NMR Study of Local Magnetism, Anelastic Deformation, and Liquid Behavior of Bulk Metallic Glasses

Magdalena Traico Sandor

A dissertation submitted to the faculty of the University of North Carolina at Chapel Hill in partial fulfillment of the requirements for the degree of Doctor of Philosophy in the Department of Physics and Astronomy.

Chapel Hill
2012

Approved by

Dr. Yue Wu

Dr. Pabitra Sen

Dr. Laurie E. McNeil

Dr. Tom Clegg

Dr. Lu-Chang Qin

ABSTRACT

MAGDALENA TRAICO SANDOR: NMR Study of Local Magnetism, Anelastic Deformation, and Liquid Behavior of Bulk Metallic Glasses
(Under the direction of Prof. Yue Wu)

In this dissertation, ^{27}Al NMR studies of CuZr- and La-based metallic glasses were carried out to investigate local magnetic properties, the mechanism of anelastic deformation, and liquid state behavior. The first part of this dissertation will cover magnetization properties of $(CuZr)_{93-x}Al_7Gd_x$ bulk metallic glasses (BMGs) from temperature dependent ^{27}Al NMR spectroscopy and magnetic susceptibility measurements. Significant nonlinear line broadening of ^{27}Al spectra commencing at high temperatures is attributed to a local magnetic susceptibility distribution. Magnetization measurements confirm linewidth enhancement caused by the strong frustrated development of antiferromagnetic magnetic short-range order.

The next section of this dissertation concerns constant-compression experiments that were carried out at room temperature to study the anelastic response of $La_{50}Ni_{15}Al_{35}$ bulk metallic glasses with varying compression time and stress. ^{27}Al NMR nutation experiments were used to measure changes of the quadrupolar interaction in order to probe local structural changes induced by anelastic recovery. It was observed that anelastic deformation results in enhanced local symmetry at Al sites and that the changes of local structure are proportional to the magnitude of stress and compression time. Modulated differential calorimetry studies were also performed to understand the correspondence between local structure changes

observed and changes in free volume. These results can be further reconciled within the theory of atomic level stresses.

The last topic addressed in this dissertation is temperature-dependent ^{27}Al nuclear magnetic resonance (NMR) experiments above the liquid temperature in La-based metallic glasses. The coexistence of two liquid states was observed from phase separation driven by differences of density or chemical potential. In addition, nonlinear liquid behavior also emerged and indicates a first-order-like phase transition. The nonlinear behavior was verified in the spectroscopy and spectral linewidths. Annealing tests show that features of phase separation can be controlled, which may be significant for processing applications of metallic glasses. These NMR results provide important thermodynamic insight for the understanding different mechanisms that drive phase separation and the underlying relevance of potential energy landscape theory.

За мојот сопруг Шон, ќерката Злата, и синот Иван. Тие се мојата причина за живеење

ACKNOWLEDGEMENTS

The works discussed in this dissertation were made possible with the support of the U. S. Army Research Office, grant no W911NF-09-1-0343, GAAN, NC Space Grant, and Amelia Earhart Fellowships.

I want to express my sincere gratitude to my advisor, Prof. Yue Wu, for giving me the opportunity to work for him. I remember making the decision to switch from astronomy to physics during the end of my 2nd year of graduate school with the intent of only finishing with a master's degree. Working with Prof. Wu gave me the confidence to proceed even further with my degree and I discovered that I was actually very interested in metallic glasses. During the past 5 years, he has taught me how to do research and appreciate the physics of glass science. I am grateful for his patience and understanding during which was not able to attend to a normal schedule like everyone else in our research group. My experience as a graduate student has allowed me to understand better the so-called "work/family balance" and all the associated instabilities and triumphs that I encountered on a daily basis. After this experience, I am not at all sure that a balance actually exists. With that being said, I know I could not have come this far without the support from my advisor and members of my research group.

I am especially grateful towards Dr. Alfred Kleinhammes for his advice, patience, and guidance during my time at UNC. He was always helpful and supportive when I had

questions regarding NMR experiments, taught me how to handle hardware, and gave me valuable advice about life in general.

I am happy to have met Horst Kessemeier and learn about his many contributions to NMR. I appreciated many of our conversations regarding NMR and family.

I'd like to express my sincere gratitude towards Jacob Forstater. I cannot express how many times has helped me with my experiments and given me advice. I appreciate many of our conversations over coffee and his ability to make light of any situation regardless of how stressed I felt. He is a good friend and I will never forget all that he has done for me.

I am also very thankful to previous and current members of Wu Group for their help. I am especially grateful to Xue-kui Xi. He is the first person I worked with on metallic glasses and has helped me during the last few years. He was also very influential in my decision to stay in physics. I would like to express my thanks to Wei Xu who had helped tremendously me with some of my data collection and probe reconstruction. Other members that I am grateful towards are: Qiang 'Charles' Chen, Harsha Kulkarni, Gregory Mogilevsky, B. J. Anderson, Shaun Gidcumb, Courtney Hadsell, Zhixiang 'Jeff' Luo, Yunzhao Xing, and Patrick Doyle.

I would also like to express my appreciation to Oscar Bernal, Laszlo Kecskes, Jian Xu, J. Q. Wang, and Haibo Ke for providing me with samples and assistance with data collection (DSC, magnetization measurements, and mechanical testing) and analysis.

I am grateful to my committee members, Profs. Yue Wu, Tom Clegg, Laurie E. McNeil, Lu-Chang Qin, and Pabitra Sen. I am also very appreciative towards Dr. Laurie McNeil's early proofreading of this dissertation.

I dedicate this dissertation to my children Zlata and Ivan and husband, Shaun Sandor.

TABLE OF CONTENTS

LIST OF TABLES

LIST OF FIGURES

LIST OF ABBREVIATIONS

NMR	Nuclear Magnetic Resonance
BMG	Bulk Metallic Glass
FM	Ferromagnetic
AF	Anti-ferromagnetic
SRO	Short-range Order
GFA	Glass-forming Ability
STZs	Shear Transformation Zones
RF	Radio Frequency
DSC	Differential Scanning Calorimetry
MDSC	Modulated Differential Scanning Calorimetry
FWHM	Full Width at Half Maximum
LLPT	Liquid-Liquid Phase Transition

CHAPTER 1

Introduction

Glass has played a significant role for the advancement of science and technology. Silicate glass has been used for centuries in window architecture and drinking containers. Today glass broadly refers to materials that exhibit no long-range order and include, but are not limited to, network forming glasses, polymer glasses, and metallic glasses. Glasses have a wide variety of useful applications. For example, silicate and polymer glasses are predominately used for glassware production in home and laboratory use. Network forming glasses are useful for optical waveguide applications and radioactive waste immobilization. Metallic glasses differ from these kinds of glasses due to their metallic bonding, but have recently shown to have tremendous potential for engineering and structural application due to their unique structures and mechanical properties that exceed those of conventional steels and titanium alloys. However, despite the current and potential widespread use of glass in everyday applications, a basic understanding of glass and the nature of the glass transition remains far from complete, which stems from many unresolved long-standing issues. For example, the amorphous structure of metallic glasses permits very interesting inhomogenous magnetic behavior even in very dilute magnetic systems. The mechanism of deformation is another important and fundamental issue that significantly restricts the widespread application of metallic glass due to its intrinsic brittleness. Lastly, an understanding of the dynamic features of the liquid state might hold important clues for understanding quenched-in properties and glass-forming-ability (GFA) of metallic glasses. The amorphous structures

of glass make structural characterizations of these different aspects very challenging using conventional techniques. This dissertation will describe ^{27}Al nuclear magnetic resonance studies to investigate different aspects of bulk metallic glass: local magnetism, anelastic deformation, and liquid behavior.

1.1 Glass Transition and Supercooled Liquids

Glass is made by rapid quenching from the liquid state to form an amorphous solid and is thereby considered a "frozen liquid". Macroscopic flow is not observed in the glassy state due to relaxation times that far exceed the experimental-timescale [1]. From an energetics perspective, glasses are in a metastable state with larger potential energy than the corresponding crystalline state [2, 3]. At ambient temperatures the local energy barrier predominates and renders thermally activated events, such as structural relaxation or crystallization, negligible. When glass is formed by rapidly quenching a melt from the liquid state below the glass transition T_g crystallization is simultaneously bypassed as illustrated in Figure 1.1 [4]. Liquids that are formed below the liquid temperature T_{liq} are called supercooled liquids. When supercooled liquids are cooled below T_{liq} molecular motions slow down significantly such that they cannot sufficiently sample their configurations due to the fast cooling rate. Hence, there is a competition between the relaxation time of the molecular motions in the glass and the cooling rate. Glass is formed from the supercooled liquid when the viscosity reaches 10^{13} poise and this occurs during a narrow transformation range where molecular relaxation times are on the order of 100 seconds [3, 5]. Fig. 1.1 shows that this corresponds to a continuous yet abrupt change in the specific volume to a value comparable to that of the crystal at approximately $2T_{Liq}/3$ [4].

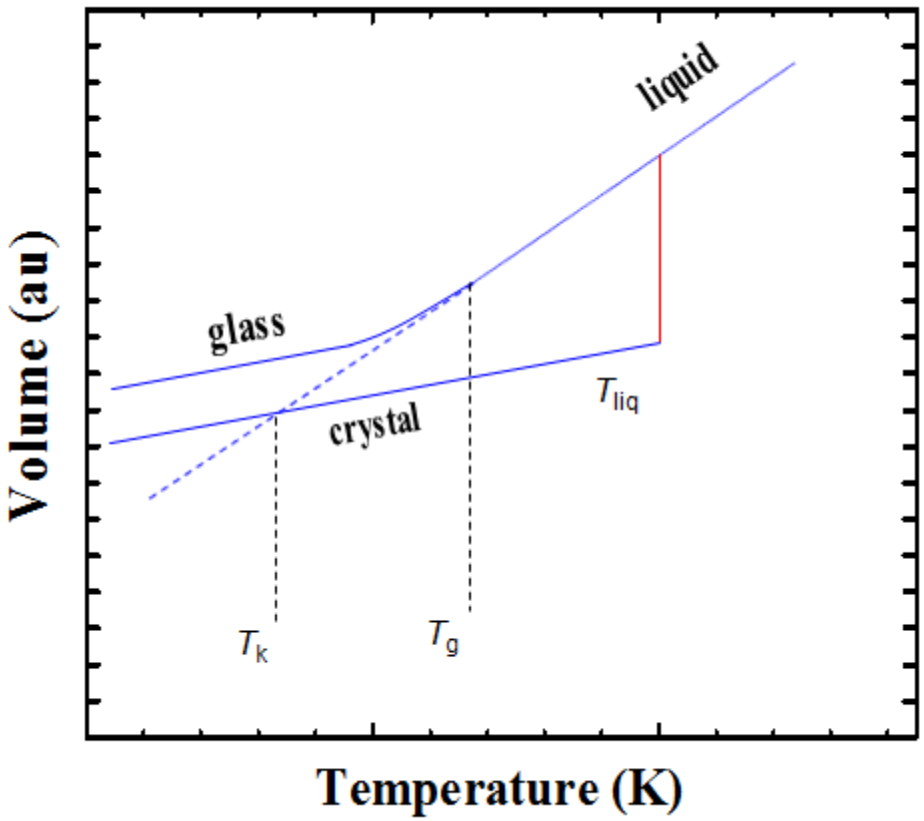

Figure 1.1 Change of volume versus temperature upon cooling below the liquidus temperature T_{liq} without crystallization. Deviation from the thermal equilibrium liquid state occurs below T_g due to slow dynamics and glass formation. The change of volume in the crystalline state is also shown for comparison.

1.2 Metallic Glasses and Bulk Metallic Glasses

Glass has played a significant role for the advancement of science and technology. Unfortunately, a basic understanding of glass remains far from complete and there are many unresolved long-standing issues. For example, the nature of the glass transition still remains one of the biggest unsolved mysteries in solid state physics [6]. The complexity of the liquid and supercooled liquid structure and dynamics as well as the complexity of the structure of the glassy state makes studying glasses an especially daunting task. Glass formation in metallic alloys was first reported in 1960 by Duwez where a metallic film (thickness~ 10

μm) of $Au_{75}Si_{25}$ was produced under rapid cooling conditions [7]. Metallic glass is one of the important types of glasses because of its unique mechanical properties that surpass conventional engineering materials [5, 8]. For example, some metallic glasses can have yield strength higher than that of steel and elasticity comparable to that of polymers [5]. Unfortunately, it is one of the least accessible glassy systems because of the weak glass forming ability (GFA) of metallic alloys. Forming a metallic glass from the liquid state, while simultaneously avoiding crystallization, requires extremely high cooling rates. For example, Fe-, Co-, and Ni-based metallic glasses require cooling rates that exceed 10^5 deg/s and typically produce glasses with dimensions of less than 50 μm [8]. The maximum casting diameter of metallic glasses is the critical diameter D_C, which is severely limited by the required large cooling rates. However, this situation has changed drastically with the discovery of bulk metallic glasses (BMGs) [9, 10]. BMGs are defined as metallic glasses that can be fabricated on the millimeter scale or larger and were first produced by Chen in 1974 [10]. Since then Zr-, Mg-, Pd-Fe, Pd-Cu, and La-based multicomponent bulk metallic glasses were discovered [8, 11]. Pd-Cu-based BMGs represent a remarkable class of metallic glasses that require a critical cooling rate as low as 0.1 deg/s with a critical diameter reaching as high as 100 mm [8]. The drastic improvement of glass forming ability (GFA) as indicated by the marked improvement of the critical diameter D_C and decreased critical cooling rates has made studying metallic glasses in the supercooled regime using different characterization techniques more feasible [12, 13].

1.3 Motivations for Studying Metallic Glasses

A widespread enthusiasm for research on bulk metallic glasses comes from the potential for structural and functional applications. Although metallic glasses are new-comers to the

world of glasses they represent a unique class of materials. Compared to their crystalline counterparts metallic glasses have superior fracture strength, soft magnetic properties, and good corrosion resistance [5, 8]. Unlike crystalline materials, the intrinsically disordered nature of metallic glasses makes experimental characterization a difficult task and causes their underlying properties and various associated mechanisms to remains active areas of study.

For instance, metallic glasses take on lots of interesting magnetic phases ranging from spin-glass behavior to re-entrant ferromagnetism [14, 15]. This has inspired much interest in mapping magnetic phase diagrams with increasing magnetic impurity concentration in metallic glasses [14-16]. Often this magnetic behavior is characterized using bulk magnetization experiments. This dissertation discusses how NMR can also be used to complement susceptibility measurements by characterizing the local magnetism at the atomic level.

Although metallic glasses have great potential as engineering materials, they suffer from shear localization and catastrophic brittle failure at ambient temperature with little or no plastic strain [5]. One of the great challenges in the study of BMGs is a basic understanding of the deformation mechanism in amorphous systems where dislocations are absent. Free volume is a reliable and often-used order parameter to quantify the structural changes induced during deformation [17-19]. Studies of the deformation of metallic glasses are often carried out at temperatures near T_g [5, 20, 21]. This causes competition between thermal relaxation and deformation, and often obscures the inherent deformation mechanism. The NMR results obtained at room temperature discussed in this dissertation show that free

volume alone perhaps is not sufficient to describe the inherent deformation mechanism in metallic glasses.

The study of structural changes and phase transitions in liquids due to the first-order liquid-liquid phase transition (LLPT) has recently become a prominent area of experimental and computational research [22]. Little attention was paid to the LLPT since it is generally believed that the structural changes in a liquid should be gradual due to dynamical averaging of structure. The LLPT is believed to be driven by differences of entropy or density between the liquid species [22], spinodal decomposition or phase separation due to large differences in heats of mixing between constituent atoms [23], or microheterogeneities that are derived from ingots and preserved upon melting [24, 25] .

1.4 NMR as a probe of local magnetism, anelastic deformation, and liquid structure

This dissertation describes the work carried out using NMR spectroscopy of BMGs in both the glassy and liquid states in an attempt to address some of the fundamental issues of glasses discussed above. NMR is a powerful and non-invasive technique is used to study properties of nuclei and their local environments. Specifically, ^{27}Al NMR spectroscopy is used to probe the properties of metallic glasses at Al sites. NMR spectroscopy can provide information regarding local atomic and electronic structure in the solid state and dynamics in the liquid state.

1.5 Dissertation outline

This dissertation consists of ^{27}Al NMR spectroscopy results in Zr-Cu- and La-based BMGs and addresses some of the fundamental issues of glasses discussed in Section 1.3. Chapter 2 reviews the relevant basic NMR theory while Chapters 3-5 discuss the different

research topics studying using NMR spectroscopy. Chapter 6 summarizes brief conclusions and potential for future research regarding liquid behavior of La-based metallic glasses.

Chapter 3 describes temperature-dependent ^{27}Al NMR spectroscopy and magnetization measurements that were utilized to explore the local magnetism in $(CuZr)_{46.5-x}Al_7Gd_x$ (x = 1, 2) BMGs at low temperatures. From spectroscopy experiments, it was observed that strong spectral linewidth enhancement emerges at high temperatures arising from a distribution of the local susceptibility that spans a narrow temperature range. Magnetization experiments confirm that while the local susceptibility is inhomogenous and gives rise to strong AF short-range frustration these amorphous systems on average remains paramagnetic.

Chapter 4 discusses transient structural changes that take place during anelastic deformation. This work also provided a better understanding of the relevant order parameter (tensor versus scalar) necessary to characterize the preliminary stages of deformation. ^{27}Al NMR and modulated differential scanning calorimetry studies of $La_{50}Ni_{15}Al_{35}$ were utilized to provide a snapshot of anelastic-induced structural changes that were compared with as-cast and annealed reference states. The data reveal that anelastic strain causes an increase in symmetry of the local electric field gradient (second-rank tensor) that is proportional to compression time whereas the corresponding changes of free volume (scalar) were negligible due to the small viscoplastic strain.

In Chapter 5, temperature-dependent ^{27}Al NMR experiments were carried out above the liquidus temperature in La-based metallic glasses. The temperature dependence of the Knight shift data indicates that nonlinear liquid behavior emerges at ~100 degrees above the liquidus temperature. Data collection during heating and cooling cycles reveals the existence

of hysteresis and thus verifies that the non-linear behavior is a first-order-like phase transition. The nonlinear behavior was also confirmed by analyzing the spectral linewidths. These results are discussed in the context of phase separation driven by chemical potential differences for metallic melts [26] and also within the framework of potential energy landscape theory [2, 27].

CHAPTER 2

Nuclear magnetic resonance

2.1 Introduction: Properties of Nuclei and Relaxation

From a classical perspective, nuclear magnetic resonance (NMR) involves radio frequency (RF) pulses corresponding to the Larmor procession frequency of the nuclear magnetic moments of interest and their precession about a strong constant external field (3-4 Tesla) due to energy absorption. In terms of quantum mechanisms, energy absorption is caused by different spin populations between quantized energy levels of the nuclear magnetic moments. The interaction due to the strong external field and the nuclear magnetic moments is given by the Zeeman interaction. There are other important interactions that are unique depending on the material of study, which can be treated as a perturbation of the Zeeman interaction. Basic theory regarding NMR will be reviewed below [28-30].

The magnetic resonance phenomenon is found in systems that have both a magnetic moment and angular momentum. The angular momentum is given by $\hbar \vec{I}$ and its magnitude is given by $|\vec{I}| = \left[I(I+1)\right]^{1/2}$ where I can be integer or half integer ($I = 0,\ 1/2,\ 1,\ 3/2,$ *etc.*). The work discussed throughout will deal with NMR of ^{27}Al with $I = 5/2$. The magnetic dipole moment $\vec{\mu}$ of a nuclear spin is related to the spin angular momentum, $\vec{I}$ by $\vec{\mu} = \gamma \hbar \vec{I}$ where γ is the nuclear gyromagnetic ratio. The nucleus experiences a torque when

placed in an external field $\vec{H}$ that causes a time-dependent change in the angular momentum of the nucleus given by $d\vec{\mu}/dt = \gamma \vec{\mu} \times \vec{H}$. For a constant external field $\vec{H}_o$ the solution of this equation is that the magnetic moment precesses at a constant angle θ and at an angular frequency (Larmor frequency) given by $\omega_o = \gamma H_o$.

The magnetization of the nuclear spin population difference is given by the Boltzmann distribution

$$M = N\gamma\hbar \frac{\sum_{m=-I}^{I} m \exp\left(\gamma\hbar m H_0 / kT\right)}{\sum_{m=-I}^{I} \exp\left(\gamma\hbar m H_0 / kT\right)}. \qquad (2.1)$$

where N is the total number of nuclear spins and $\hbar$ is Planck's constant. At room temperature an approximation can be made in which $\gamma\hbar H_0 / kT << 1$. The net magnetization reduces to

$$M = \frac{N\gamma^2\hbar^2 I(I+1)}{3kT} H_0 = \chi_o H_o \qquad (2.2)$$

where χ_o is the nuclear susceptibility and H_o is the strong constant external field that points along the z-axis. The Zeeman interaction is the interaction between the nuclear magnetic moment and the external field and gives rise to the Zeeman energy levels $E = -\gamma\hbar H_o m$ where $m = I, I-1, ..., -I$ which are equally spaced energy levels with an energy difference $\Delta E_o = \gamma\hbar H_o$. Transitions between adjacent states occur when the nuclear spins absorb an energy $\hbar\omega_o = \Delta E_o$.

NMR experiments are carried out by placing a sample in the inductor coil of an LC circuit of an NMR probe, which is inserted into a superconducting magnet. Initially the nuclear spins are at thermal equilibrium with the strong external field. The transmitter is turned on and produces a linearly-polarized RF field is given by

$$\vec{H}_1(t) = 2H_1 \cos \omega t \hat{x}. \tag{2.3}$$

This can be decomposed into two rotating components given by

$$\vec{H}_1(t) = H_1(\cos \omega t \hat{x} - \sin \omega t \hat{y}) + H_1(\cos \omega t \hat{x} + \sin \omega t \hat{y}). \tag{2.4}$$

The first term on the left rotates clockwise and is in the rotating frame of the precessing magnetic moment. The second term rotates counter-clockwise and has a negligible effect on the resonance of the nucleus since it has a rotation frequency of $2\omega_o$. The total magnetic field in the NMR experiment is

$$\vec{H}_1(t) = H_1(\cos \omega t \hat{x} - \sin \omega t \hat{y}) + \vec{H}_o \hat{z}. \tag{2.5}$$

The first term on the right-hand side of (2.5) corresponds to the RF field applied in a plane perpendicular to $\vec{H}_o$ at the resonance frequency ω_L that exerts a torque $\vec{\mu} \times \vec{H}_1$ due to energy absorption by the nuclear spins. This will effectively increase the precession angle of the magnetic moment and, therefore, change the orientation of the magnetic moment of the nucleusand its corresponding magnetic energy. The angle of the nuclear magnetic moment with respect to the z-axis is given by $\theta = \gamma t H_1$, where *t* is the pulse duration on the order of microseconds.

As mentioned previously, NMR experiments begin with the population of nuclear spins in thermal equilibrium as denoted by $\vec{M}_0$. An application of an RF field induces a time evolution of non-interacting nuclear moments of a net magnetization $\vec{M}$ given by the set of Bloch equations:

$$\begin{aligned}
\frac{dM_x}{dt} &= \gamma\left(\vec{M}\times\vec{H}\right)_x - \frac{M_x}{T_2} \\
\frac{dM_y}{dt} &= \gamma\left(\vec{M}\times\vec{H}\right)_y - \frac{M_y}{T_2} \\
\frac{dM_z}{dt} &= \frac{M_0 - M_z}{T_1} + \gamma\left(\vec{M}\times\vec{H}\right)_z .
\end{aligned} \tag{2.6}$$

An RF pulse at the resonant frequency of the nucleus of interest results in a perturbation of the nuclear magnetic moment by an RF pulse at the resonant frequency. This causes $\vec{M}$ to move away from its thermal equilibrium value $\vec{M}_o$. When the transmitter is turned off, the net magnetization tries to recover towards $\vec{M}_o$ and precesses about the strong external field. The small signal induced in the coil (order of $\sim \mu V$) of the probe during precession is further amplified during data collection. In the longitudinal direction, any change of M_z is due to the energy transfer from the nuclear spin to its surroundings or a thermal reservoir. This time constant T_1 is called the spin-lattice relaxation time. Relaxation in the transverse or xy planeis given by the spin-spin relaxation time constant T_2. This characterizes the time needed for spins to lose their coherence due to spins seeing different magnetic fields at different sites and randomize the phase of precession. Energy is not transferred during the spin-spin relaxation process.

2.2 Interactions in Metal

Conduction electrons are what set metals apart from non-conducting materials. These electrons are responsible for Pauli paramagnetism and the Knight shift. In metals, the magnetic field at the nucleus of interest might be different from the applied field. For a given nucleus in a simple metal (metallic bonding dominated by *s*-orbitals), the resonance frequency ν_m is slightly higher than the resonance frequency ν_s of the same isotope in a non-conducting substance, which gives the reference frequency. This is known as the Knight shift [31] given by

$$K = \frac{\nu_m - \nu_s}{\nu_s}. \tag{2.7}$$

The origin of such a shift is derived from *s*-conduction electrons. For simple metals, the spin polarization of the conduction electrons gives rise to an internal field that is parallel and proportional to the strong applied external field, $\vec{H}_o$. In this dissertation, the Knight shift is expressed in units of ppm (parts per million) and calculated by using the reference frequency due to an aqueous 1M solution of $Al(NO_3)_3$.

The Knight shift can be expressed as the sum of three dominant contributions,

$$K = K_s + K_d + K_{orb}. \tag{2.8}$$

It is important to note that there are other contributions to the total Knight shift that will be discussed when relevant in later chapters. The first term, K_s, is the direct Fermi-contact shift due to *s*-conduction electrons and contributes the most to the Knight shift. The Pauli principle assures that each conduction-electron orbital state is occupied by two electrons having opposite spins. All the orbital states are filled to the Fermi level E_F and in a manner

that minimizes the energy. The presence of an applied external field results in a net magnetic moment of the conduction electrons and results in a Pauli paramagnetic susceptibility that is temperature independent since $kT << E_F$. Electrons in the *s*-band have a non-zero probability density, $\left\langle |\psi(0)|^2 \right\rangle_{E_F}$, at the nucleus averaged over all states at the Fermi energy E_F . This results in a Fermi-contact shift given by

$$K_s = (8\pi/3)\left\langle |\psi(0)|^2 \right\rangle_{E_F} \Omega \chi_{\text{Pauli}} \tag{2.9}$$

where Ω is the atomic volume and χ_{Pauli} is the Pauli spin susceptibility due to conduction electrons. In general, K_s is proportional to the nuclear charge given that $\left\langle |\psi(0)|^2 \right\rangle_{E_F}$ is larger for heavier metals [32] and provides qualitative information regarding the amount of *s*-character of the conduction electrons . For example, pure aluminum with *sp*-electrons has a K_s of ~1660 ppm [32]. This can be compared to ZrCuAl metallic glass alloys that have K_s of ~300 ppm [33], which demonstrates their significantly smaller s-character.

In (2.8) the second term in the Knight shift, K_d , is caused by transition metals due to a polarization of the *d*-electrons by the external field $\vec{H}_o$ and provides an indirect *s*-*d* exchange interaction with the s-conduction electrons described by

$$K_d = \alpha_d \chi^d_{Pauli} \tag{2.10}$$

where α_d is the hyperfine coupling constant and χ^d_{Pauli} is the *d*-electron Pauli susceptibility.

The third term, K_{orb} , is the orbital shift contribution

$$K_{orb} = \alpha_{orb} \chi_{orb} \tag{2.11}$$

derived from the orbital moment induced in occupied conduction electron states, where χ_{orb} is the orbital susceptibility and α_{orb} is the coupling constant. This second-order perturbation effect gives rise to magnetic shielding of the nucleus and is most important in transition metals with half-filled *d*-bands such as Nb, W, and Cr alloy systems [32].

2.3 Spin-Lattice Relaxation Time

The direct Fermi-contact interaction term given in (2.9) not only dominates the Knight shift and the magnetic susceptibility, but also provides a mechanism for the nucleus to undergo spin-lattice relaxation. For free electrons the rate of relaxation is given by the Korringa relation [34]

$$K^2 T_1 T = \left(\frac{\gamma_e}{\gamma_n}\right)^2 \left(\frac{\hbar}{4\pi k_B}\right) f \qquad (2.12)$$

where K is the Knight shift, T_1 is the spin-lattice relaxation time, T is the temperature, γ_e and γ_n are the electronic and nuclear gyromagnetic ratios and k_B is the Boltzmann constant. The equation above also includes the enhancement factor f, which is ~1 for free electrons. For example, the enhancement factor is 1.2 for ^{27}Al [32] . In alloys containing metals that have *d* or *f*-electrons, electron-electron interactions become more important. In Chapter 5, another mechanism arising from the motion of atoms that gives rise to spin lattice relation will be discussed.

2.4 Quadrupole Interactions

In addition to a nuclear magnetic moment μ, nuclei that have spin $I > 1/2$ also have a

nuclear electric quadrupole moment eQ. Most nuclei on the periodic table have a nuclear spin $I > 1/2$. This gives rise to a coupling between the quadrupole moment and the electric field gradient (EFG) generated by the local structure. In addition, this causes unequal splitting of the magnetic energy $2I+1$ levels. For example, ^{27}Al has a spin $I = 5/2$ and a quadrupole moment of $14.66 \times 10^{-30} m^2$ so quadrupole interactions are important for the metallic glass alloy systems considered in this thesis. This section reviews some basic theory regarding quadrupole interactions and how they are reflected in the NMR lineshape in addition to methods that quantify the interaction, which will be very useful in Chapter 4 [30, 32, 35].

As mentioned in Section 2.1 the interaction of a spin system with a strong external field $\vec{H}_o$ gives rise to a Zeeman interaction. The quadrupole interaction can therefore be treated as a perturbation of the Zeeman interaction. The EFG tensor $\vec{V}$ in the principal-axis system is given by:

$$\vec{V} = \begin{pmatrix} V_{xx} & 0 & 0 \\ 0 & V_{yy} & 0 \\ 0 & 0 & V_{zz} \end{pmatrix}, \tag{2.13}$$

which satisfies Laplace's equation $V_{xx} + V_{yy} + V_{zz} = 0$. The largest component of the EFG is given by $V_{zz} = eq$. For lower than cubic symmetries a dimensionless asymmetry parameter can be defined $\eta = \dfrac{|V_{xx} - V_{yy}|}{V_{zz}}$, where $0 \le \eta \le 1$.

Unlike Zeeman interactions, quadrupole interactions give rise to unequal splitting of the magnetic energy levels. For example, an NMR spectrum of a nucleus with spin $I = 5/2$

consists of five $|m\rangle \leftrightarrow |m+1\rangle$ transitions including the narrow $|-1/2\rangle \leftrightarrow |1/2\rangle$ central transition and wide satellite transitions $|m\rangle \leftrightarrow |m+1\rangle$ ($m \neq -1/2$). This is illustrated in Figure 2.1. The satellite transitions are broadened by the first-order quadrupole interaction given by the Hamiltonian

$$H_Q = \frac{1}{12}\omega_Q \left[3I_z^2 - I(I+1)\right]\left(3\cos^2\beta - 1 + \eta\sin^2\beta\cos 2\alpha\right) \qquad (2.14)$$

where $\omega_Q = \dfrac{3e^2qQ}{2I(2I-1)\hbar}$ is defined as the quadrupole frequency, and α and β are Euler angles orienting the external field $\vec{H}_o$ to the EFG. Fig. 2.1 shows that the spectral features are smeared out since all orientations of the EFG relative to the external field are possible in an amorphous system. Second-order quadrupole effects result in broadening of the central transition and will not be considered here.

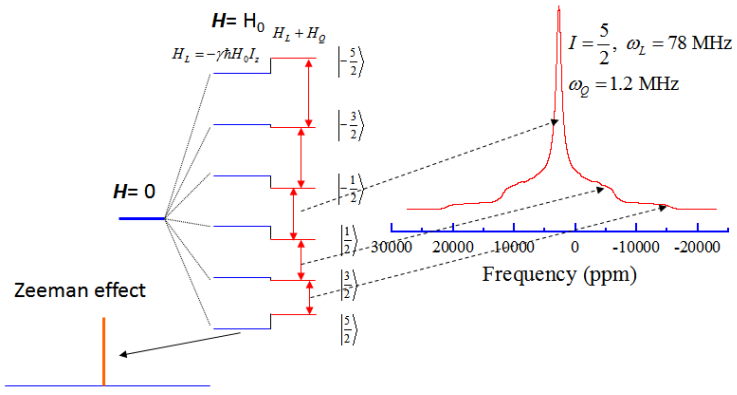

Figure 2.1: The diagram above demonstrates the difference between the spectral line splitting due to Zeeman interactions, with a corresponding Larmor frequency of 78 MHz, versus quadrupole effects for a nucleus with spin $I = 5/2$. Zeeman interactions result in equally-spaced energy levels (left blue) resulting in a single well-defined peak in the spectrum. This can be compared to first-order quadrupole interactions that cause unequal line splitting of the satellite transitions. The spectrum on the right is simulated using SIMPSON software with a quadrupole frequency ω_Q = 1.2 MHz.

Quadrupole interactions cause fast transverse relaxation or spin-spin relaxation of the nuclear spins due to the large local EFG and give rise to broad spectra. A Hahn-echo [36] pulse sequence is often used in solid state NMR to recover any lost signal intensity due to relaxation and the dead time of the receiver. The Hahn-echo pulse sequence is illustrated in Figure 2.2 and is given by

$$(t_1)_x - \tau_2 - (t_3)_x - \tau_4 - \text{acquisition}_{-y} \qquad (2.15)$$

where t_1 and t_3 are pulse widths (on the order of μs), x and $-y$ are pulse and receiver phases, respectively, τ_1 and τ_4 are time delays, and acquisition refers to data collection of the echo signal. t_1 flips the nuclear spins in the xy plane and t_3 refocuses the spin magnetization to be detected after coherence is lost during τ_1. The echo signal appearing at $\tau_2 = \tau_4$ is recorded and the signal intensity corresponds to the central and satellite transitions.

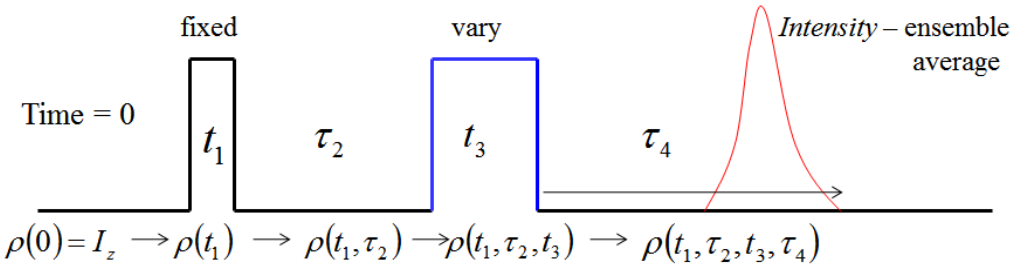

Figure 2.2 The two-pulse Hahn-echo pulse sequence development in the time domain. Nutation maps the evolution of the central and satellite transition intensities that are strongly dependent on the quadrupole interaction.

The quadrupole interactions cause significant broadening of the satellite transitions. Often an entire spectrum cannot be resolved in a single experiment unless field-sweeping capabilities are available. For a static field, piecing together a single spectrum point-by-point by retuning the NMR probe to different frequencies is possible, although time consuming, and requires that the tuning be precisely the same at each point so that the relative intensities

are accurately represented. NMR nutation [35] is an alternate method that can be used to quantify quadrupole interactions. Nutation methods have demonstrated much success in describing local structural changes at aluminum sites due to quadrupole interactions in ZrCuAl- and CeAlCu-based metallic glasses [37, 38] due to micro-alloying (minute changes of composition). Nutation is carried out by using the Hahn-echo sequence described in (2.15) and is more time efficient than extracting ω_Q from a broad piecewise-constructed spectrum as shown in Fig. 2.1. Density operator formalism can be used to describe the interactions that take place during a Hahn-echo sequence. Fig. 2.2 shows the time-domain development of the density operator during the Hahn-echo sequence and the corresponding significant interactions. If second-order quadrupole interactions are neglected, the density matrix $\rho(t_1,\tau_2,t_3,\tau_4)$ can be described in the rotating frame of the central transition:

$$\begin{aligned}\rho(t_1,\tau_2,t_3,\tau_4) = \exp\left\{-iH_Q\ \tau_4\right\}\exp\left\{-iH^{(-x)}\mathrm{t}_3\right\}\exp\left\{-iH_Q\ \tau_2\right\}\exp\left\{-iH^{(-x)}t_1\right\}\rho(0)\\ \times\exp\left\{iH^{(-x)}\mathrm{t}_1\right\}\exp\left\{iH_Q\ \tau_2\right\}\exp\left\{iH^{(-x)}\ \mathrm{t}_3\right\}\exp\left\{iH_Q\ \tau_4\right\}\end{aligned} \tag{2.16}$$

where $\rho(0) = I_z$, $H^{(-x)} = H_{rf} + H_Q$, $H_{rf} = \omega_{rf} I_x$, and H_Q (and its associated parameters) is defined in equation (2.14). For a spin 5/2 system, analytical expressions for the central transition intensity or ensemble average can be found by rewriting (2.15) in terms of $(2I+1)\times(2I+1)$ or 6×6 matrices by taking the trace [39] $\langle I\rangle = Tr\left[(I_x + iI_y)\rho(t_1,\tau_2,t_3,\tau_4)\right]$. As indicated in Fig. 2.2, experimental data for nutation are obtained by fixing t_1, varying t_2, and plotting echo height during the acquisition period in (2.15), which can then be fit using NMR simulation programs such as SIMPSON [40].

CHAPTER 3

Local magnetism in $(CuZr)_{93-x}Al_7Gd_x$ Bulk Metallic Glasses

3.1 Introduction

Studies of magnetism in metallic glasses have provided overwhelming evidence in support of the existence of magnetic inhomogeneities in these materials [14, 41-45]. Structural disorder is extremely influential in metallic glasses giving rise to frustrated magnetic behaviors such as spin-glass, reentrant spin-glass magnetism, and complex cluster-glass states [14, 41-45]. Structural inhomogeneities also play a role in transition-metal-oxides such as manganites, [46, 47] in the regime of colossal magnetoresistance (CMR), high temperature superconductivity (HTS) observed in cuprates [46, 47], and in *f*-electron systems that have non-Fermi-liquid (NFL) behavior [48]. For example in NFL systems, X-ray analysis shows that they are seemingly ordered compounds, but exhibit local disorder due to random site interchange and interstitial-vacancy pairs [49]. In general, these studies seem to suggest that magnetic frustration, especially magnetic cluster formation, is an important feature of disordered systems. For example, even in the dilute impurity limit for simple magnetic systems, amorphous metallic glass systems such as CuZrGd [44, 45], and LaGdAu [14, 50] containing S-state ions ($L = 0$) such as Gd demonstrate extensive cluster development through long-range indirect coupling through Ruderman-Kittel-Kasuya-Yosida (RKKY) [51] interactions between localized 4*f* electron spins.

In this Chapter, NMR is used to characterize the local anomalous magnetic behaviors in $(CuZr)_{93-x}Al_7Gd_x$ (x = 1, 2) bulk metallic glasses (BMGs) in the temperature range of 77-300 K. dependence on temperature of the nonlinear linewidth broadening was found and is attributed to strong spatial inhomogeneities in both the hyperfine coupling and bulk magnetic susceptibility due to local Gd^{3+} ions. This is also confirmed using magnetization measurements.

3.2 Magnetism in rare-earth metals

The rare earth elements comprise fifteen elements in which the 4*f* electronic shell filling increases from 0 (Lanthanum, also considered an early transition metal) to 14 (Lutenium) electrons [52]. Magnetism in rare-earth metals due to 4*f*-electrons is localized. The two internal electronic shells are 6*s* that generally contains two electrons and 5*d* with one electron. The electron configuration of a rare earth element is $[Xe]4f^n5d^16s^2$. The magnetic moments are built up according Hund's rules. The *L* and *S* orbits are strongly coupled. While the 5*d* and 6*s* shells have itinerant character and form the conduction band, the 4*f* orbits are localized and deeply embedded within an atom. Lanthanide contraction of rare earth elements describes how the atomic radius decreases with the increase of atomic number and results in poor atomic shielding of 4*f* electrons [52, 53]. The net magnetic moment arises from exchange forces that are also responsible for the creation of magnetic ordering. Since the 4*f*-electrons are localized far below the Fermi energy, the 5*d* and 6*s* conduction electrons mediate the indirect exchange interaction, known as the RKKY interaction [54], between adjacent *f*-electrons that give rise to magnetic ordering. The relevance of this is further elaborated upon in sections below.

3.3 Experiments

BMG compositions $(CuZr)_{93-x}Al_7Gd_x$ (x = 1, 2) with good glass forming ability (GFA) were fabricated into cylindrical rods using conventional copper mold casting [55]. The amorphous nature of these BMGs was confirmed by X-ray diffraction and differential scanning calorimetry (DSC). The RF penetration into BMG samples is finite and limited to the skin depth, $\delta = \sqrt{\frac{2\rho}{2\pi f \mu}}$ [52] which causes a reduction in both the effective sample volume and the signal intensity. Here ρ is the resistivity, f is the NMR resonance frequency and μ is the magnetic permeability of the BMG under study. To maximize the filling factor or fraction of the coil detection volume filled with sample and overcome skin depth issues samples were prepared by crushing cylindrical rods into a powder which was packed into quartz tubes with Teflon tape.

^{27}Al NMR experiments were performed in a magnetic field of 7.01 T in the temperature range of 77-300 K using an Oxford Helium Bath Variox cryostat [56] and an Oxford ITC4 temperature controller. Figure 3.1 shows a schematic of the cryostat. Before NMR experiments were carried out, it was necessary to prepare the cryostat. This was done by first using a backing pump to evacuate the outer vacuum chamber (OVC) to ~20 mTorr pressure while keeping the needle valve closed, after which sample chamber space was pumped out to low pressure using a turbo pump. The helium and nitrogen reservoirs were then both filled with liquid nitrogen. The needle valve was slowly opened to allow nitrogen to fill the sample space. Temperature stability was obtained using both the flow from the needle valve and the ITC4 temperature controller. The temperature fluctuations on the order of +/- 5 degrees were observed and considered in the error analysis of the data.

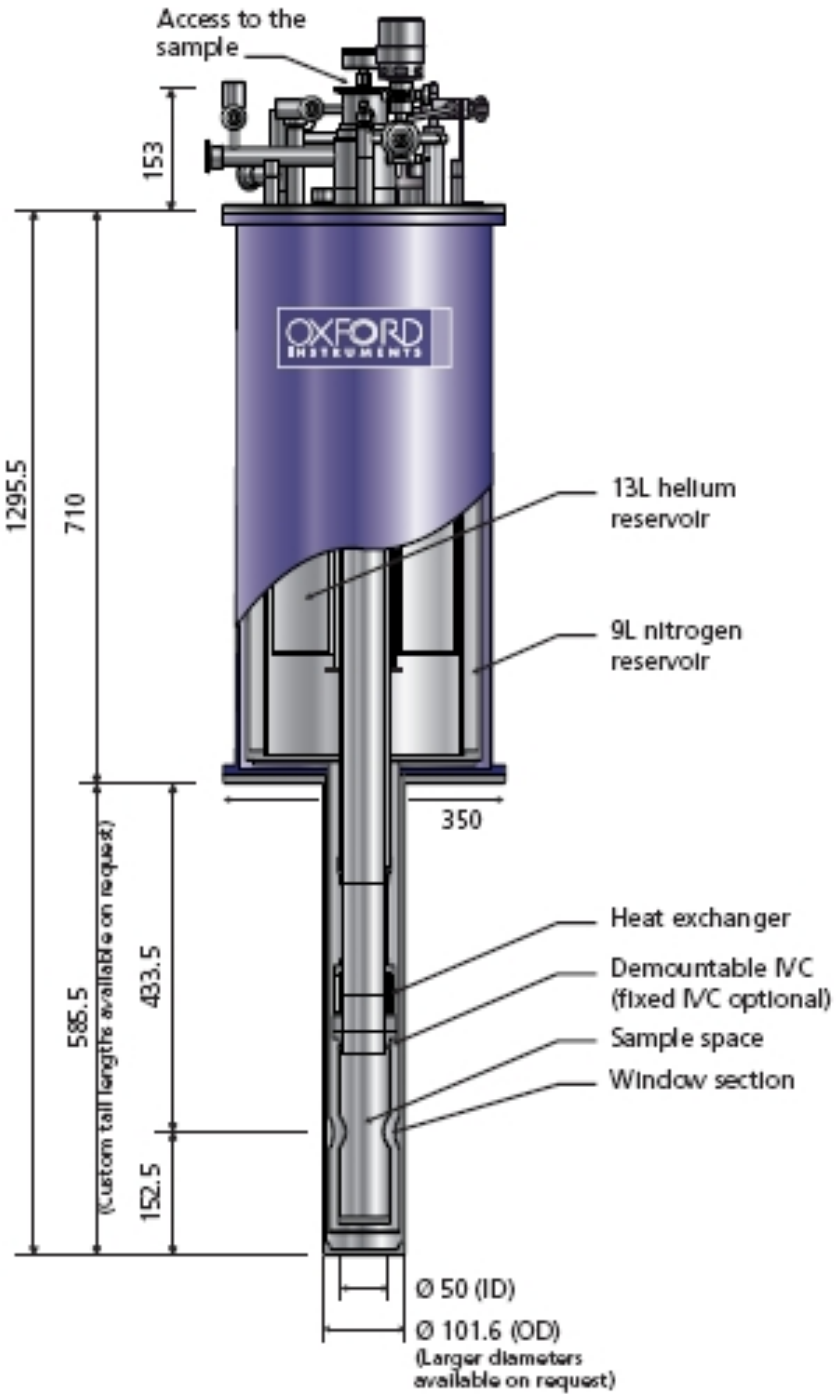

Figure 3.1 Schematic of Oxford Helium Variox Cryostat that operates between 1.3 and 300K [56].

3.4 Results and Discussion

3.4.1 NMR spectra for x = 1 and x = 2

NMR spectra were obtained using a Hahn-echo pulse sequence $90° - \tau - 180° - \tau -$ detection. Detection of the significantly-broadened line of ^{27}Al caused by Gd magnetic moments was done by implementing frequency-stepped Fourier-transform methods in the time domain [57] . NMR spectral data for each temperature were acquired by using five 0.1 MHz frequency steps in which echoes were shifted in the time domain to a common carrier frequency of 78.992 MHz. All the spectra for each frequency step were then obtained through Fourier transform processing and added together to obtain a single spectrum. ^{27}Al Knight shifts were referenced to 1.0 M $Al(NO_3)_3$ aqueous solution.

Figure 3.1 shows an example ^{27}Al NMR spectrum for x = 2. ^{27}Al is a spin $I = 5/2$ nucleus and, as mentioned in Chapter 2, its spectrum consists of five $|m\rangle \leftrightarrow |m+1\rangle$ transitions including the narrow $|-1/2\rangle \leftrightarrow |1/2\rangle$ central transition, broadened only by the second-order quadrupole effect, and wide satellite transitions $|m\rangle \leftrightarrow |m+1\rangle$ ($m \neq -1/2$) broadened by the first-order quadrupole interactions. Fig. 3.1 shows that the narrow central transition broadens significantly from 1040 ppm at 300 K to 3600 ppm at 77 K. A two-curve Gaussian fit was used to determine the corresponding linewidths of the central and satellite transitions as noted by the dashed curves in Fig 3.1. In addition, the Knight shift of the central transition also changes with temperature. Due to the electronic structure of this metallic glass system, there are two main contributions to the Knight shift $K_{iso} = K_s + K_{s-f}$ [32]. K_s is due to the Fermi contact hyperfine interaction associated with the s electrons at

the Fermi level and K_{s-f} is due to the transferred hyperfine interaction mediated by *s-f* exchange interactions between the localized *f*-electron spins and the spins of the *s* electrons. K_{s-f} is given by $A_{hf}\chi_M^f(T)$ where $A_{hf} = zH_{hf}/(N_A\mu_B)$ is the hyperfine coupling constant and is generally assumed to be temperature independent [52]. Here, H_{hf} is the hyperfine field due to local moments, N_A is Avogadro's number, μ_β is the Bohr magneton, z is the number of Gd ions that are nearest neighbors to Al, and $\chi_M^f(T)$ is the bulk magnetic susceptibility due to localized Gd f moments.

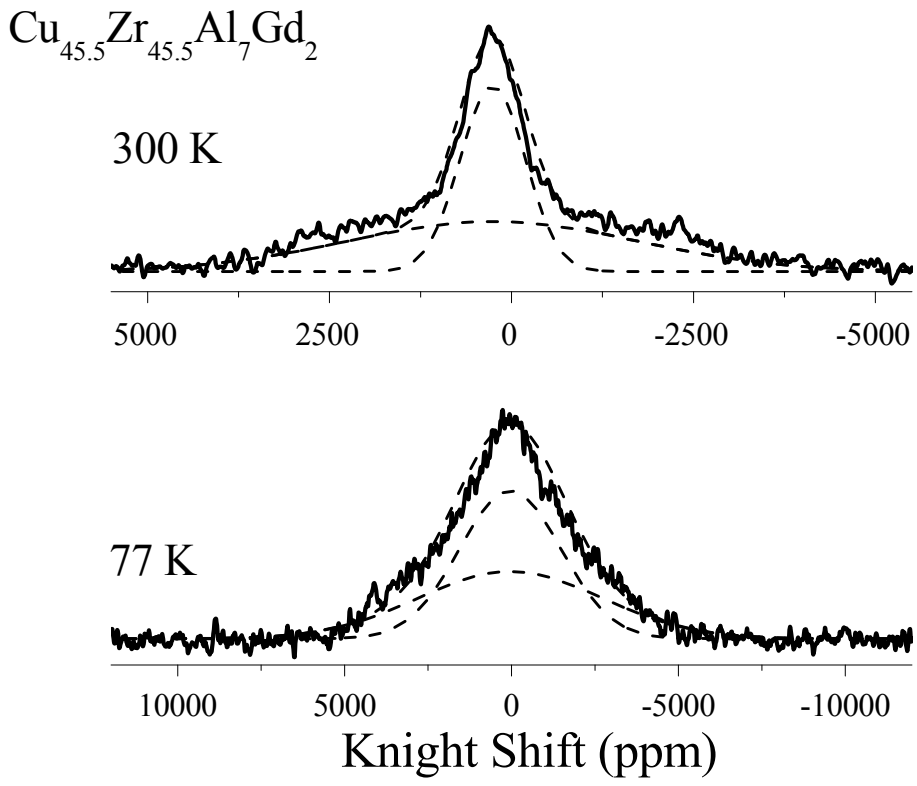

Figure 3.2 NMR frequency-shifted spectra for $Cu_{45.5}Zr_{45.5}Al_7Gd_2$ at 300 K and 77 K for comparison. Dashed lines show the two sources of broadening from first-order quadrupole interactions (satellites) and from $^{+3}$Gd moments (central transition).

3.4.2 Non-linear spectral linewidth broadening

In general, paramagnetic alloy systems are known to have homogenous magnetic character (i.e. Curie temperature of ~0K, linear isothermal magnetization curves, absence of cusp in AC susceptibility measurements, etc.). Such paramagnetic behavior would be reflected in NMR measurements as a linear dependence of the full-width at half max (FWHM) or linear spectral linewidth on temperature. This would mean that in the case of dipolar or RKKY magnetic interactions the linewidth would be directly proportional to the local time-averaged value of the magnetic moment $\langle S_z \rangle \propto T^{-1}$ as the temperature is lowered [58]. Surprisingly, NMR studies of paramagnetic alloy systems $(CuZr)_{93-x}Al_7Gd_x$ for x = 1 & 2 [16, 59] demonstrate a nonlinear dependence of linewidth on temperature. Figures 3.3 (a) and (b) below show the non-linear linewidth broadening commencing at high temperatures.

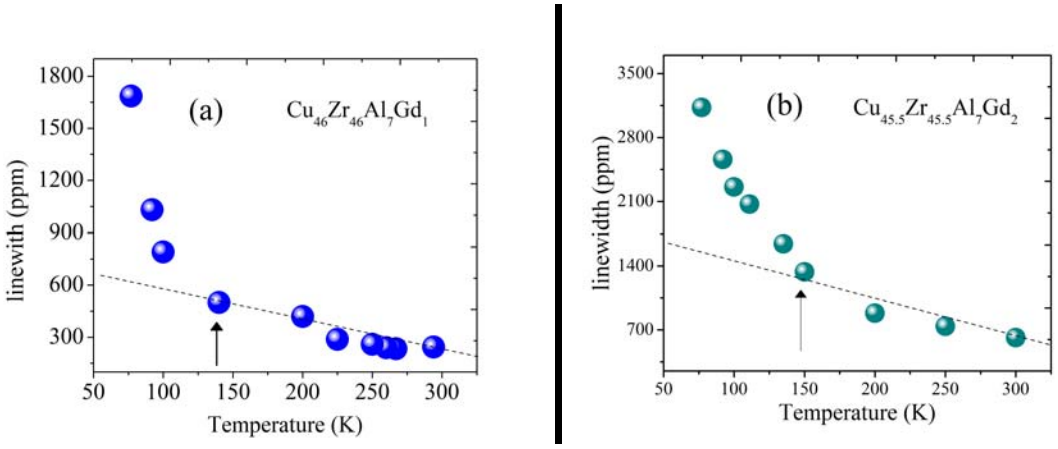

Figure 3.3 (a) & (b) Spectral linewidth for $(CuZr)_{92}Al_7Gd_1$ and $(CuZr)_{91}Al_7Gd_2$. Dashed lines provide a guide for the eye to show that nonlinear broadening occurs at ~ 150K. Purely paramagnetic alloy systems are expected to display linear linewidth temperature dependence.

The nonlinear behavior shown in Fig. 3.3 can be evaluated within the context of magnetic inhomogeneities. The nature of magnetic inhomogeneities, such as the Kondo disorder observed in non-Fermi liquids due to a distribution of magnetic susceptibilities, has

previously been evaluated using NMR shift and linewidth data [60]. Assuming A_{hf} and χ are not correlated, the Knight shift can be expressed as an average over all distributions of hyperfine coupling constants and local magnetic susceptibilities $K = A_{hf}\chi$ [60, 61]. Due to the amorphous nature of these BMGs under study, different local environments at ^{27}Al sites are anticipated to induce a spread in susceptibilities and result in nonlinear line broadening. This line broadening can be evaluated by calculating the experimental fractional NMR linewidth [60], which is expressed as

$$k / \left|K_{s-f}\right| = \left\{\left[\left(\delta\chi\right)_{rms} / \chi\right]^2 + \left[\left(\delta A_{hf}\right)_{rms} / A_{hf}\right]^2\right\}^{1/2} \qquad (1)$$

where k is the ^{27}Al NMR linewidth. Temperature-independent $k/|K_{s-f}|$ values are expected in magnetically-homogenous alloys due to spatially-independent local susceptibilities in purely paramagnetic systems.

The behavior of line broadening is shown in Figure 3.4 (a) below, which displays values of the ratio $k / \left|K_{s-f}\right|$ versus bulk magnetic susceptibility χ with temperature for x = 1 as an implicit parameter ranging from 77-300 K. Here K_{s-f} was obtained by subtracting the Fermi-contact shift K_s of 342 ppm for x = 1 and 330 ppm for x = 2 as determined from the y-intercept of K_{iso} plotted against χ.This value agrees with the shift value observed in the x = 0 sample ($(CuZr)_{93}Al_7$). In addition, the second-order quadrupole broadening of the central transition was corrected for by subtracting the linewidth found for an x = 0 sample.

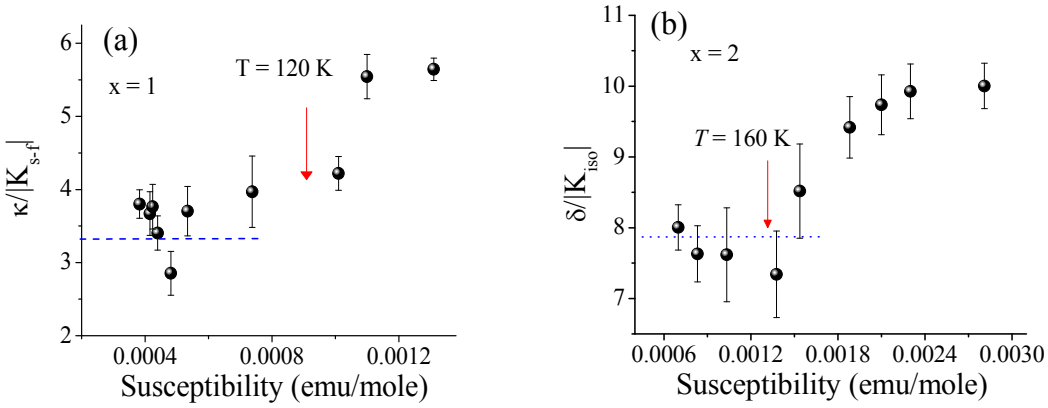

Figure 3.4 k / K_{s-f} versus χ for x = 1 (a) and x = 2 (b) with temperature as an implicit parameter after conduction-electron Knight shift and second order quadrupolar broadening corrections. The dashed lines indicate pure paramagnetic behavior between Gd ions.

The pseudo contact interaction strength was also considered, which results in a dipolar coupling interaction between the thermally-averaged magnetic moment of the unpaired electrons of a paramagnetic ion and the nucleus [62]. This results in a pseudo contact shift that can be calculated from the distances between the electronic and nuclear spins, which ranged between 3.14 and 3.15 Angstroms [63]. The pseudo contact shifts were found to be negligible giving at most a shift of 4.8 and 9.5 ppm for x = 1 and 2 at 77 K. Fig. 3.4 (a) shows that values of $k / \left|K_{s-f}\right|$ remain constant at high temperatures, as expected for purely paramagnetic behavior. Near ~120 K the ratio $k / \left|K_{s-f}\right|$ becomes proportional to χ as temperature is lowered. This signifies the onset of a magnetic phase-like transition and supports the existence of a magnetic susceptibility distribution in this temperature regime. In addition, a distribution of A_{hf} is reflected in the large constant offset of ~ 3.5 and is naturally anticipated in amorphous systems. Figure 3.4 (b) displays $k / \left|K_{s-f}\right|$ versus χ for x = 2 and

demonstrates a similar NMR linewidth enhancement occurring at a higher temperature of ~ 160 K with a corresponding non-zero distribution of A_{hf} denoted by an offset of ~ 7.75. The anomalies span a wider temperature range for x = 2, which may be due to the twofold increase in the number of magnetic moments. Proportionality between $k/\left|K_{s-f}\right|$ and χ confirms that the linewidth dependence on temperature is significantly stronger than are paramagnetic effects caused by RKKY coupling between individual Gd spins and host Al nuclei [58].

In general, the distribution of susceptibilities and A_{hf} for this alloy system is not entirely unexpected since the spatially-disordered nature of these BMGs is expected to give rise to a distribution in the magnetic environments due to fluctuations of local interatomic distances and atomic coordination [15]. Interestingly, $k/\left|K_{s-f}\right|$ is observed to saturate near 77K for both compositions and suggests that a magnetic susceptibility distribution develops only over a narrow temperature range between 160-77 and 120-77 degrees for x = 1 and 2, respectively. The nature of these susceptibility distributions is further elaborated upon through magnetization experiments.

3.4.3 Hyperfine field temperature dependence

The temperature dependence of the hyperfine field A_{hf} is also explored in Fig. 3.5 (a) and (b) in which K_{s-f} is plotted against χ and shows that A_{hf} is negative as evidenced in the slope. A linear fit was applied yielding a transferred hyperfine field of $zH_{hf} = -1.2$ kOe for x = 1 and $zH_{hf} = -0.6$ kOe for x = 2. A distribution in A_{hf} and χ mentioned previously

would suggest that these couplings might have various strengths in temperature and space. The linear behavior demonstrated in both x = 1 and x = 2 shows that A_{hf} is temperature independent and is not the source of non-linear NMR linewidth broadening in the temperature range of 77-300 K.

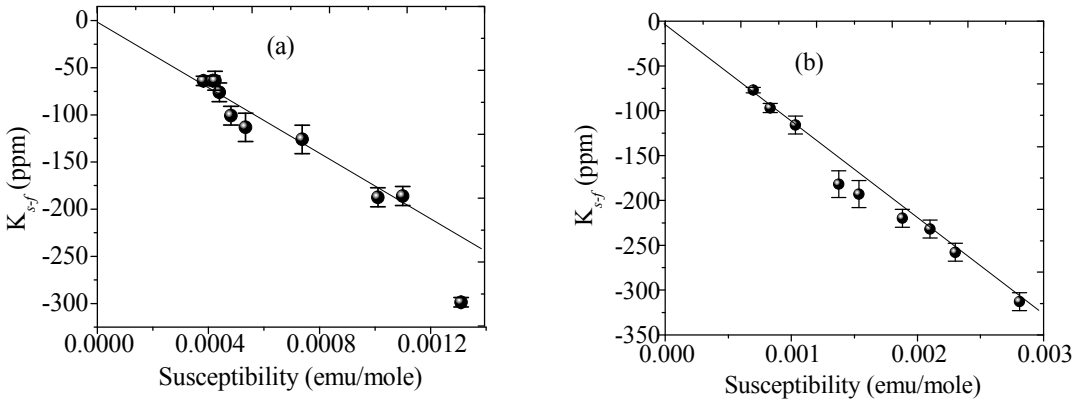

Figure 3.5 for x = 1 (a) and x = 2 (b) displays K_{s-f} versus χ with temperature as an implicit parameter. The behavior of A_{hf} is inferred from the slope.

3.4.4 Magnetization Measurements

Additional insight into the nature of magnetic linewidth broadening can be gained through magnetization experiments. Magnetization measurements of samples were carried out by J. Q. Wang at the Chinese Academy of Sciences. Molar susceptibility measurements taken at 10,000 Oe are shown in Figure 3.6 for x = 1 and x = 2. The inverse of magnetic susceptibility approaches the origin at $T = 0$ indicating the absence of long-range magnetic ordering in these systems. Further inspection reveals deviations from conventional Curie-Weiss behavior, below ~150 K in agreement with the onset temperature of the NMR linewidth enhancement and suggesting that they have a common origin. Deviations from Curie-Weiss behavior in high temperature extrapolations of the data yield Curie-Weiss temperatures of (-30 ± 1) K for

x =1 and (-5 ± 1) K for x = 2 demonstrating anti-ferromagnetic short-range order. The Curie constants obtained from the extrapolated fit yield an effective moment of 9.9 μ_B for x = 1 and 10.0 μ_B for x = 2. These values of effective moment are much larger than the 7.94 μ_B for localized Gd^{+3} ions. An enhancement of the effective moment could originate from the effect of $5d$ conduction electron polarization [64] .

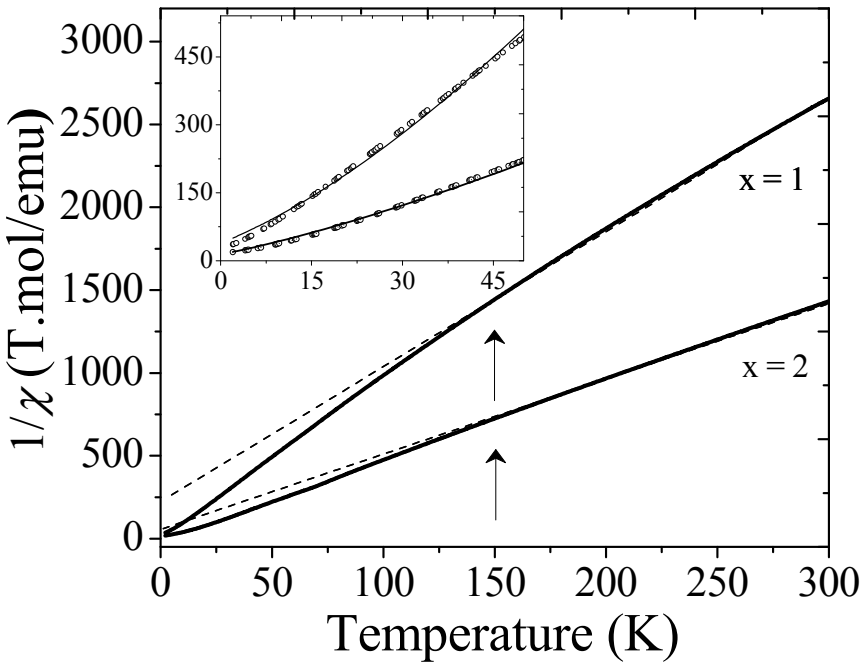

Figure 3.6 The magnetic susceptibility χ^{-1} versus T for x = 1 and 2 at 10,000 Oe. The dashed lines are linear extrapolations of the susceptibility at high temperatures giving paramagnetic Curie temperatures of (-30 ± 1) K for x = 1 and (-5 ± 1) K for x = 2. The inset contains trial fits (black solid) at low temperature to test the possibility of the "Griffiths phase". Fits to $\chi^{-1}(T) \propto (T - T_0)^{1-\lambda}$ yield λ values of -0.52 and -0.33 for x = 1 and x = 2, respectively, and do not meet the criteria of the Griffiths magnetization scaling law where $0 < \lambda < 1$ is predicted. Credit: Magnetization measurements of samples were carried out by J. Q. Wang at the Chinese Academy of Sciences.

The low-temperature behavior of the magnetic susceptibility suggests a broad range of inter-cluster interactions centered on T = 0 K that is largely reminiscent of spin glass or cluster-glass behavior observed in YAlGd, ZrCuGd, LaGdAu, and MgGdZn amorphous systems [14, 16]. The importance of short-range clusters in the high-temperature paramagnetic regime is emphasized by the enhanced effective moments for x = 1 and x = 2 obtained from the Curie constants that are larger than 7.94 μ_B for localized Gd^{+3} ions. This suggests the presence of short-range magnetic correlations as seen in Griffiths systems, including randomly-doped manganites and heavy-fermion alloys [46, 65, 66]. The Griffiths phase is characterized by regions that have pre-formed magnetic clusters that grow in number with a decrease in temperature [65]. Although this gives rise to a globally paramagnetic state, locally there are competing interactions. Trials fits to the low temperature susceptibility data in the "Griffith's phase" are shown in the inset of Fig. 3.6 and demonstrate that local magnetic characteristics in these BMGs are not in agreement with Griffiths scaling behavior characterized by $\chi^{-1}(T) \propto (T - T_0)^{1-\lambda}$ [48]. The expected λ value for the Griffiths phase is $0 < \lambda < 1$ whereas the fitting yields λ values of -0.52 and -0.33 for x = 1 and x = 2, respectively.

Further investigations of the magnetic behavior was also carried out through isothermal magnetization measurements $M(H)$ from H = 0 to 70,000 Oe shown in Figure 3.7 for x = 1 and x = 2 at 300 K and 80 K and in Figure 3.8 at 2K. A Brillouin function corresponding to a magnetic moment of 7 μ_B is also included for comparison. Although NMR observations in Fig. 3.4 (a) and (b) demonstrate the development of local magnetic

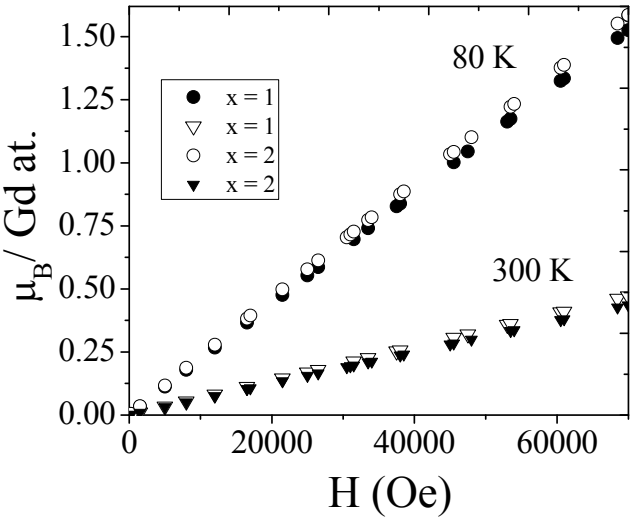

Figure 3.7 Magnetization isotherms for x = 1 and x = 2 at 80 K and 300 K for fields up to 70,000 Oe show paramagnetic behavior. Credit: Magnetization measurements of samples were carried out by J.Q. Wang at the Chinese Academy of Sciences.

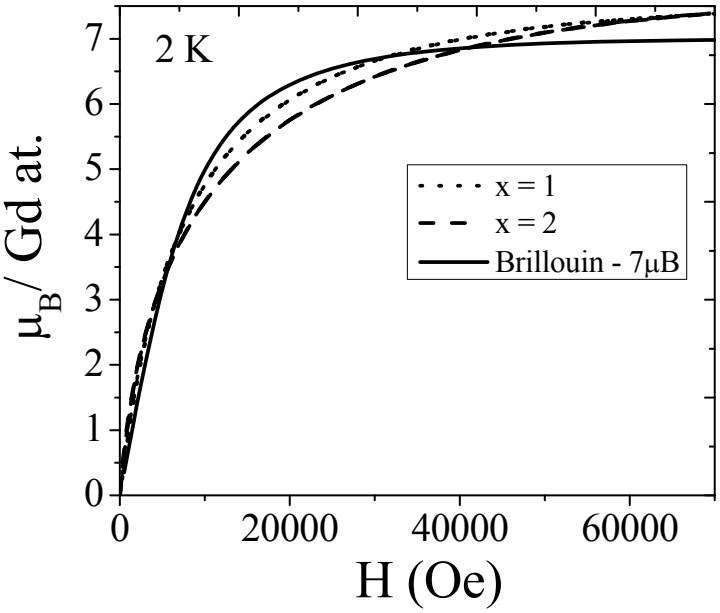

Figure 3.8 Magnetization isotherms for x = 1 and 2 at 2 K are compared to a Brillouin function with a magnetic moment $gJ = 7\mu_B$. Direct comparison shows the presence of strong non-Brillouin behavior at 2 K for both x = 1 and 2. Credit: Magnetization measurements of samples were carried out by J.Q. Wang at the Chinese Academy of Sciences.

susceptibility inhomogeneities at high temperatures, inspection of Fig. 3.7 and Fig. 3.8 reveals that isotherms at 80 K and 300 K exhibit purely paramagnetic behavior. Fig. 3.8 also shows that at 2K the magnetization does not reach saturation even at the maximum applied field and displays non-Brillouin behavior possibly due to frustrated RKKY magnetic correlations as also observed in amorphous spin-glass systems [50, 67]. Random magnetic anisotropies are not expected to play an important role in suppressing the magnetization due to a non-existent orbital angular momentum $(J = S,\ L = 0)$.

3.4.5 Spin-glass-like behavior

A comparison to RKKY theory for spin-glass for the dilute impurity limit can be made using the relationship for reduced magnetization [68] given by $M = 1 - (2/3)V_0 n(2J+1)/(g\mu_B H)$, which is valid for $V_0 n << g\mu_B$ and $g\mu_B H >> k_B T$ where n is the impurity number density and V_0 is the amplitude of the RKKY interaction strength. Figure 3.9 shows the saturation moment for x = 1 and 2 as obtained from a linear extrapolation of M versus H^{-1} at high fields (60 - 70 kOe) at 2 K. For x = 1, the saturation moment of 7.9 μ_B is larger than the expected value of 7.0 μ_B for Gd^{+3} and may be attributed to magnetic short-range order, as implied by the high-temperature molar susceptibility fits given in Fig. 3.6, or conduction electron polarization as seen in Gd-La and Gd-Y alloys [69, 71]. The relevance of evaluating isothermal magnetization data in this way was further verified using the y-intercept of M versus H^{-1} and normalizing by $\mu_B J$. The intercept is 1.12 and 1.16 for x = 1 and 2, respectively, implying a small correction to the reduced magnetization expression. In addition to the high quality of fit from the linear extrapolation, these results strongly suggest the relevance of the RKKY interaction with spin-glass-like

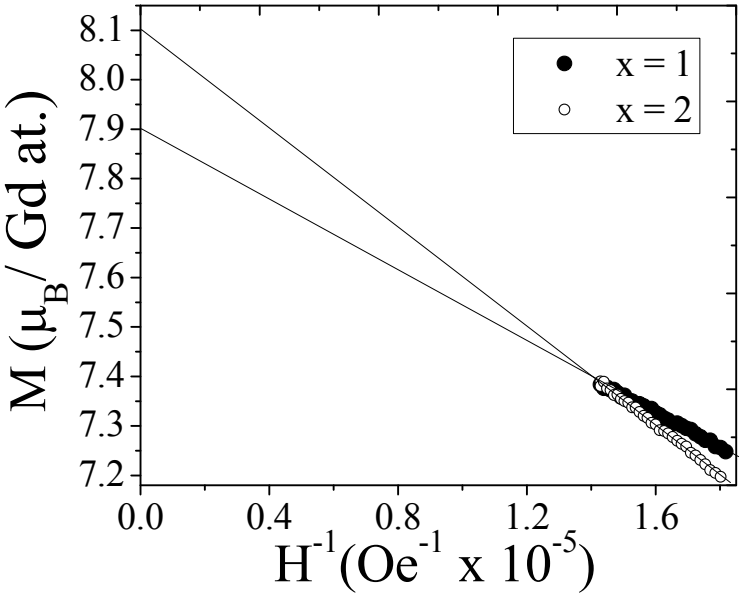

Figure 3.9 A linear extrapolation of M versus H^{-1} at high fields (60-70 kOe) results in a large saturation moment of 7.9 μ_B and 8.1 μ_B for x = 1 and 2, respectively.

characteristics in this BMG system. The saturation behavior for x = 2 yields a similarly larger moment of 8.1 μ_B. Interestingly, a field much greater than 70,000 Oe is necessary to obtain saturation at 2 K which strongly suggests the importance of frustration such as spin-glass behavior in CuZrGd alloy systems [44] although past studies of similar BMG systems and recent AC susceptibility measurements confirm that x = 1 and 2 remain paramagnetic down to 2K [16, 59]. The slope determined from the linear fit gives $V_0 = 3\times10^{-38}$ and 2.3×10^{-38} erg cm^3 for x = 1 and x = 2, respectively. For a free electron the Fermi energies are estimated to be $E_F = 9.34$ eV and 9.40 eV and the exchange integral J_{s-f} can be determined from $J_{s-f}^2 = V_0 32\sqrt{2}E_F k_F^3 / \left[9^2 J\left(J+1\right)\right]$ [44, 69], giving $\left|J_{s-f}\right| = 0.15$ eV and 0.13 eV for x = 1 and x = 2, respectively. This interaction strength is comparable to that seen in amorphous alloys such as LaAuGd [50, 70], but is ~3-4 times larger than the interaction strength determined in

CuZrGd [44] with considerably higher Gd concentration and in (La, Gd)Al [69] alloy systems containing comparable Gd content. It is interesting to note that a smaller Gd content (x = 1) yields a slightly stronger interaction strength, which is consistent with the NMR and susceptibility measurements.

3.5 Conclusions

In general, NMR and magnetization measurements both confirm the development and the importance of AF short-range order of $(CuZr)_{93-x}Al_7Gd_x$ glasses with x = 1 and 2, beginning at high temperatures near 150K. This is supported by the temperature-independent hyperfine couplings A_{hf} for x = 1 and x = 2 that show the source of broadening is due to the local magnetic susceptibility distribution at high temperatures. Non-linear linewidth broadening shown in Fig. 3 (a) and (b) clearly proves that this distribution is prominent at high temperatures and evolves over a narrow temperature range (40-80 degrees). Furthermore, non-Brillouin isothermal magnetization behavior at low temperatures seems to suggest that the AF cluster development in both x = 1 and 2 is magnetically frustrated. The intra-cluster interaction strength for x = 1 and 2, as determined by the exchange integral $\left|J_{s-f}\right|$, shows that this frustration is quite strong as it is considerably higher than other Gd-bearing amorphous systems [44, 69] showing long-range spin-glass behavior.

.

CHAPTER 4

Anelastic deformation of La-based metallic glasses

4.1 Introduction: Free Volume and Shear Transformation Zones (STZs)

One of the great challenges in the study of bulk metallic glasses (BMGs) is a basic understanding of the deformation mechanism in amorphous systems where dislocations are absent [71]. Plastic flow in metallic glasses can proceed by two mechanisms: inhomogenous and homogenous deformation [18]. Inhomogenous deformation takes place at low temperatures and high stresses resulting in highly localized shear banding (at 45^{o} with respect to the tensile axis), since only a small fraction of the volume of the sample participates in flow [18]. At low stress and higher temperatures (near T_g) the entire volume of the sample can undergo homogenous deformation [18]. These two mechanisms showing macroscopic deformation are illustrated in Figure 4.1. The strain response during homogenous deformation exhibits both elastic and inelastic (anelastic and viscoplastic) strain components [72] where the elastic strain recovers instantaneously, the anelastic strain undergoes time-dependent recovery, and the viscoplastic strain is permanent [72-74]. This can be compared to crystalline systems, where plastic flow occurs by propagation of dislocations or line

defects that have a definite slip plane [75]. This Chapter will focus on using NMR to understand the anelastic response to homogenous deformation[1].

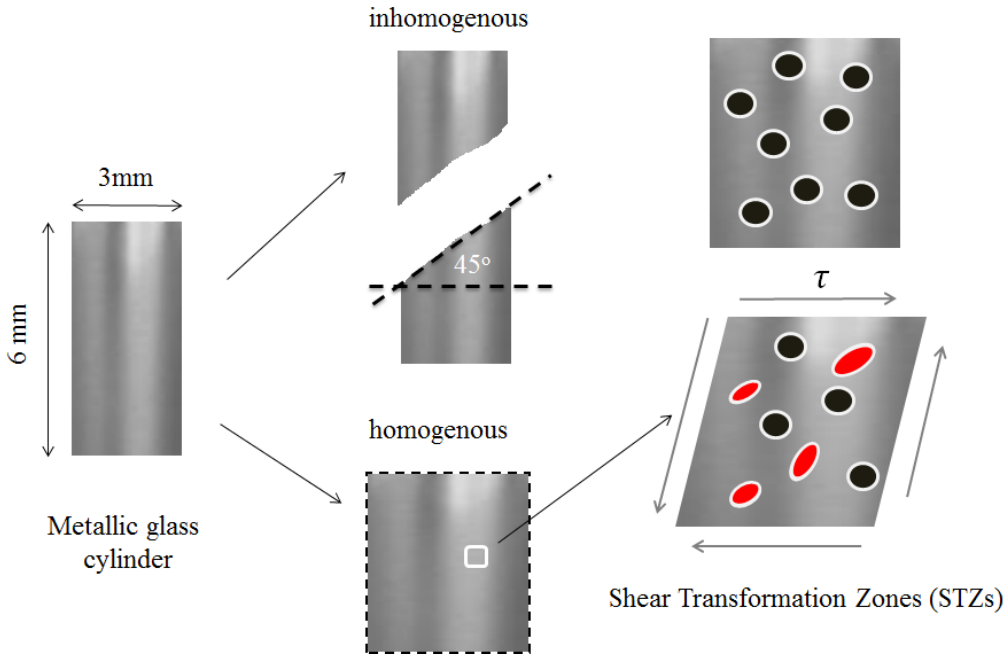

Figure 4.1 Schematic illustrating the two deformation mechanisms observed in metallic glasses. Shear transformation zones (STZs) correspond to the regions of local atomic rearrangements that take place during a shear.

Phenomenological models of inelastic deformation describe the fundamental flow mechanism in metallic glass as a process involving a local rearrangement of atoms that accommodates strain though single-atomic diffusion [18] or as a cooperative shear process of atomic clusters referred to as shear-transformation zones (STZs) [19]. This is also illustrated in Fig. 4.1. These deformation mechanisms are believed to be facilitated by a distribution of

[1] This work was submitted for publication to Physical Review during June, 2012 and is currently pending review.

free volume [76] that is a widely-used scalar parameter for quantifying structural relaxation [1] and creep kinetics [77, 78] in metallic glass. Free volume is defined as the volume that is in excess of the material's corresponding crystalline state or ideally-ordered structural state. The red highlighted areas in Fig. 4.1 represent STZs that are in close proximity to regions of large free volume and therefore can easily undergo shear. Due to the amorphous nature of metallic glass, there is believed to be a continuous distribution of different local structure and free volume [73]. In essence, this is what makes up the defects in metallic glass [73, 79].

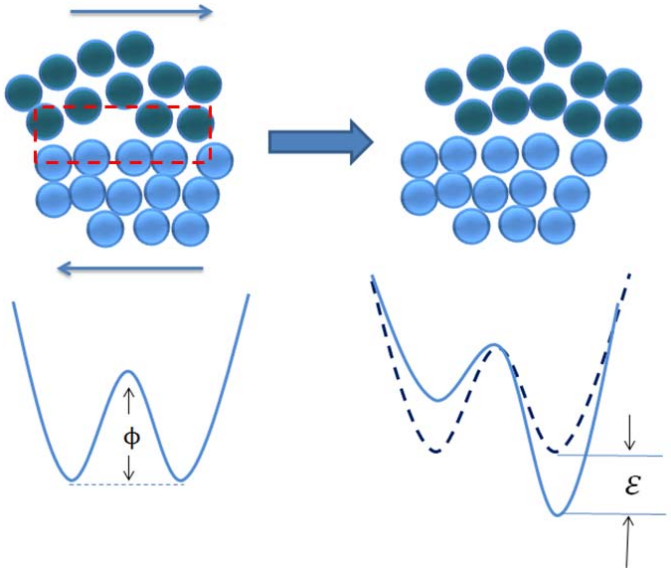

Figure 4.2 At the atomic-level, local regions of metallic glass have symmetric free energies ϕ. Applying a stress lowers the free energy by ε in the direction of shear and causes atomic rearrangements [80].

Deriving an understanding of how the local structure/free volume evolves under shear stress might provide tremendous insight into the deformation mechanism in metallic glass. Currently, anelastic and viscoplastic deformations of metallic glasses are mostly interpreted in terms of STZs [71]. As shown in Figure 4.2, the distribution of structure and free volume in glass gives rise to local free energies ϕ that are approximately symmetrical. The

application of shear stress induces an asymmetry of the local free energy by an amount ε and causes mechanical polarization of STZs. This effectively increases the probability for atoms to reshuffle along the direction of shear. Backward atomic shuffling is possible, but has a much lower probability [80].

During an applied stress local regions that are sheared are not isolated. STZs are embedded in an elastic surrounding that exerts a back stress on the transformed volume. The back stress developed during anelastic deformation is anticipated to aid in the macroscopic recovery of the shape when the applied stress is released [73]. This gives rise to delayed-elastic or anelastic recovery. Previous studies have shown that the anelastic recovery of glass exhibits a continuous spectrum of activation energies and relaxation times [73, 74] reflecting the resulting distortion of free volume and local structural distribution due to STZs. If two or more neighboring transformed STZs emerge and interact with each other, dissipative release of the back stress could occur resulting in viscoplasticity [81]. This chapter will cover the anelastic response of La-based metallic glass to constant compression at room temperature.

4.2 Experiments: Constant Compression, Modulated Differential Scanning Calorimetry, and NMR

For constant compression experiments, $La_{50}Ni_{15}Al_{35}$ BMG rods 3mm in diameter and ~6 mm length were prepared by arc-melting the elemental components under a Ti-gettered argon atmosphere. A cylinder, 3 mm in diameter and 50 mm long, was cast in a water-cooled copper mold. The samples to undergo constant compression experiments were cut from the middle of the cylinder with a diamond saw, and the ends of the samples were carefully polished flat and normal to the longitudinal axis for uniform loading in compression. It was recently found that homogenous deformation of metallic glass rods at room temperature

could be obtained at high stress by applying a stress just below the yield strength [77]. The samples were therefore compressed at a strain rate of $1\times10^{-4}s^{-1}$ (Instron electromechanical testing system 3384) to a stress equal to 0.90 of the metallic-glass yield strength ($\sigma = 900\ Mpa$), and held at this stress for 10, 24, and 48 hours. The effect of different stress was also explored by studying rods that were compressed for 24 hours at a stress equal to 0.80 ($\sigma = 800\ Mpa$) and 0.90 ($\sigma = 900\ Mpa$) of the metallic-glass yield strength. The amorphous nature of these BMGs was confirmed using DSC and X-ray diffraction. An as-cast rod (no mechanical treatment) and a rod annealed at T_g – 20 (240 ^oC) degrees for 48 hours were used as reference samples. SEM of the rods after compression confirmed the absence of any inhomogenous deformation development such as cracking or localized shear banding. Figure 4.3 shows some SEM images of the rods after mechanical treatment.

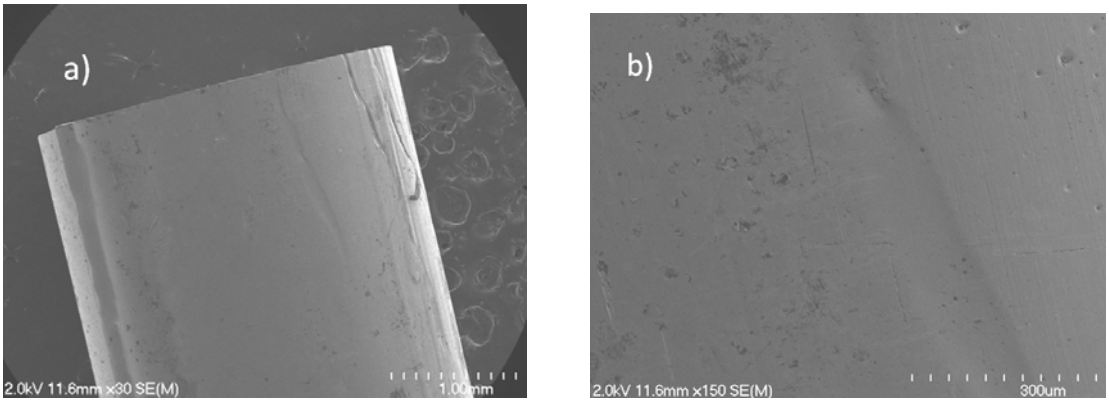

Figure 4.3 (a) and (b) SEM images of a compressed BMG rod at 900 MPa for 24 hours.

The SEM images above do not show any evidence of shear banding on the surface of the BMG rods. Shear banding results in large plastic strain that causes significant local atomic rearrangements that are favorable for inducing Al crystallization [82]. Figure 4.4 shows X-ray diffraction patterns of an as-cast sample showing broad diffraction peaks typical in

amorphous systems [83]. These diffraction peaks are compared to those of the sample mechanically treated at 900 MPa, which shows no obvious sign of crystallization.

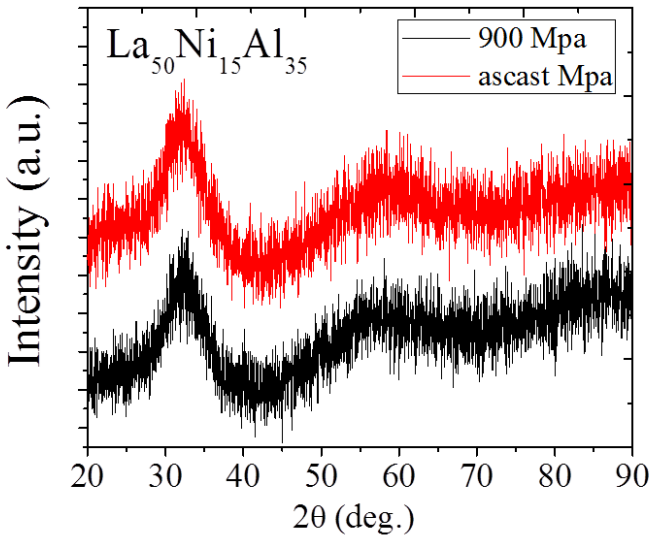

Figure 4.4 X-ray diffraction of a BMG sample compressed at 900 MPa for 24 hours compared with an as-cast BMG sample.

The compression experiments and length measurements made using a micrometer were carried out by Haibo Ke at the Chinese Academy of Sciences. Figure 4.5 shows an example of a strain curve for constant compression at room temperature for 24 hours. The strain response is characterized by three components: elastic (~ 1.90%), anelastic (~0.10%), and a sum of viscoplastic and anelastic (~0.04%) components [72]. It is important to note that anelastic strain continues even at the onset of viscoplastic strain [72]. Table 4.1 summarizes the length measurements taken ten times before compression, immediately after 24 hour

compression, and 10 and 24 hours after the 24-hour compression. The micrometer used has a length scale of 10^{-6} m. The average irreversible strain determined after 24 hours is ~0.03% also in agreement with Fig. 4.5.

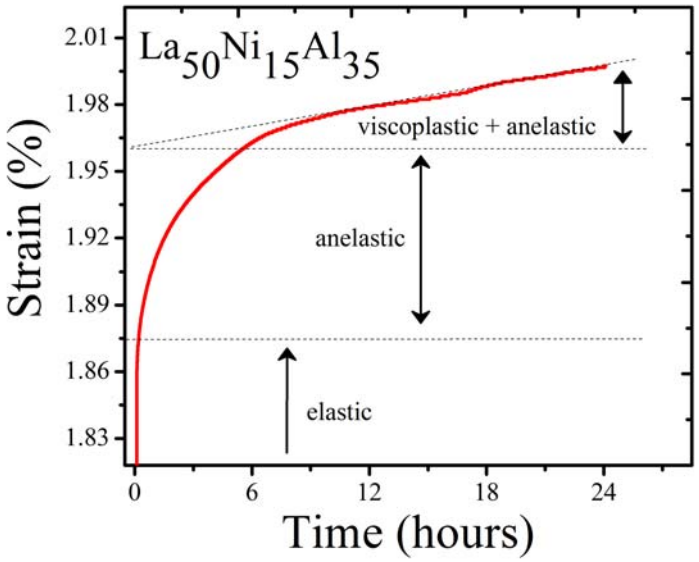

Figure 4.5 (a) Room temperature constant-compression experiments for 24 hours. The elastic (~1.90%), anelastic (~0.10%) (delayed elastic), and anelastic and viscoplastic strain (~0.04%) responses are noted. Credit: Mechanical treatment of BMG rods were carried out by Haibo Ke at Chinese Academy of Sciences.

For each sample the anelastic and viscoplastic components were also verified systematically by micrometer measurements after unloading and well after macroscopic recovery (>48 hrs).

^{27}Al NMR nutation experiments were performed in a magnetic field of 8.9 T at 300 K. Nutation was performed using Hahn-echo pulse sequence $(t_1)_x - \tau_1 - (t_2)_x - \tau_2 - aquisition_{-y}$, where t_1 and t_2 are the radiofrequency (rf) pulse widths, x and -y are the pulse and receiver

phases, respectively, where τ_1 and τ_2 are the time delays. The echo intensity was acquired at $\tau_1 = \tau_2$. The bulk of the echo intensity comes from the central transition $|-1/2\rangle \leftrightarrow |1/2\rangle$, but

Table 4.1. Micrometer measurements of a $La_{50}Ni_{15}Al_{35}$ BMG rod taken before compression, immediately after, and 10 and 24 hours after 24-hour compression. The average irreversible strain after 24 hours is ~0.03%. Credit: Micrometer measurements were carried out by Haibo Ke at Chinese Academy of Sciences.

	Before compression (mm)	**After 24hours compression (mm)**	**Relaxation for 10hours (mm)**	**Relaxation for 24hours (mm)**
1	6.4524	6.4416	6.4484	6.4506
2	6.4524	6.4424	6.4480	6.4504
3	6.4526	6.4426	6.4482	6.4500
4	6.4524	6.4422	6.4482	6.4496
5	6.4516	6.4426	6.4484	6.4504
6	6.4524	6.4430	6.4486	6.4504
7	6.4520	6.4426	6.4484	6.4498
8	6.4522	6.4430	6.4486	6.4496
9	6.4520	6.4430	6.4480	6.4500
10	6.4524	6.4424	6.4484	6.4504
average	**6.4522**	**6.4425**	**6.4483**	**6.4501**

also includes satellite transitions that are important for determining the quadrupole frequency ω_Q, (defined in Section 4.3). Measurements were obtained using an rf pulse strength of

$\omega_{rf} / 2\pi = 50$ kHz and by setting $t_1 = 1\mu s$ and allowing t_2 to vary from $0.5\mu s$ to $6.5\mu s$ in increments of $0.5\mu s$ with a recycle delay of 300ms. A numerical fit of the nutation curve was employed to extract the electric-field gradient (EFG) parameters. It is crucial to note here that NMR experiments were carried out well after anelastic macroscopic length recovery. The relative changes in anelastic-induced enthalpic processes or free volume [84] were also evaluated using a TA q200 heat flux modulated differential scanning calorimeter (MDSC) at a heating rate of 4 C/min, temperature amplitude variation of +/-2 deg, and period of 60 seconds.

4.3 Experimental Results

4.3.1 NMR nutation results

Figure 4.6 shows ^{27}Al NMR nutation profiles of the central transition intensity versus the width of the first pulse t_1 ranging from 0 to 6.5 μs for as-cast, annealed, and compressed $La_{50}Ni_{15}Al_{35}$ BMG samples. ^{27}Al is a spin $I = 5/2$ nucleus and permits coupling between the electric quadrupole moment and the EFG due to the quadrupole interaction. For weak perturbation of the Zeeman interaction the intensity represents the evolution of the density operator $\rho(t_1, \tau_1, t_2, \tau_2)$ due to first-order quadrupole interactions as discussed in Chapter 2. The fitting parameter $\omega_Q = \frac{3e^2qQ}{2I(2I-1)\hbar}$ provides direct determination of the EFG, reflecting any local compression-induced structural changes. The EFG experienced at ^{27}Al sites is most

sensitive to the positions of the aluminum atom's nearest neighbors and is negligible in instances of high symmetry, e.g., cubic, icosahedral order, etc.

Fits of the nutation curves [35] are shown as solid lines in Fig. 4.2 for an asymmetry parameter η of 0.9 and the extracted values of ω_Q are listed in Table 4.2 with the corresponding strain changes. Complete anelastic recovery of strain is observed for a compression time of 10 hours and results in a decrease of ω_Q from 820 to 615 kHz compared to the as-cast samples. A decrease in ω_Q corresponds to a reduction of the largest principal

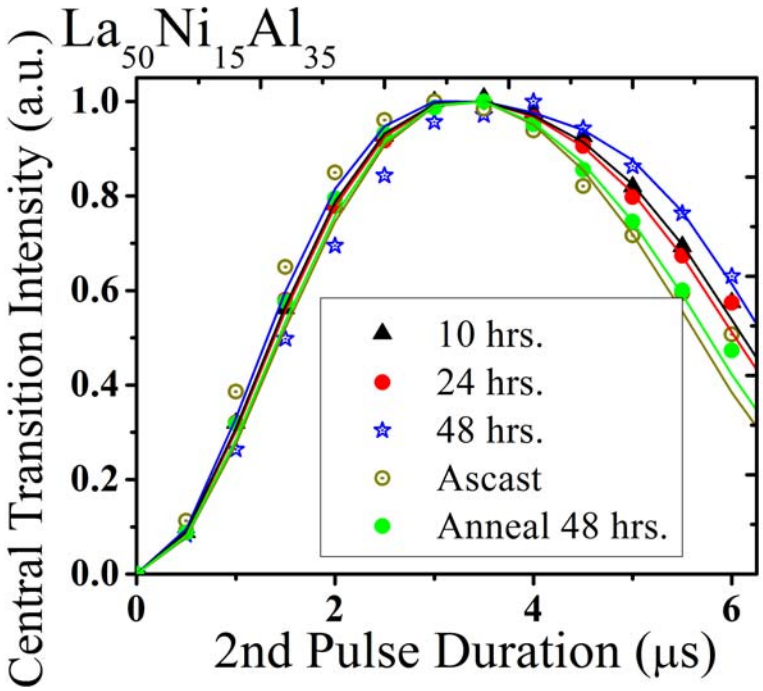

Figure 4.6: Nutation experiments where the central transition intensity is plotted versus the second pulse duration in a Hahn-echo sequence. The pulse duration t_1 increases from 0 to 6.5 μs by steps of 0.5 μs. Solid lines are fits of ω_Q and are summarized in Table 4.2 in addition length change percentages.

component of EFG tensor, V_{zz}. This provides direct experimental evidence that anelasticity is responsible for the structural changes induced locally at Al sites. Fitted values of ω_Q also decrease to 653 kHz for 24 hours and 528 kHz for 48 hours of strain time. Annealing for 48 hours below T_g gives a ω_Q of 765 kHz and shows that local site symmetry is slightly enhanced by annealing although to a much lesser degree than by compression. Figure 4.7 shows nutation profiles due to applied stresses for a different batch of $La_{50}Ni_{15}Al_{35}$ BMGs. ω_Q for an as-cast sample of 700 kHz changes to 615 kHz at 800 MPa and 562 kHz at 900

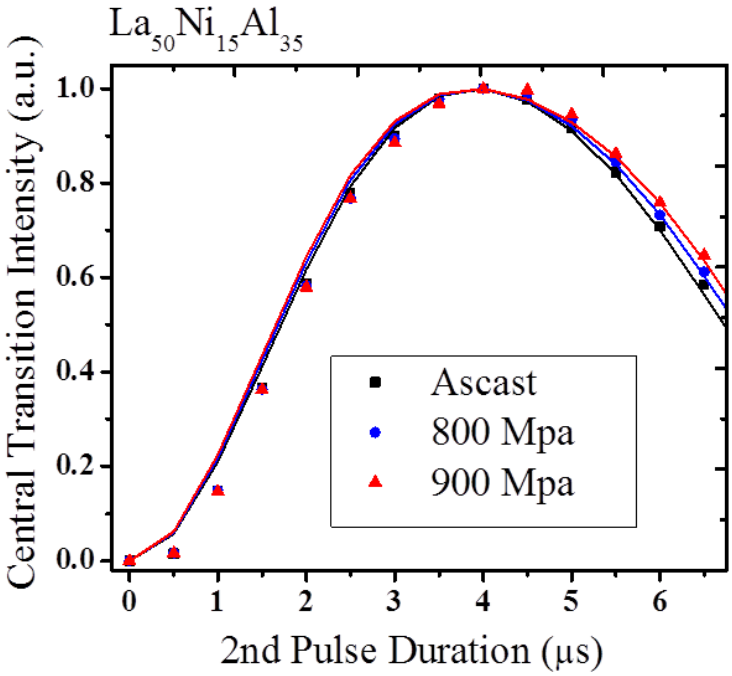

Figure 4.7: Nutation profiles due to different applied stresses for 24 hrs where ω_Q changes from 700 kHz in the as-cast state to 620 kHz after compression at 800 MPa and 560 kHz after compression at 900 MPa.

MPa for a corresponding compression time of 24 hrs. These results demonstrate that compression treatment leads to smaller ω_Q, which implies higher local symmetry at the Al sites. Higher external stress and longer compression time lead to a larger decrease of ω_Q.

To understand the results presented in Fig. 4.6 and 4.7 it is necessary to consider the general expression for the strain rate $d\gamma / dt$ [80]

$$\frac{d\gamma}{dt} \propto \gamma_a \int_0^\infty f_f \nu e^{-(\Phi-\varepsilon)/kT} d\Phi - \gamma_a \int_0^\infty f_u \nu e^{-(\Phi+\varepsilon)/kT} d\Phi \qquad (4.1)$$

where γ_a is the strain contribution due to one atomic jump, ν is the Debye frequency, $(\phi - \varepsilon)$ is the activation energy barrier of an STZ, Φ is free energy of an STZ, and ε is the energy change of the barrier height due to the application of shear stress. Φ and ε are illustrated in Fig. 4.2. The first and second terms on the right-hand side of (4.1) are the strain components due to a distribution f of atoms that are in favorable (f_f) and unfavorable (f_u) positions. Here, favorable and unfavorable positions refer to atoms that move in the same or opposite direction as the applied shear stress. At low stresses the second term on the right-hand side becomes important [85].

It is important to note that the strain and recovery rates expressed in (4.1) are sensitive to the free energy of the STZ [19, 85]. This free energy takes on different forms depending on the level of stress [85]. At low stress or high temperatures near T_g the STZs are diffuse large volumes that are believed to contain ~100 atoms [86] with an activation energy given by

$$\phi = (0.67\gamma_o^T \mu + 0.5\hat{\tau})\gamma_o^T \Omega_F \left(1 - \frac{\sigma}{\hat{\tau}}\right) \qquad (4.2)$$

where γ_o^T is the is the transformation shear strain (ranges between 0.10 and 0.125), μ is the shear modulus, Ω_F is the transformation volume, $\hat{\tau}$ is the shear strength, and σ is the applied shear stress. At high stresses and low temperature STZs are confined to a small region (red boxed region of Fig. 4.2) that resembles a dislocation loop. The corresponding activation energy is given by

$$\phi = 4.56\hat{\tau}\Omega_F\left(1-\frac{\sigma}{\hat{\tau}}\right)^2. \qquad (4.3)$$

Given the expressions (4.1)-(4.3) the macroscopic length changes as noted in Table 4.1 likely come from the most-easily-sheared STZs with free energies ϕ comparatively smaller than those that give rise to the local structural changes as revealed by the change of ω_Q. The fact that large shear stresses ($\tau \sim \sigma/2 = 450$ MPa) were used in these experiments emphasizes that the STZs correspond to small confined regions with free energies in accordance with (4.3). It is important to acknowledge the sensitivity of NMR at Al sites in detecting atomic-level structural changes for such a small anelastic strain of 0.1 %. Although it cannot be determined from NMR experiments, changes of ω_Q for such small macroscopic length changes implies that a large fraction of the Al sites undergo structural changes.

Figure 4.8 shows nutation experiments for compressed samples demonstrating complete structural relaxation well after a 1 month period. These results are summarized with the nutation data of the as-cast and annealed samples and a nutation curve fit parameter of ω_Q = 810 kHz for comparison. This clearly supports the idea that for large applied stresses the residual back stress developed during anelastic deformation promotes not only the fast macroscopic recovery of the shape, which is comparable to the timescale of the compression

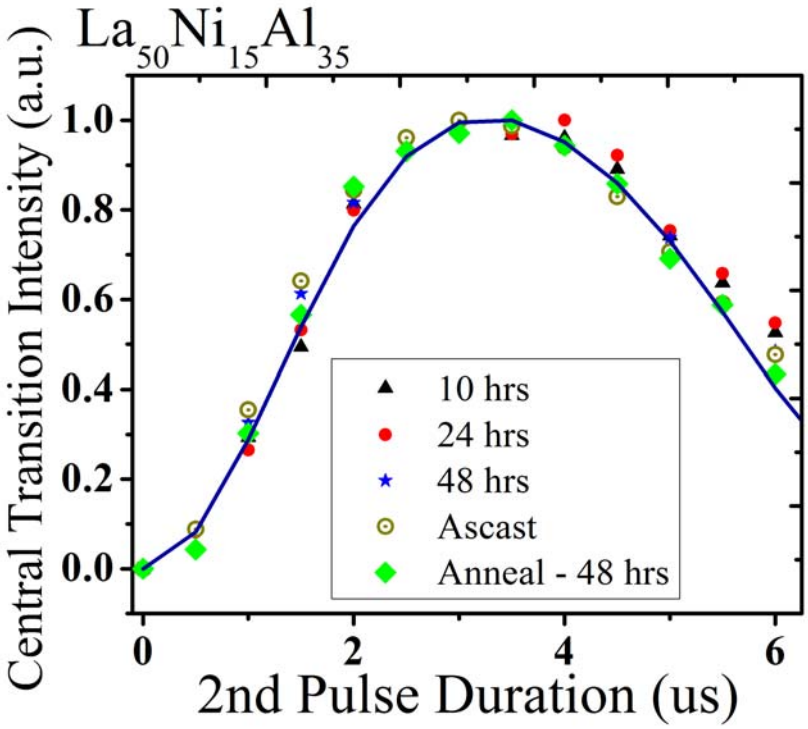

Figure 4.8: Nutation experimental data for as-cast, compressed, and annealed samples (data points), which show no changes in structural symmetry due to anelastic relaxation for > 1 month. The fit of the nutation curve gives ω_Q = 810 kHz.

experiment, but also causes relaxation of the slower anelastic-induced local structural changes that exceeds the duration of the experiment. To some degree, the different relaxation timescales (macroscopic versus microscopic) observed are not surprising since recent macroscopic anelastic studies of metallic glasses demonstrate that these relaxation processes have an extended spectrum of free energies [73, 87] that gives rise to a wide distribution of relaxation rates [88]. The NMR results presented here are important in emphasizing that the characteristic time laws for anelastic strain during stress and recovery are fundamentally different due to the different length scales and associated free energies [73, 87], although they are approximately identical for small applied shear stresses ($\phi << kT$) [73].

An understanding of the slow relaxation time that leads to microscopic recovery of the local structure as demonstrated in Fig. 4.8 can be made by considering the role of stress-induced short-range atomic diffusion mechanisms such as Snoek or Zener relaxation observed in crystalline solids [88]. Snoek and Zener relaxation has shown substantial relevance in internal friction studies of metallic glasses [89-92]. Snoek relaxation refers to a reorientation of a single atom, while Zener relaxation involves several atoms that give rise to changes of short-range order. For the work presented here, Snoek and Zener relaxation can be generalized to Al-centered clusters. The free energy produced by Al-centered clusters comes from the product of the various strain orientations due to local structural changes, and the residual back stress [73] after the release of applied stress. During anelastic relaxation the minimization of free energy is facilitated by thermal fluctuations that cause local diffusive jumps due to Snoek or Zener relaxation of Al atoms and atoms in their first coordination shell to reach a more energetically favorable strain orientation. However, the pertinence of Snoek or Zener relaxation for macroscopic anelastic recovery cannot be elaborated upon due to fast relaxation on the order of a few days (Table 4.1).

Table 4.2. Fitting values of quadrupole frequency $\omega_Q / 2\pi$, length changes, and Knight shift values (ppm).

$La_{50}Ni_{15}Al_{35}$ (Fig 4.6)	$\omega_Q / 2\pi$ (kHz)	% Length Change	Knight Shift (ppm)
As-cast	820	-	657
10 hrs.	615	0.0%	657
24 hrs.	653	-0.03%	657
48 hrs.	528	-0.04%	657
Anneal – 48 hrs.	765	-0.09%	647
As-cast (Fig. 4.7)	700	-	657
800 Mpa	615	-0.03%	657
900 Mpa	562	-0.03%	657

4.3.2 Modulated Differential Scanning Calorimetry (MDSC)

Differential scanning calorimetry (DSC) studies are useful in understanding the thermodynamic transitions that take place in materials, such as the glass transition, crystallization, and melting. DSC measures the total heat flow difference between a sample and an empty sample pan as a function of temperature and time using a linear heating rate. Modulated differential scanning calorimetry (MDSC) incorporates a temperature modulation in addition to the linear heating rate to separate two different components of the heat flow. The total heat flow equation [93] for MDSC is given by

$$dQ / dt = C_p dT / dt + f(t,T) \qquad (4.4)$$

where Q is the heat absorbed by the sample, t is time, C_p is the heat capacity due to vibrational, rotational, and translational motions in the sample, T is the temperature, and $f(t,T)$ is the kinetic response that is a function of both temperature and time. C_p-related processes are reversible. This means that they are not kinetically hindered (i.e. are instantaneous) and for any heating rate dT/dt does not result in a hysteresis during heating and cooling. On the other hand, $f(t,T)$ refers to kinetic processes that are irreversible (or non-reversing in the language of DSC).

Characterizing the change of non-reversing heat flow between the compressed samples will be useful to understand if there is any relationship between anelastic-induced structural changes exhibited in Fig. 4.6 and changes, if any, of free volume. Figure 4.9 shows the MDSC curves in the temperature range 100 to 450 ^{o}C for the as-cast, annealed, and compressed BMG samples. The inset to Fig. 4.9 shows the exothermic events preceding T_g at 250 ^{o}C that represent the excess free volume trapped in BMG during rapid solidification that is annealed out during heating [1, 84]. In comparison to the as-cast state, the annealed sample shows significant structural relaxation as evidenced by the enhanced endothermic peak. Small viscoplastic strains of 0.03% for 24- and 0.04% for 48-hour compression experiments are anticipated to induce some degree of free volume change [77]. However, the enthalpic heat recoveries of the compressed samples do not show any corresponding variation with the enhancement of local symmetry as shown in Fig. 4.6.

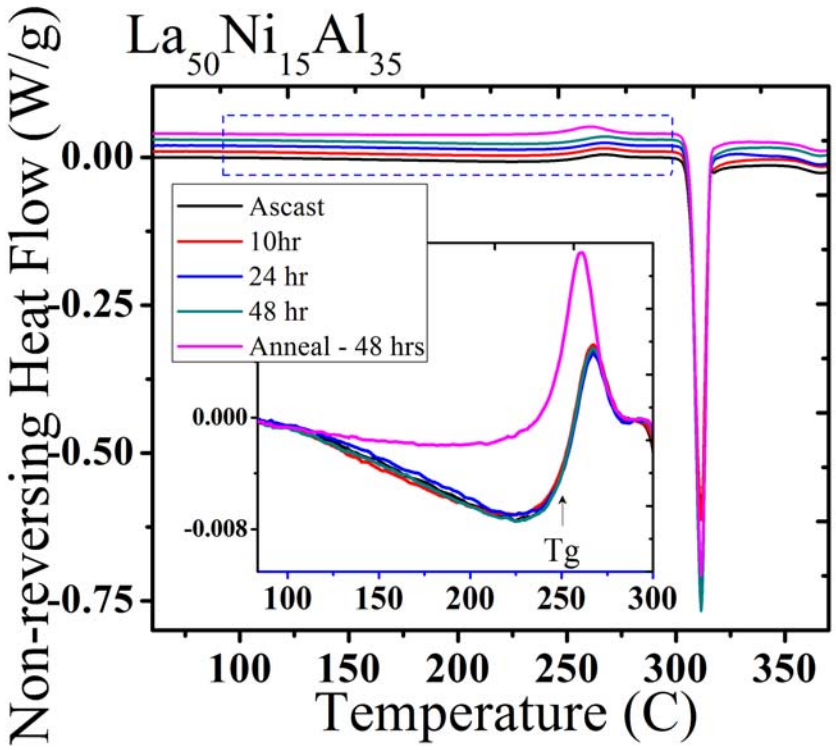

Figure 4.9: MDSC curves of non-reversing heat flow for as-cast, annealed, and compressed samples. The compressed samples do not show changes in enthalpic recovery near T_g. This can be compared to the annealed sample that shows significant structural relaxation.

4.3.3 ^{27}Al NMR Spectroscopy

An understanding of the how the local electronic structure is affected by compression and thermal relaxation can be obtained through ^{27}Al NMR spectroscopy. Figure 4.10 and the inset show spectra of the as-cast, annealed, and compressed samples. The spectrum due to the Knight shift is dominated by $K = K_s + K_d$ (also described in Chapter 2)[32]. K_s is the direct Fermi contact interaction represented by $K_s = (8\pi/3)|\psi(0)^2|\Omega\chi_s$, where $|\psi(0)^2|$ is the probability density of the wave function of conduction *s*-electrons at the nucleus averaged

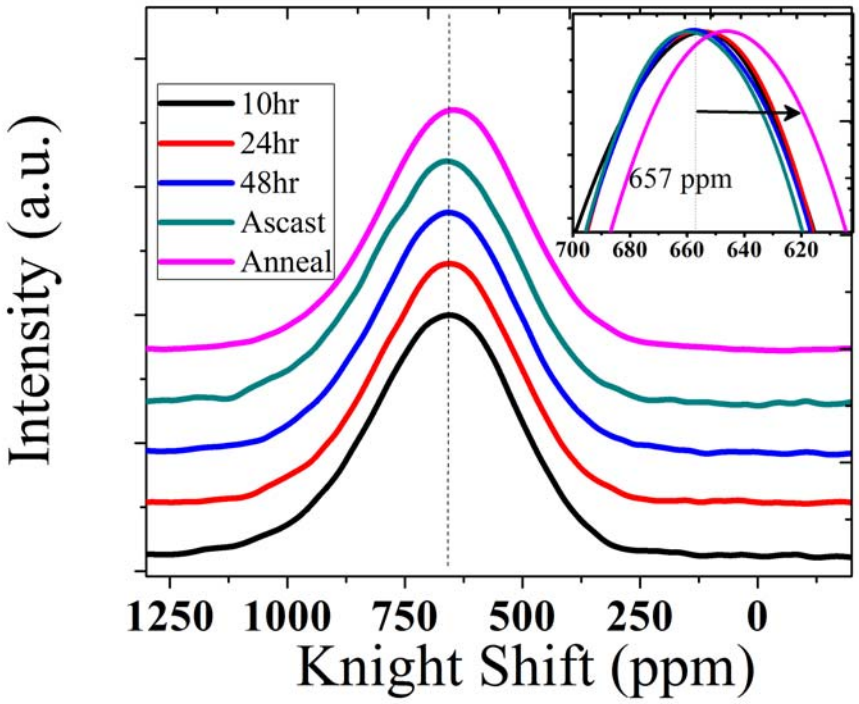

Figure 4.10: Spectra for the as-cast, compressed, and annealed rods are shown. The inset demonstrates the small change in Knight shift caused by structural relaxation: 657 to 647 ppm.

over the Fermi surface and normalized by the atomic volume Ω, and χ_s is the Pauli paramagnetic volume susceptibility. K_d is caused by a polarization shift from the indirect *s-d* exchange interaction that is described by $K_d = \alpha_D \mu_B^2 \chi_D$, where α_D is the hyperfine coupling constant and χ_D is the temperature-dependent Pauli susceptibility due to La and Ni *d*-electrons. The inset to Fig. 4.5 shows that the as-cast sample and compressed samples all have the same Knight shift value of ~657 ppm. Subtle variations of the local electronic structural state caused by atomic volume effects are observed from the annealed rod giving a smaller Knight shift of 647 ppm. The change in Knight shift is predominately due to changes

of the *d*-electron density of states [94, 95] caused by Al 3*s* valence charge transfer to the 5*d*-band of La [96]. The change in shift (~1.5%) is also consistent with the small fluctuations in metallic glass volume or density on the order of ~1.0% to 0.5% [97] that are typically observed during structural relaxation near T_g.

4.4 Discussion: Relevance for atomic-level stress theory

Changes of electronic structure exhibited through annealing and anelastic-induced site symmetry probed by NMR can be reconciled within the theory of atomic-level stresses and site symmetry coefficients [98]. According to this theory, the stress state of an amorphous structure can be considered when a small strain $\vec{r}$ is applied yielding a change in the total internal potential energy by $\Delta E_i = \frac{1}{2}\sum_{\alpha\beta}\sigma_i^{\alpha\beta}\varepsilon^{\alpha\beta}$. $\varepsilon^{\alpha\beta}$ and $\sigma_i^{\alpha\beta}$ are second-rank tensors that define components of applied strain and atomic-level stress, respectively. Two relevant quantities that are derived from the change of energy ΔE_i are the hydrostatic pressure p and the local average shear stress τ. Additional local parameters such as the site symmetry coefficients can be obtained by expressing the change of potential energy as an expansion in spherical harmonics: $\Delta E = \sum_n \varepsilon_n^{l,m}(i)\, Y_l^m(\theta_i,\varphi_i)\frac{|r_i|^n}{n!}$ [79]. The site symmetry coefficients are given by $\alpha_o = \varepsilon_2^{0,0}\ (l=0)$ and $\beta = \sqrt{\left(\sum_{m=-2}^{2}|\varepsilon_2^{2,m}|^2\right)}\alpha_o^{-1}\ (l=2)$, where α_o is a measure of the average harmonic potential energy curvature directly correlated to the atomic volume or hydrostatic pressure p, and β is related to the deviation from spherical symmetry that is associated with the local shear stress, τ.

The change of potential energy ΔE_i due to atomic-level stresses directly parallels the change of quadrupole coupling energy given by $\Delta E_i = \frac{1}{6}\sum_{\alpha\beta} V_i^{\alpha\beta} Q^{\alpha\beta}$ [30] where $Q^{\alpha\beta}$ defines the quadrupole moment tensor and $V_i^{\alpha\beta}$ is the second-rank EFG tensor that is probed by the best fit parameter ω_Q of NMR nutation experiments [35]. Since $Q^{\alpha\beta}$ is an intrinsic property of the NMR probe nucleus $V_i^{\alpha\beta}$ provides a strong correspondence to $\sigma_i^{\alpha\beta}$. Given the physical importance of p and τ, analogies can also be made between site symmetry coefficients and properties measured by NMR. Anelastic-induced structural change in Fig. 4.6 probed by ω_Q is equivalent to the $l = 2$ coefficient and the distribution of local shear stress τ. Similarly, the symmetry coefficient $l = 0$ directly coincides with the changes of local electric structure observed in Fig. 4.10 due to annealing that give rise to a smaller Knight shift (647 ppm). Numerical studies indicate that fluctuations of the local shear stress τ are independent of changes of hydrostatic pressure, p [79] This agrees with the negligible changes of NMR Knight shift and free volume due to anelastic compression. Within the theoretical framework of atomic level stresses, NMR nutation and spectroscopy results provide evidence to suggest that the mechanism of anelastic deformation is one that causes local shear rearrangements of atoms that not only enhance local site symmetry, but to also lower the change in internal potential energy by minimizing the local distribution of atomic-level stress [98]. This suggests that local shearing of atoms is accommodated by approaching a more ideal structural state.

4.5 Conclusions

In conclusion, ^{27}Al NMR and MDSC studies of $La_{50}Ni_{15}Al_{35}$ were utilized to understand anelastic-induced structural changes that were compared with as-cast and annealed reference states. The data reveal that anelastic strain causes an increase in local symmetry near Al atoms that depends on the length and strength of the applied stress. The corresponding changes of free volume were negligible due to the small viscoplastic strain. It was also shown that these anelastic-induced structural changes have a relaxation timescale that is long compared the duration of the constant compression experiments. Furthermore, it was observed that local changes of electronic structure are closely linked to fluctuations of the local density obtained through annealing. The results here show that the anelastic deformation mechanism can be described within the theory of atomic level stresses [98].

CHAPTER 5

Probing the liquid behavior of La-based metallic glass

5.1 Introduction: Structure of Metallic Liquids

After a material undergoes melting, it is widely believed that in the liquid state there exists in single- or multicomponent systems a uniform, long-range disordered structure caused by thermal excitation and motion that gradually changes with temperature. X-ray diffraction patterns have shown that the structure of amorphous materials resembles closely that of liquids [99]. It is well established that in single-component metallic liquids short-range order is preserved up to three or four atomic diameters and that the position of the peak of the pair distribution function varies smoothly with temperature [99, 100]. This might not be expected in the liquid state since structural relaxation times are on the order of 10^{-12} seconds [101]. Short-range order is believed to be a natural consequence of interparticle interactions, which restrict the positions of the atoms in the liquid state. Although the ion-ion pair potential was predicted to be relevant for metallic liquids, because of conduction electrons, a comparison of pair distribution functions for metallic liquids showed that they resembled non-metallic liquids [99, 102]. In that case, a hard-sphere potential pair potential or Lenard-Jones pair potentials have predominately been used to analyze X-ray diffraction [12, 99, 103].

In addition to short-range order, medium-range order is also preserved in multicomponent metallic liquid systems. Icosahedral and icosahedral-like clusters, consisting

of 13 densely-packed atoms, are the predominant short-range structural units in single- and multi-component metallic liquids [100, 103, 104]. It is generally observed that icosahedral ordering changes gradually, becoming more extensive and pronounced with decreasing temperature [103]. It was pointed out by Frank in 1952 that compared to fcc or hcp structural units, icosahedral ordering results in an energy that is ~8.4% lower and thus, might have significant implications for GFA and the ability to undercool a melt below its melting point [4]. Icosahedral order is incompatible with translational symmetry and as a result can significantly inhibit crystal nucleation in supercooled liquids [12]. To some degree short-range ordering is independent of the metallic liquid system observed, which implies that icosahedral ordering of a metallic liquid is compatible with the constituent elements having *s*- or *d*- bonding or an underlying fcc or bcc crystalline structure [100, 103, 104]. For example, icosahedral and distorted icosahedral symmetry is observed in simple metallic liquids such as aluminum [100] and in multi-component systems comprising late and early transition metals [103, 104].

5.2 Phase Transition in liquid state

The study of structural changes and phase transitions in liquids without changes of composition from first-order liquid-liquid phase transitions (LLPT) or polyamorphic transitions has recently become a prominent area of experimental [22, 105, 106] and computational research [22, 107]. In general, little attention was paid to the LLPT since it is believed that the structural changes in liquid should be gradual because of dynamical structural averaging. Upon melting, the entropy of a liquid is expected to increase with a corresponding positive increase in volume. The possibility of an LLPT first arose [108] when melting curves for pure substances analyzed as a function of pressure were found to

exhibit negative slopes of the Clausius-Clapeyron relation $dT_m/dP = \Delta S_m / \Delta V_m < 0$ [22]. This is believed to occur when the density of the liquid becomes larger than the density of the underlying crystalline state.

A LLPT or polyamorphic transition is believed to be driven by differences of entropy or density between the liquid species [22]. This can be compared to crystals that undergo polymorphic phase transitions (e.g. graphite to diamond in the presence of high pressure and temperature) where changes to their entire coordination environment occur to preserve translational symmetry. On the other hand, liquids have more degrees of freedom and below a critical temperature T_c can have coexisting high- and low-density liquid states corresponding to different atomic structures. These coexisting liquid states also have different entropies and are expected to induce changes of the total enthalpy. As a result, most have considered the LLPT phenomenon as a two-state system that can be modeled using a regular solution theory [22, 108, 109]. Recent studies indicate that density alone might not be a sufficient order parameter to describe the cause of the LLPT, and the bond-orientational order parameter *S,* which characterizes locally favored packing structures (medium-range order), might be just as important [110].

5.3 Microscopic Immiscibility in Metallic Liquids

First order phase transitions in the local structure of metallic glasses might also be derived from the thermal history of the metallic melts [25] . In the 1930's, studies of eutectic binary systems Sn-Pb, Sn-Zn, and Bi-Pb have revealed that strong interparticle interactions may actually cause large-scale immiscibility at the atomic level [25, 111]. For example, X-ray scattering curves near the melting point show that they correspond to pure components.

This led to the conclusion that microscopic domains rich with each of the components co-exist in the liquid state, which led to the classification of these binary systems as quasi-eutectic. According to sedimentation experiments in a centrifuge the characteristic scale of these microscopic domains was estimated to be ~1-10 nm [25, 112]. This is significantly larger than the short-range atomic ordering typically seem in X-ray scattering curves [99]. Further experiments on a eutectic Sn-Pb system investigated the origin of this microheterogeneity and studied the thermal expansion coefficient and density when components were mixed ~500 degrees above their eutectic point [25]. The thermal expansion coefficient and density were found to vary smoothly with temperature. However, upon rapidly solidifying and remelting, anomalies were present above the eutectic point, which gave clear indication that microheterogenities are derived from the initial cast metal. These results further helped to formulate the concept of *metastable microheterogeneity*. The concept of metastable microheterogeneity views the enriched medium-range ordered domains as an emulsion or colloid with well-defined interfaces dispersed in a medium of a slightly different composition.

To investigate the relevance of these concepts above for BMGs, an ^{27}Al NMR study of the BMG ternary system $La_{50}Ni_{15}Al_{35}$ was carried out in the liquid state. Heating and cooling experiments reveal significant phase-separation with further liquid decomposition at ~100 degrees above the liquid temperature. In addition, isothermal annealing experiments show that phase-separation can be controlled to some degree. These results provide important insight for understanding mechanisms that drive immiscibility.

5.4 Sample preparation and NMR experiments

For this high temperature study, the $La_{50}Ni_{15}Al_{35}$ BMG system was chosen because of its high GFA (D_c=5mm) [83] and stability against oxidation at room temperature. The BMG rods were cast using pure materials and mixed in a furnace at 2000 C followed by rapid cooling. For each experiment, 2-4 mg BMG pieces were sealed under vacuum in quartz tubes to prevent oxidation (Al_2O_3) that would significantly degrade the signal intensity. The small sample size was chosen to ensure that the sample temperature was homogenous. Energy-dispersive X-ray spectroscopy (EDS) of samples after experiments was carried out and compared to samples that did not undergo heat treatment. This ensured that the composition did not change from significant evaporation or mass loss because of long exposure at high temperatures.

The ^{27}Al NMR experiments were carried out using a homemade high-temperature probe illustrated in Figure 5.1. Inside the water jacket is the heating wire made of tantalum wound in a manner that minimizes the static magnetic field produced by the current. Molybdenum foil is also used to shield the heating wire and thermocouple of the temperature controller from the inductor. To calibrate the probe, an additional thermocouple was sealed inside the probe and centered inside the molybdenum inductor coil and heated to track the temperature between the sample area and the thermocouple near the heating wire. The calibration was further confirmed within +/- 5 degrees by using aluminum to check the melting point at 660 ^{o}C. High-temperature experiments were carried out using reducing gas (99% nitrogen, 5% hydrogen balance) to protect the heating wire.

5.5 High Temperature Differential Scanning Calorimetry

In order to determine the liquidus temperature T_{liq} of $La_{50}Ni_{15}Al_{35}$, high temperature DSC at a heating/cooling rate of 20 degrees/minute was used. Figure 5.2 below notes all the

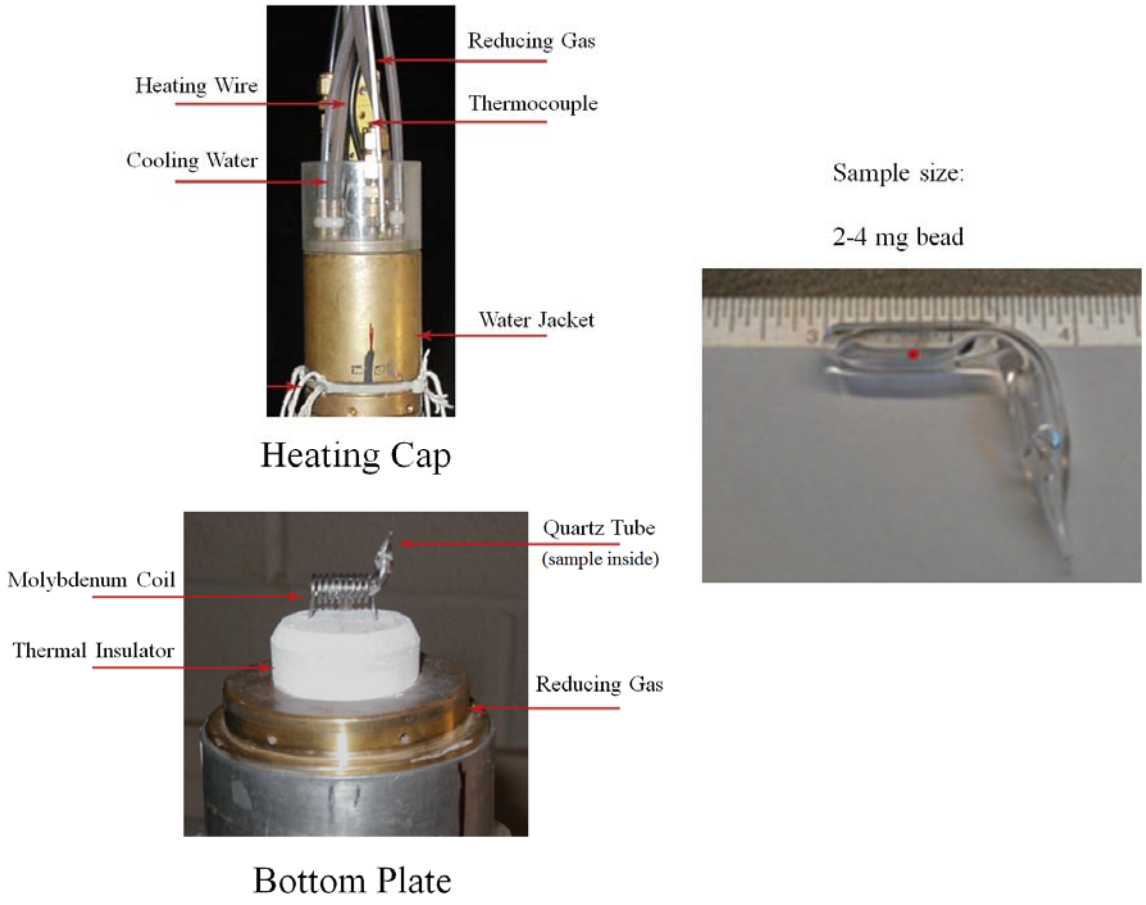

Figure 5.1: High temperature NMR probe that consists of a heating cap and bottom plate. The picture on the right shows the small sample used, highlighted in red [113].

significant thermal transitions encountered during heating and cooling cycles. To show the different cycles clearly an offset of 0.5 W/g was added to the cooling cycle, moving it entirely above the heating cycle. During the initial heating the first important transition is the glass transition T_g at 250 C, followed by first major crystallization exotherm at 320 C and denoted by T_{x1}, then the second smaller crystallization peak at ~380 C corresponding to T_{x2}, and then the liquidus temperature T_{liq} at 690 C. These transitions are in agreement with the

published values [83]. The cooling curve in the boxed region shows how the liquid starts to transforms back to a crystal almost immediately below T_{liq} at ~660 C. In addition, the crystallization process is observed to take place over a large temperature range of ~ 250 degrees. All NMR results discussed in this chapter will involve temperatures above T_{liq}.

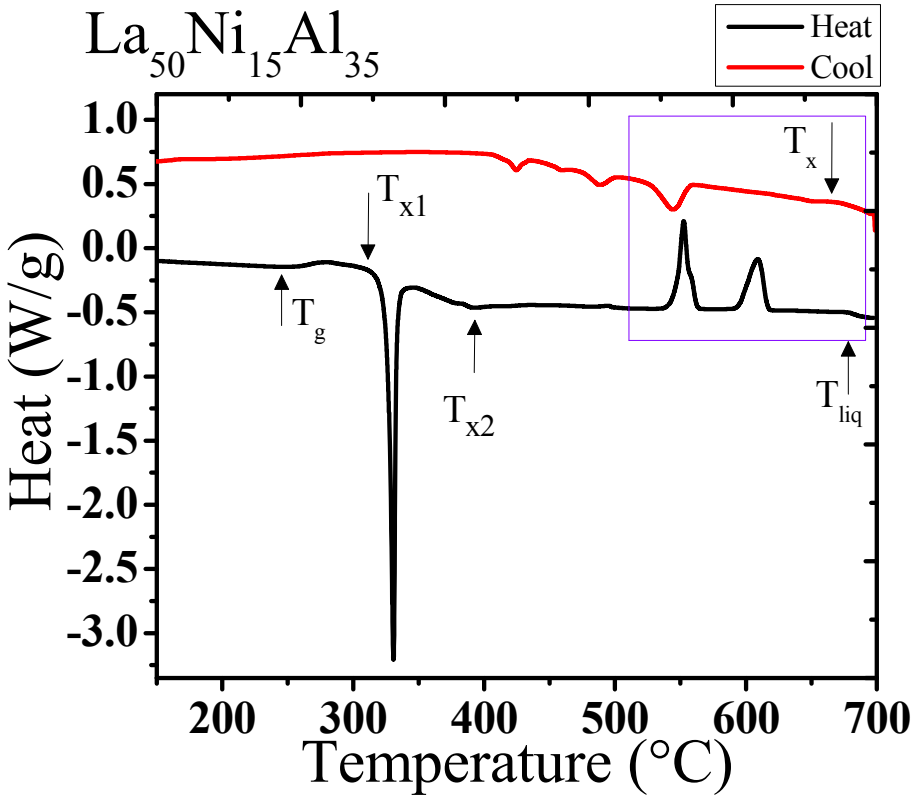

Figure 5.2: High temperature DSC heating and cooling cycles at a rate of 20 degrees/minute.

5.6 Room temperature versus Liquid Spectra

Figure 5.3 shows comparative ^{27}Al NMR spectra obtained for $La_{50}Ni_{15}Al_{35}$ in the glassy state at room temperature and in the liquid state at 960 C corresponding to ~160 degrees above T_{liq}. The main differences between the spectra are the linewidth at full-width-at-half-maximum (FWHM) and the change of the Knight shift as noted by the direction of the arrow. The spectrum at room temperature is considerably broader than that at high

temperature and has a linewidth on the order of ~36 kHz arising from the local distribution of magnetic fields in the glassy state. The peak maximum is the ensemble average of the local fields that represents the average Knight shift of 660 ppm [30, 32]. Upon heating into the liquid state, the Knight shift increases and undergoes linewidth narrowing as expected. In the extreme narrowing regime the rapid relaxation of atoms

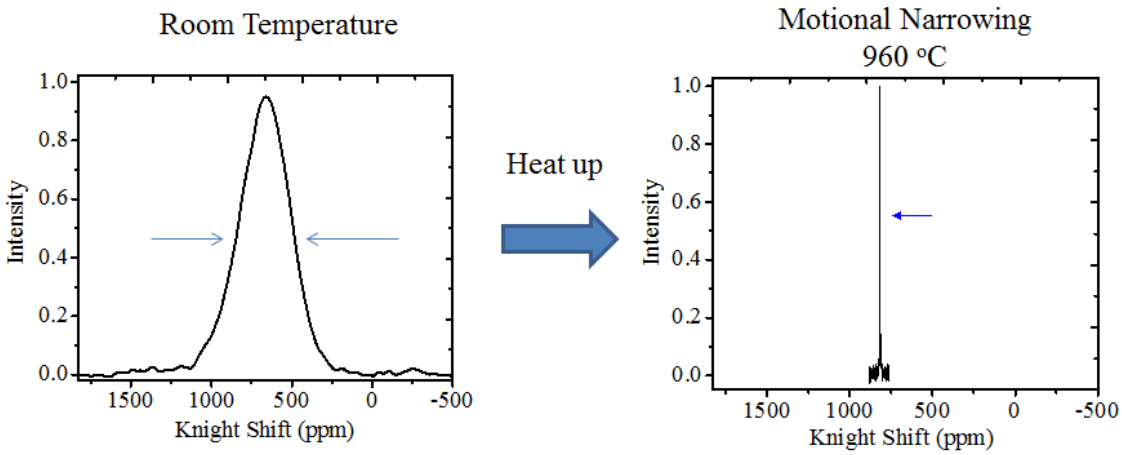

Figure 5.3: Spectra for $La_{50}Ni_{15}Al_{35}$ at room temperature and at 960 C.

on timescales of the order of 10^{-12} s causes fluctuations of the local magnetic field faster than the Larmor frequency and relaxation is defined by a single time $T_1 = T_2$ [30, 114]. The cause for the Knight shift increase will be discussed below. In addition to differences such as linewidth and shift, the liquid line has two peaks as shown in Figure 5.4 by expanding the liquid line spectrum from Fig 5.3. This indicates that in the liquid state of $La_{50}Ni_{15}Al_{35}$ two states coexist and that their peak heights are proportional to their relative populations. They will be referred to as peak 1 and peak 2. The correlation length or mean squared displacement of aluminum in $La_{50}Ni_{15}Al_{35}$ can be estimated from $\langle x(t)^2 \rangle = 6Dt$, where D is diffusion constant and t is the NMR timescale. For a diffusion constant of 10^{-5} cm^2 s^{-1} [115]

and NMR timescale of ~1 ms, the correlation length is ~ 25,000 Angstroms. The correlation length implies that these two coexisting states comprise large extended structures in the liquid. Further insight regarding the nature of these liquid structures and their temperature dependence will be drawn from discussion below.

5.7 Temperature Dependent Knight Shift

The temperature dependence of the Knight shift was obtained by first heating the samples to 700 C (just above T_{liq}). Data were collected in 10- or 20-degree increments until 960 C and then repeated upon cooling. Heating and cooling was implemented to see if the

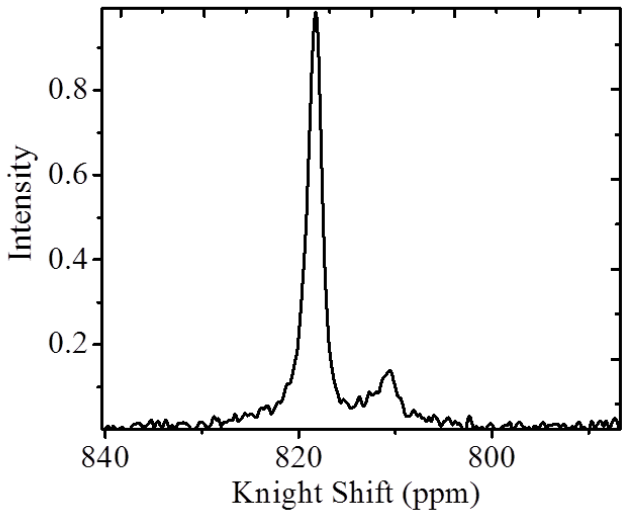

Figure 5.4 Liquid spectrum showing two peaks at 818 ppm (peak 1) and 811 ppm (peak 2).

temperature dependence were reversible. The temperature dependence of the Knight shift is shown in Figure 5.5 for both liquid peaks. Peak 1 corresponds to the peak with the larger intensity (and larger Knight shift) and peak 2 is the much-smaller peak. Figure 5.6 shows the corresponding spectra in the liquid state upon heating at 720, 780, 820, 880, and 920 C that are noted by arrows in Fig. 5.5. A quick comparison of spectra at 720 C versus 950 C shows

pronounced narrowing with increasing temperature. These spectra show that two coexisting liquid states of different intensity (or population) are present at all the temperatures sampled by NMR. Inspection of Fig 5.6 shows that the relative proportion of these two liquid states remains approximately constant. The reasons for phase separation will be further speculated upon below.

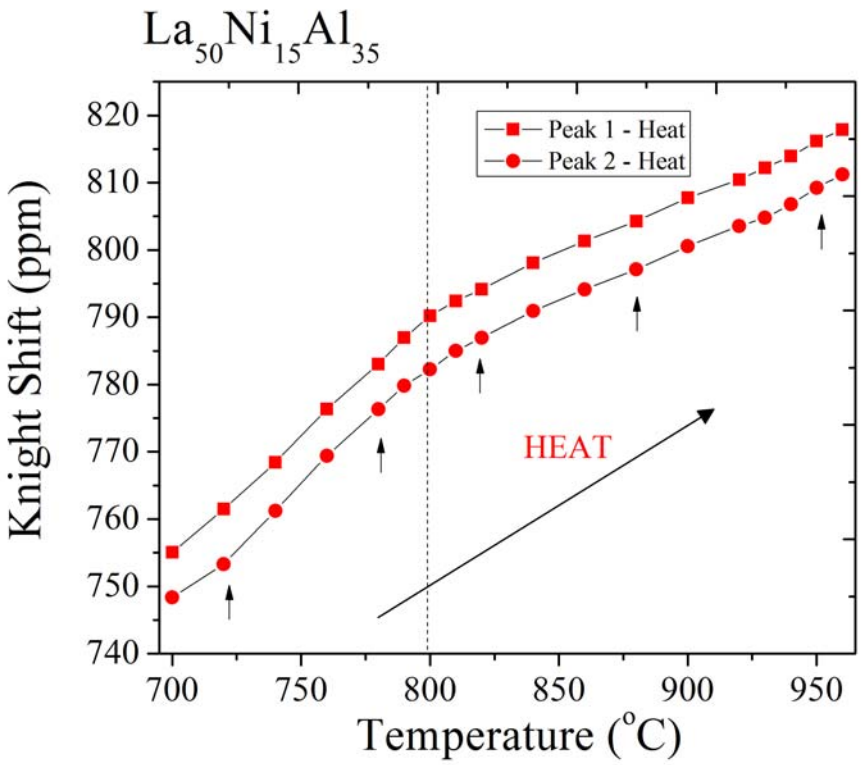

Figure 5.5 The temperature dependence of the Knight shift during a heating cycle. Peak 1 (■) and peak 2 (●) refer to the large and small peaks, respectively in Fig. 5.4 The arrows are a guide for the eye to show which temperatures correspond to the spectra in Fig. 5.6.

In addition to phase separation, Fig. 5.5 shows that the Knight shift displays a kink or non-linear behavior at 800 C (>100 degrees above T_{liq}). The slope above the kink is 0.17 ppm/K and the slope below the kink is 0.36 ppm/K. Measurements of the temperature dependence of the Knight shift during cooling were also implemented to see if phase

separation and non-linear behavior were maintained. Figure 5.7 shows the temperature dependence of the Knight shift during cooling at all the same temperatures accessed during the heating cycle. It is observed that non-linear behavior is still present during cooling, but there is also a hysteresis shown by a difference in slopes between heating and cooling. This is verified by noting that the slope above the kink at 810 C during cooling is 0.2 ppm/K and the slope below the kink

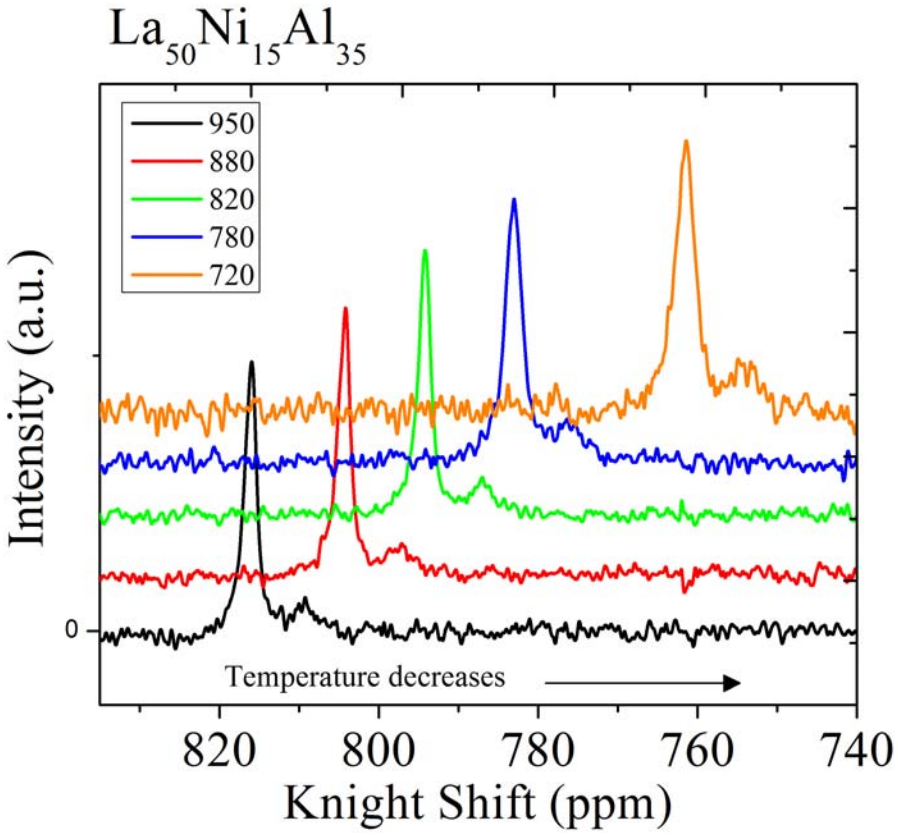

Figure 5.6 Spectra for the heating cycle at 720, 780, 820, 880, and 920 C. The relative intensities between the two phases stay constant.

is ~0.3 ppm/K. Table 5.1 briefly summarizes these slopes for quick reference to show the differences. In addition to the hysteretic behavior, the intensity of the second peak gets larger

just below the kink of the shift. Figure 5.8 displays this change upon cooling below 810 C. This corresponds to the enhancement of the second smaller liquid phase shown in Fig 5.4. Figure 5.9 plots the corresponding ratios of intensities as a function of temperature during heating and cooling to demonstrate the relative proportion of the two liquid states. Interestingly, the ratio of intensities is ~7 at higher temperatures and is constant until the

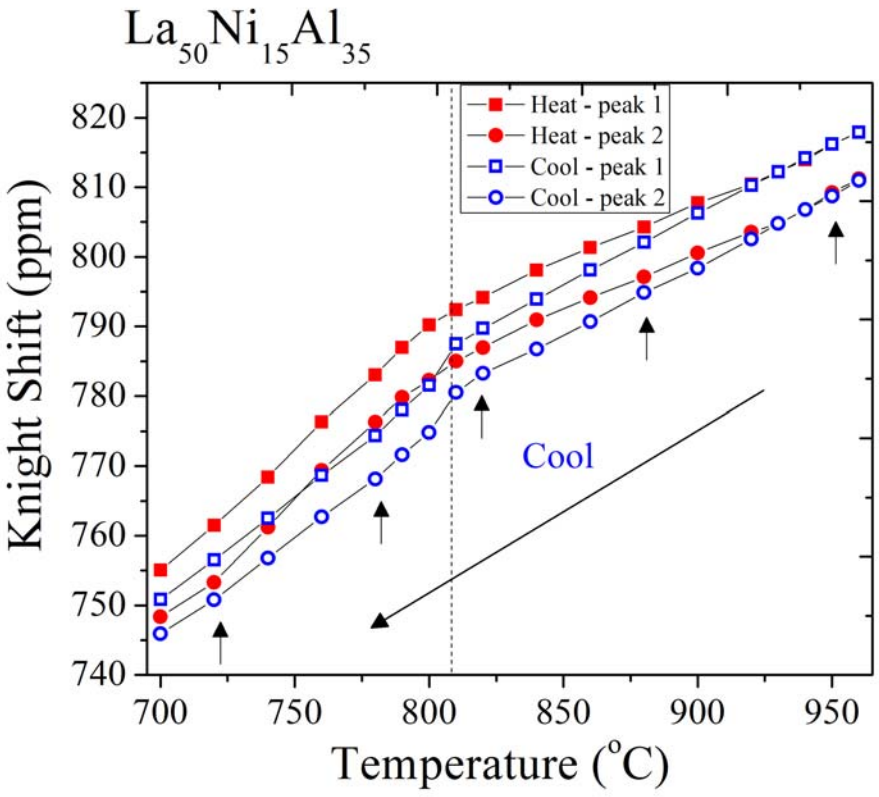

Figure 5.7 The temperature dependence of the Knight shift during a heating and cooling cycle. Peak 1 (□) and Peak 2 (O) refers to the large and small peak as shown in Fig. 5.4 Arrows guide the eye to show which temperatures correspond to the spectra in Fig. 5.8.

Table 5.1: Summary of Knight shift slopes for the two liquid peaks during heating and cooling.

$La_{50}Ni_{15}Al_{35}$	Peak 1 (ppm/K)	Peak 2 (ppm/K)
Below Kink (Heat)	0.36	0.36
Above Kink (Heat)	0.17	0.17
Below Kink (Cool)	0.31	0.29
Above Kink (Cool)	0.20	0.20

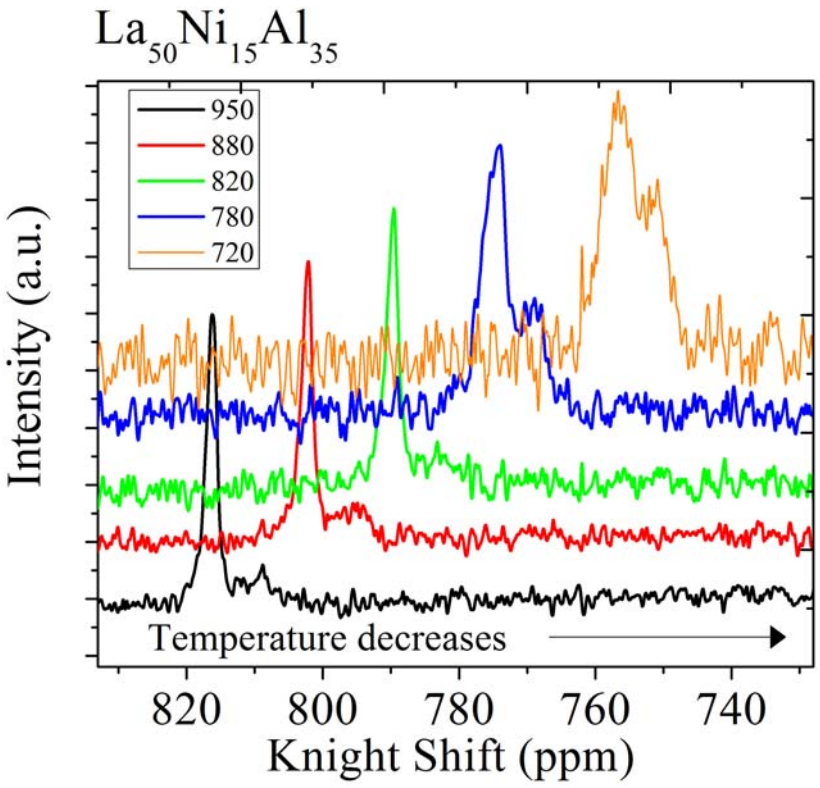

Figure 5.8 Spectra for the cooling cycle at 720, 780, 820, 880, and 920 C. The relative intensities between the two phases stay constant until just below the kink temperature at 810C.

temperature of the kink is reached upon cooling and then changes to ~2 and remains constant. This means that compared to the heating cycle, the liquid state upon cooling has become more heterogeneous and complex.

5.8 Population and Knight Shift Dependence on Rapid Cooling

Based on the data presented, it is not clear why peak 2 is enhanced below the kink. It is important to note that the data collected in Figs. 5.5 – 5.9 occurred over the span of several hours. Therefore, it might be of interest to understand whether the behavior observed in this

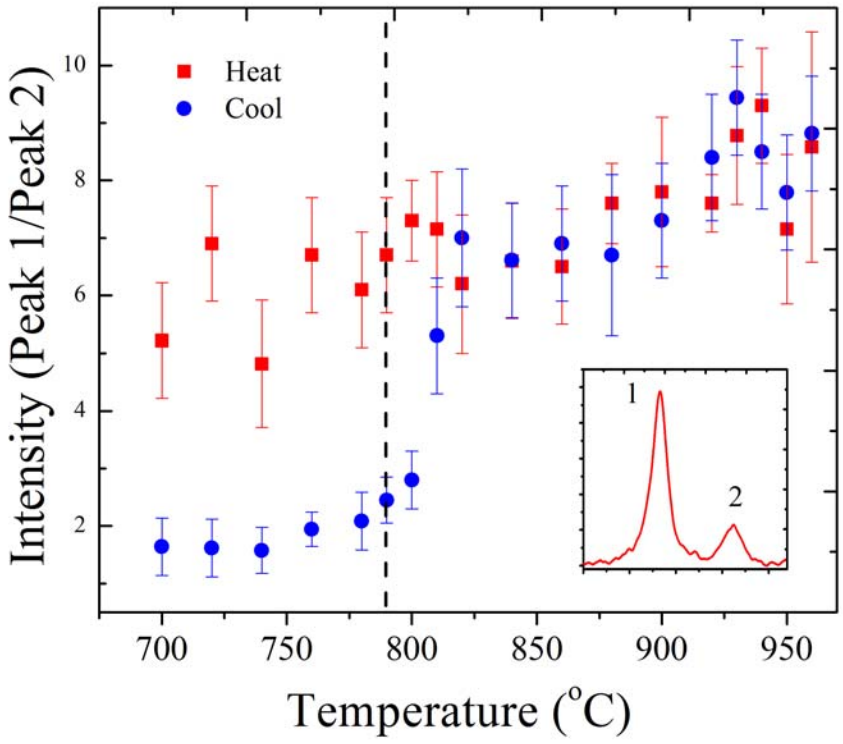

Figure 5.9 Ratio of intensities for the two liquid peaks as a function of temperature. Within the error bars the ratio stays constant at ~7 upon heating. The sharp change in intensity from ~7 to ~2 denotes the significant growth of the smaller liquid phase. The onset temperature is consistent with the temperatures of the kinks exhibited in the Knight shift during heating and cooling.

system has any dependence on the time spent at any one particular temperature, which will be defined as the isothermal annealing time. To test this, $La_{50}Ni_{15}Al_{35}$ was heated to 960C for initial data collection and then cooled to 860, 790, and 720 C for additional data collection. The total experimental time was ~45 minutes. These temperatures were chosen since they capture important transitions observed for this system. The spectra are summarized in Figure 5.10 and show that below the kink the growth of peak 2 is actually

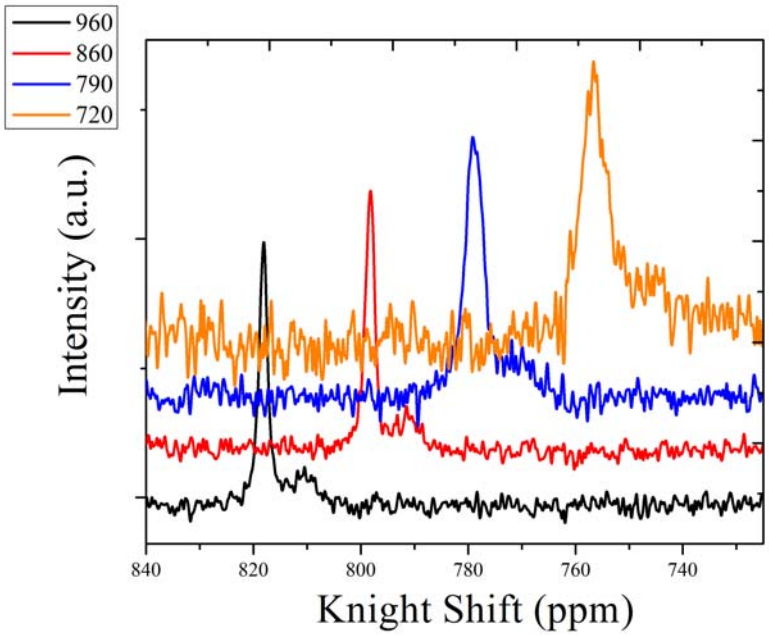

Figure 5.10 Spectra obtained by heating to 960 C and then rapidly cooling to 860, 790, and 720 C. The smaller liquid phase is suppressed.

suppressed with shorter length of the isothermal annealing time. This strongly indicates that this liquid system is not at equilibrium, which is quite surprising since the typical relaxation time of liquid at this temperature is ~ 10^{-12} s [101]. This also is verified in Figure 5.11 that compares the corresponding ratios of intensities to those obtained by long-time heating and cooling cycles. The corresponding Knight shifts are plotted in Figure 5.12 and compared to

the shifts obtained by heating and cooling, showing no significant difference within the error bars. These results indicate that time is an important parameter for controlling the relative population of the two phases in this system.

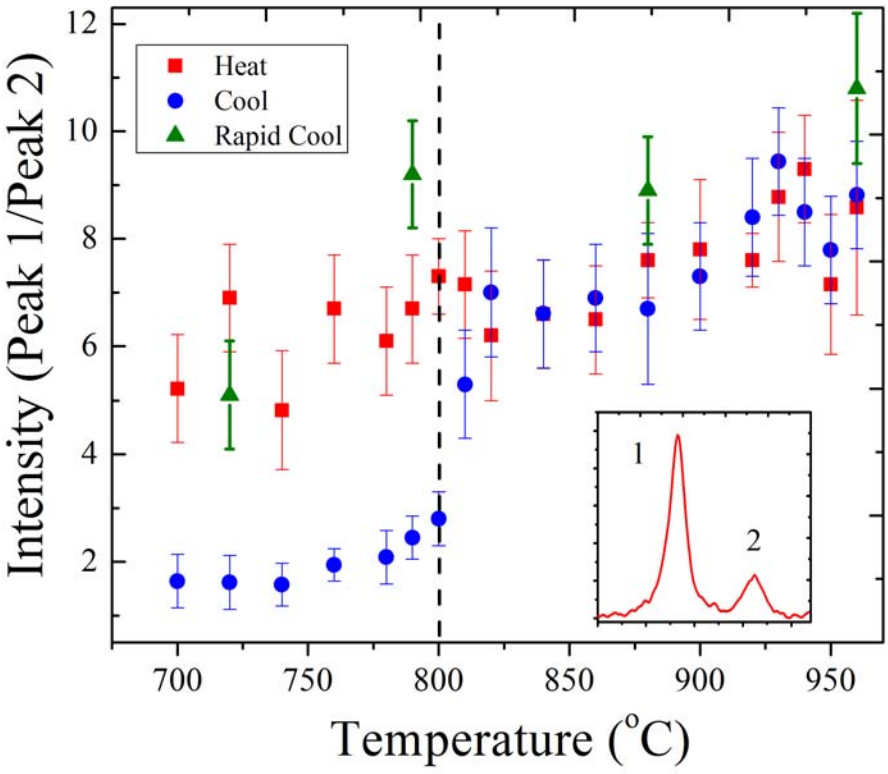

Figure 5.11 Ratio of intensities for the two liquid phases obtained by heating to 960 C and then rapidly cooling to 860, 790, and 720 C. The smaller liquid phase is suppressed as observed by the constant intensity ratio of ~7.

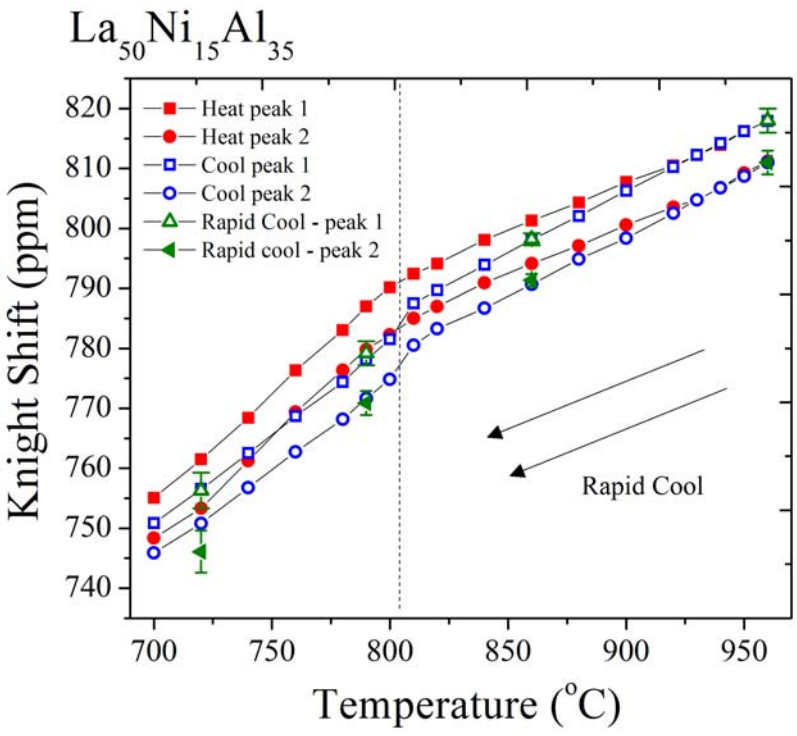

Figure 5.12 The temperature dependence of the Knight shift during rapid cooling cycle as noted by the arrows. Peak 1 (▲) and Peak 2 (Δ) refer to the large and small peak as shown in Fig. 5.4.

5.9 Stability of the Liquid State Due to Isothermal Annealing Time

Based on the data presented it is important to understand the relative stability of the liquid state in different temperature regions surrounding the first-order phase transition: at the highest temperature (960 C), intermediate temperature above the kink, and below the kink. Stability here will be defined as the lack of change the spectrum undergoes as a function of isothermal annealing time (i.e. sitting at one temperature). Figure 5.13 shows spectra above the kink at 960 C and 860 C for different annealing times: 8 min., 48 min., and 1.3 hours, which show no change. These results indicate that the liquid phase above the kink is stable within the annealing times tested. To test the stability below the kink different isothermal

annealing times at 960 C were used and then the samples were cooled to 790 C for data collection. These results are summarized in Figure 5.14 and show that for isothermal annealing times greater than 1.3 hours peak 2 is enhanced.

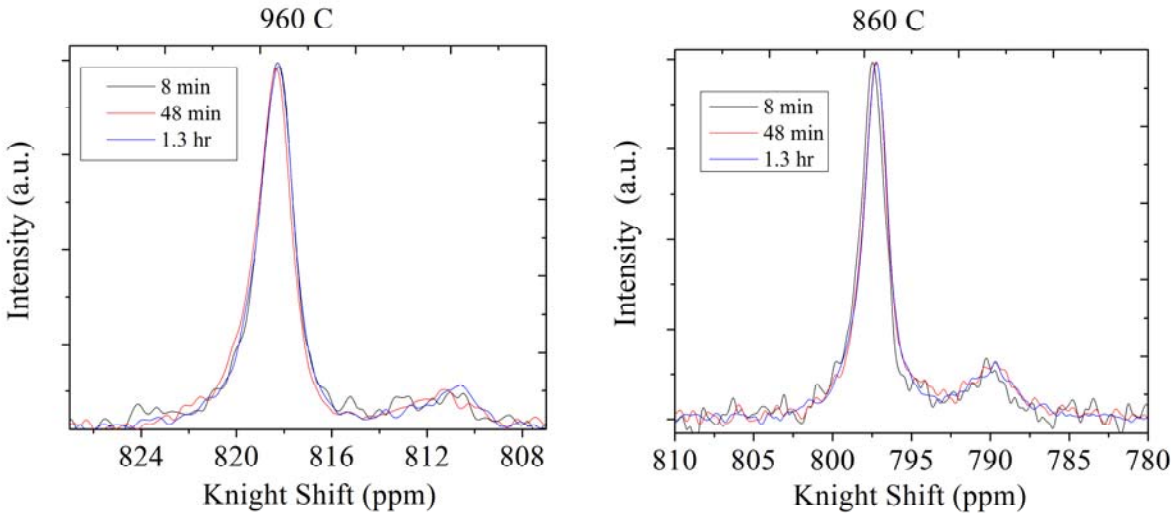

Figure 5.13 Spectra at 960 C and 860 C for 8 min, 48 min, and 1.3 hour annealing times. The spectra show stability in these temperature regions.

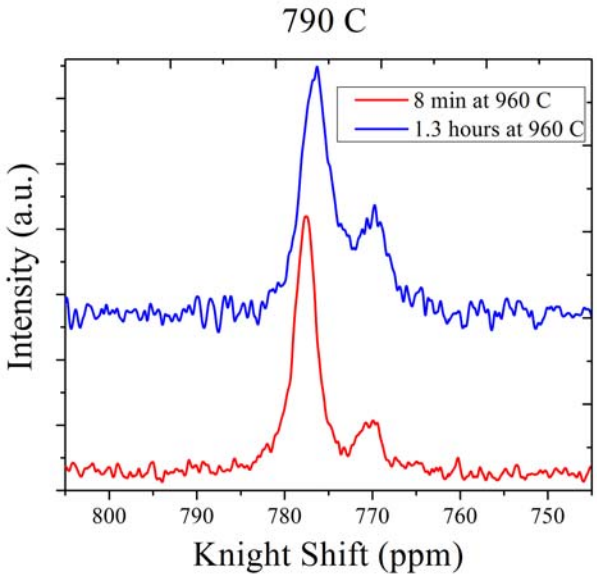

Figure 5.14 Spectra at 790 C due to isothermal annealing times 8 min and 1.3 hours at 960 C. Peak 2 is enhanced for an isothermal annealing time > 1 hour.

5.10 Thermodynamics of the Knight Shift

The kink behavior observed in the temperature dependence of the Knight shift and ratio of intensities gives clear indication the mechanism involved is in fact a first-order phase transition (i.e. non-reversible) of a liquid phase-separated system. This is further evidenced by the hysteretic behavior, which implies that this is a metastable thermodynamic process that undergoes energy dissipation near 800C [26, 116]. The fact that the onset temperature of the kink coincides with the enhancement of peak 2 shows that the phase-separation behavior is not independent of the first-order phase transition.

In order to understand the mechanism for the observed liquid-liquid phase transition the Knight shift needs to be considered in more depth. In general, the Knight shift reflects the local electronic structure in the vicinity of the Al atoms. While there is no large-scale atomic motion at room temperature, there is still fast atomic vibration on the order of 10^{12} s^{-1}. The Knight shift was defined previously as

$$K = (8\pi/3)\left\langle|\psi(0)|^2\right\rangle_{E_F} \Omega\chi_{\text{Pauli}} + \alpha_D\mu_B^2\chi_D \ , \qquad (5.1)$$

where the first and second terms on the right-hand side correspond to the shift contributions from *s*- and *d*- conduction electrons, respectively. In the liquid state, metallic bonds are loosened and volume expansion is usually important [117]. The dynamic features of liquids include fast atomic vibration and slower cooperative shear processes that reflect the fact that the local distribution of atoms in the vicinity of the Al atoms is constantly changing [13, 118, 119]. Considering this, it is more advantageous to express the Knight shift in terms of thermodynamic quantities that will provide insight to the first-order phase transition observed. In the liquid state the Knight shift can be expressed generally as

$$K \approx S_{vib}(\mathrm{T}) + S_{conf}(T)\,, \tag{5.2}$$

where $S_{vib}(T)$ represents the mean-squared displacements $\left\langle u(t)^2 \right\rangle$ of local atomic motion or harmonic vibration of equipartition theory in the thermodynamic limit [13] and $S_{conf}(T)$ [120-122] is the local configurational entropy. Then, $S_{conf}(T)$ can be further expressed as $S_{conf} \approx k \ln \left\langle N_{conf} \right\rangle$, where $\left\langle N_{conf} \right\rangle$ comes from the pseudopotential expansion of $\left\langle |\psi(0)|^2 \right\rangle_{E_F} \Omega$ in (5.1) to account for scattering of electrons in a metallic liquid. $\left\langle N_{conf} \right\rangle$ is directly related to the structure factor ***S(Q)*** [121, 122], which describes the interference of light and neutron scattering in liquid. The interference depends on the relative position of the particles or the ensemble average of different particle configurations $\left\langle N_{conf} \right\rangle$.

5.11 Data Interpretation

For the complex liquid behavior observed here data interpretation will cover two different perspectives: 1) chemical potential driven atomic-level immiscibility and 2) potential energy landscape influenced thermodynamic behavior.

5.11.1 Atomic-level immiscibility

For a homogenous or miscible liquid (no phase-separation), it is anticipated that (5.2) should give rise to monotonic or linear behavior [99, 113, 117, 122]. In order to account for the non-linear behavior of the phase-separated liquid shown in Figs. 5.5-5.10 another parameter in (5.2) must be invoked to account for the change in slope of the Knight shift. The increase of the Knight shift slope below the onset temperature of the kink might reflect a strong enhancement of short- or medium-range order in the liquid structure [123]. Considering this, the Knight shift can be expressed as

$$K \approx S_{vib}(T) + S_{conf}(T) - \sigma \exp[\Delta G / kT]_{loss}, \quad (5.3)$$

where $-\sigma \exp[\Delta G / kT]_{loss}$ describes the configurational entropy loss of the liquid caused by an increase in short-range order and a corresponding decrease of the system's free energy ΔG and σ is a fitting parameter. Therefore, the increase of the Knight shift slope below the kink might reflect a more rapid loss of configurational entropy. This is not unreasonable considering that the local ordering of a metallic liquid generally becomes more well-defined upon cooling [99, 103].

5.11.1.2 Features of Phase Separation

The cause for the more rapid loss of configurational entropy can be understood by considering the important role of phase separation in the liquid state of $La_{50}Ni_{15}Al_{35}$. It is observed that phase separation not only exists at all the temperatures sampled, but is enhanced below the onset temperature giving rise to a more heterogeneous liquid upon cooling. The two coexisting liquid states result from of phase separation due to different heats of mixing of the constituent elements in $La_{50}Ni_{15}Al_{35}$ as shown in Table 5.2 [124]. The differences in atomic radii between La, Ni, and Al coupled with different interatomic interactions, owing to heats of mixing, might give rise to liquid structures that promote immiscibility [26].

Since the driving force for phase separation is non-existent or small, it is reasonable to expect that the composition difference between the two peaks would also be small. This is verified by observing the small difference in Knight shift of ~7 ppm between the two peaks. The composition can reasonably be assumed to differ by as much as 5 percent given that the

shift difference between $La_{50}Ni_{15}Al_{35}$ and $La_{45}Ni_{15}Al_{40}$ at room temperature is ~11 ppm [83]. According to Table 5.2 the strongest interaction is between La and Al and then between La

Table 5.2: Enthalpic heats of mixing binary systems between La, Ni, and Al elements [124]

ΔH^{mix} (kJ/mole)	La	Al	Ni
La	0	-38	-27
Al		0	-22
Ni			0

and Ni. The corresponding crystalline structures of $La_{50}Ni_{15}Al_{35}$ might provide some insight for understanding the nature of the two coexisting liquid states. In a similar composition, X-ray studies of annealing in $La_{55}Ni_{25}Al_{25}$ have found that after the first major exothermic peak (similar to T_{x1} in Fig 5.2) the crystallized structure is made up of predominately cubic La_3Al and orthorhombic LaNi crystal phases [125, 126]. Upon further heating to the second smaller exotherm (similar to T_{x2} Fig. 5.2), a ternary phase La(Al,Ni) that has orthorhombic-like features is believed to be the final crystal structure following complete crystallization after T_{x2}. If it is assumed that these structures persist to some degree in the liquid state [22] then perhaps the larger liquid peak with the larger shift in Fig. 5.4 might represent a LaNi orthohombic structure. The smaller peak would then correspond to the orthorhombic La(Al,Ni) phase. Given the lattice parameters [125] the atomic packing factor for peak 1 of the liquid spectrum is larger (0.13) than that of peak 2 (0.10) and might signify a slightly more densely-packed liquid structure with a lower energy.

5.11.1.3 Liquid Decomposition: Ostwald ripening and Brownian Flocculation

Phase separation is a wide-spread phenomena in many binary metallic systems such as Cu-Pb, Al-Pb, Hg-Ga, and Al-Bi that have a miscibility gap [26]. Immiscibility of metallic melts is illustrated in Figure 5.15, which shows a simple binary phase diagram in a system of atoms or molecules A and B. Above the critical temperature T_c, A and B are completely miscible and give rise to a homogenous liquid L. Just below T_c the homogenous liquid can undergo decomposition into two coexisting liquids $L_1 + L_2$ that vary in composition between x_1 and x_3. An alternative route for liquid decomposition is along the A-rich side where there is the possibility of a monotectic reaction $S_A + L_1$ resulting a liquid/solid phase. Cooling below T_1 further results in other monotectic reactions $S_A + L_2$, $S_B + L_2$, and other solidus phases.

In addition to the phase-separation of liquid $L_1 + L_2$ below T_c, there is another other decomposition process that becomes important. For example, the kink of the temperature dependent Knight shift observed in $La_{50}Ni_{15}Al_{35}$ signifies additional processes that occur during cooling. In the instance that interfacial energy is important there is the possibility of Ostwald ripening in metallic phase-separated liquid systems [26, 127-129]. Ostwald ripening is a spontaneous thermodynamic transition in phase-separated liquids that is driven by the reduction of the total interfacial energy. In such a process larger phase-separated regions or droplets will form at the expense of smaller ones to decrease the overall surface-area-to volume-ratio. This is further facilitated by the dispersive transfer of smaller droplets onto larger ones. Ultimately, this reduces the free energy associated with the interfacial energy of

the dispersed phase-separated droplets. The growth of the mean droplet phase [26] is given by

$$\overline{R}^3 - \overline{R}_o^3 = \frac{8}{9}\frac{D\sigma\Omega c_\infty}{k_B T(c_\beta - c_\infty)}t \qquad (5.4)$$

where R is the droplet radius, R_o is the initial droplet radius, D is the diffusion coefficient, σ is the interfacial tension, Ω is the atomic volume, c_β is the composition of the

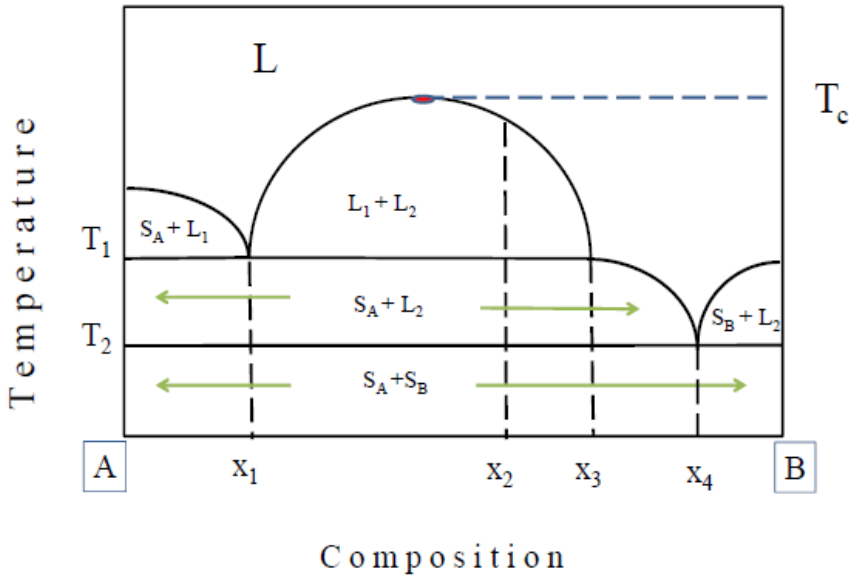

Figure 5.15 Binary phase diagram of A and B atoms that have a miscibility gap. Cooling liquid L below T_c results in liquid decomposition such as phase-separation $L_1 + L_2$, monotectic $L + S$, and solidus reactions $S_A + S_B$.

droplet, c_∞ is the composition in the matrix surrounding the droplet, and t is the time for Ostwald ripening. Ostwald ripening is a promising mechanism for the hysteretic behavior observed in $La_{50}Ni_{15}Al_{35}$ at ~800C that signifies energy dissipation. This is supported by the increased slope below the kink, which would correspond to the more rapid loss of

configurational entropy caused by the growth of larger dispersed phase-separated droplets. It is also important to note that Ostwald ripening is independent of the cooling rate (rapid or slow).

Slow Brownian flocculation [130] is another mechanism that might help explain the growth of peak 2 in $La_{50}Ni_{15}Al_{35}$ during Ostwald ripening. If interatomic forces are important, Brownian motions of the phase-separated droplets result in the formation of loose packs of atoms over time. These loose packs retain their phase-separated identity, but are expected to lose some kinetic independence. The heats of mixing given in Table 5.2 reflect competing interatomic forces [26]. The flux arising from slow Brownian flocculation of particles whose centers pass through every sphere of radius r surrounding the central particle is given by [130]

$$J_{slow} = 4\pi r^2 \left(2D \frac{dn_j}{dr} + \frac{n_j}{B} \frac{dV_T}{dr} \right) \tag{5.5}$$

where D is the diffusion coefficient, n_j is the particle concentration, B is a friction factor, and V_T is the interatomic potential. The first term on the left-hand-side is Fick's first law of diffusion. The second term accounts for competing forces between particles that help facilitate flocculation of particles.

Based on the results of isothermal annealing time, slow flocculation might play an important role for phase-separation in $La_{50}Ni_{15}Al_{35}$ liquids. Isothermal annealing for long periods of time at higher temperatures might enhance the growth of peak 2 since the diffusion coefficient is larger (~one order of magnitude between 960 and 790 C), thereby increasing the flux J_{slow} and the probability of flocculation in a shorter period of time. Here it

is observed that flocculation does not interfere with the relative population of peak 1 and peak 2 above the kink. Instead, flocculation assists in enhancing peak 2 during Ostwald ripening below the kink.

5.11.2 Potential Energy Landscape Influenced Regime

Interpretation of liquid behavior within the potential energy landscape has provided tremendous insight into the nature of the dynamics preceding the glass transition [2, 27]. For example, at high temperatures ($T>>T_g$) the structural relaxation of a liquid has an exponential dependence. Upon cooling near T_g, the structural relaxation of the glass-forming liquids increases significantly and is dominated by non-exponential relaxation processes. In addition to drastic changes in the relaxation, other interesting liquid behaviors include a breakdown of the Stokes-Einstein relation and a decoupling between rotational and translational diffusion [101, 131, 132]. The dynamics of liquids was recently considered within the framework of the potential energy landscape to provide insight for the crossover or onset temperature that demarcates exponential versus non-exponential relaxation processes [133]. Here the non-equilibrium liquid behavior of $La_{50}Ni_{15}Al_{35}$ will be considered in the potential -energy-landscape-influenced regime and will be described in more depth below.

Qualitatively, the potential energy landscape can be described as the configurational -space dependence of the complex potential energy interactions in a 3N- (N = number of particles) dimensional hypersurface. The relevant features of a potential energy landscape can be understood by examining a slice of the hypersurface. A schematic illustration of the potential energy versus particle coordinates is given in Figure 5.16 and summarizes the important features of the energy landscape. General features of the landscape in Fig. 5.16 are given by the number and distribution of potential energy minima, which characterize

different configurations that can be accessed by a liquid [133]. The time evolution of a liquid can be viewed as the motion of a particle on the potential energy surface, with successive transitions between one basin and another. Small intrabasin displacements correspond to the harmonic motions of the liquid. It is important to note that temperature governs the way that a liquid samples its potential energy landscape and that the energy landscape does not evolve with temperature. Therefore, upon cooling deeper and rarer potential minima, such as crystalline states (see Fig. 5.16), can be accessed and explored. A large collection of inherent structures that characterize the properties of the liquid is called a megabasin.

The relaxation of a liquid was recently considered in the framework of its potential energy landscape by examining the temperature dependence of the average potential energy [133-135] using molecular dynamics simulations. In the high-temperature or free-diffusion regime (region (1) in Fig. 5.16), the liquid has sufficient thermal energy to surmount most or all of the potential energy barriers. The temperature dependence of the potential energy in this regime is weak reflecting the minimal influence of the interatomic interactions. Upon cooling, the thermal energy of the liquid becomes comparable to the configurational potential energy and the liquid begins to sample different configurations by moving between basins. This corresponds to the transition into the potential energy landscape-influence regime (region (2) in Fig. 5.16) where there is a strong temperature dependence of the potential energy. This is also referred to as transitioning from liquid-like to solid-like behavior [136].

Within the context of the potential energy landscape the liquid behavior in $La_{50}Ni_{15}Al_{35}$ can be understood by identifying features of the landscape the measured NMR parameters can characterize. Each minimum in the potential energy landscape refers to the

average inherent energy $\langle E^I(T) \rangle$ for a corresponding liquid configuration sampled at a particular temperature. For a given temperature, the different configurations available to a liquid can be expressed as expressed as the configurational entropy by $S_{conf}(E^I) \equiv k_B \ln[\Omega(E^I)\delta E^I]$ where $\Omega(E^I)\delta E^I$ is

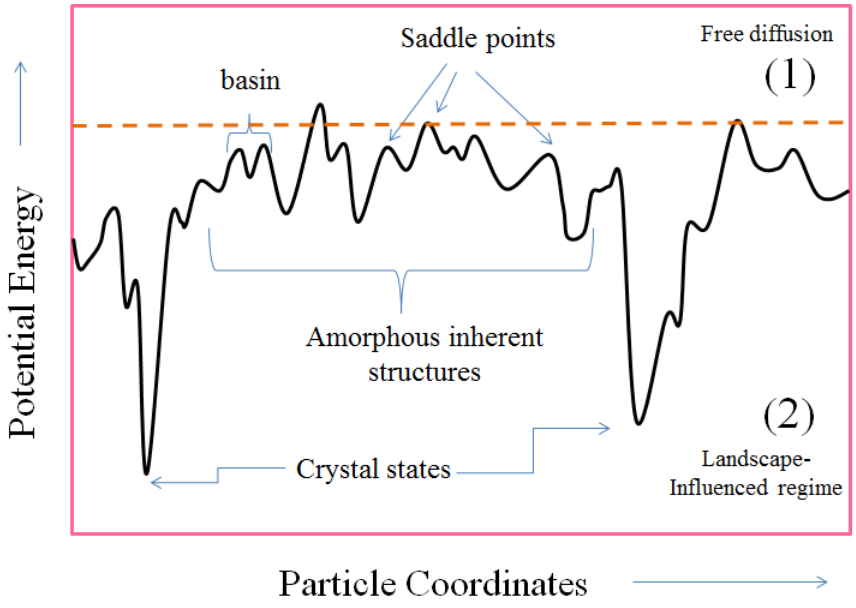

Figure 5.16 Schematic illustration of the potential energy landscape of a liquid as a function of the N particle coordinates adapted from [137]. The potential energy is characterized by the number and distribution of potential energy minima that correspond to the liquid configuration. The dashed line (- - - -) represents the crossover temperature from free diffusion (1) to the landscape-influenced regime (2) [133].

the multiplicity of inherent structures probed at a particular temperature between E^I and $E^I + \delta E^I$ [135]. Therefore, the Knight shift measured at high temperatures provides a measure of the change of the configurational entropy arising from temperature dependent changes. The slope of the Knight shift can be related to the configurational heat capacity [120] by

$$\left(\frac{\partial \ln(K)}{\partial T}\right)_p \approx T\left(\frac{\partial S_{conf}}{\partial T}\right)_p = C_{p,conf} \ . \qquad (5.6)$$

The configurational heat capacity provides information regarding the "ruggedness" of the landscape or the number of different liquid configurations sampled by a liquid. For example, fragile glass-forming liquids (such as toluene and o-terphenyl) have a larger configurational heat capacity at the glass transition than do strong glass-formers (SiO_2 and GeO_2) [138].

Based on the correspondence made between features of the potential energy landscape and the Knight shift parameter measured by NMR, the change of slope observed near 800 C upon heating can reasonably be attributed to the liquid crossing from the energy-landscape-influenced (region (2) in Fig. 5.16) to the free diffusion regime (region (1) in Fig. 5.16) and vice-versa upon cooling. This is further supported by the larger slope or configurational heat capacity in the landscape-influenced regime, which is proportional to the number of configurational minima that can be accessed by the liquid. The temperature dependence of the Knight shift in the free-diffusion regime is also significant and can be attributed to atomic vibrations. The hysteresis observed in the Knight shift between heating and cooling indicates that enthalpy is first absorbed (endothermic) when heated through the crossover temperature and then released (exothermic) upon cooling.

It was noted in Section 5.11.1.2 that two coexisting liquid states of slightly differing composition may explain the shift difference of ~ 8ppm. At high temperature, the Knight shift is also sensitive to volume expansion, which would affect the mean-squared displacements of atoms within a cage surrounding aluminum. In other words, the two coexisting liquid states might have the same composition, but have slightly different densities or structures. The similar configurational heat capacities or slopes of the Knight shift (Table

5.1) obtained for both peaks upon heating and cooling strongly suggest that these two liquid states are quite similar.

Two coexisting liquid states or polyamorphism (same composition with differing density) can be accounted for in the potential energy landscape context with two megabasins [138, 139]. Since these two liquid states are believed to be similar, the ruggedness or configurational heat capacity of the two megabasins will be expected to be quite similar. Figure 5.17 gives a schematic illustration of two megabasins separated by a small energy barrier. The dashed horizontal line represents the crossover from free diffusion to the landscape-influenced regime. Peak 1 in Fig. 5.4 represents the megabasin that is at a lower potential energy to account for the larger liquid phase-separated population. Upon fast cooling or short annealing time at high temperature (see Fig. 5.14), the ratio between peak 1 and peak 2 is ~7, which reflects the fact that inherent structures in megabasin 1 on average comprise liquid configurations that are more energetically favorable (lower potential energy). Simulation studies of the scattering angle [136] sample the waiting time in a megabasin indicate that short waiting times result in small scattering angles and actually prevent sufficient equilibration. This is surprising considering the fast diffusion and structural relaxation times of typical glass-forming liquids at high temperatures. Long waiting times (or annealing times) result in large scattering angles that reflect multiple entries and exits of the liquid in its megabasin [136]. The results presented in Fig. 5.8 and 5.13 show that large annealing times affect the memory of the liquid, which does not become evident until the landscape can actually be sampled upon cooling or entering the landscape-influenced regime. Put in another way, long annealing times allow the liquid to become acquainted with finer inherent energy structure within the megabasin. Memory of the liquid is also supported by

the significant hysteresis observed in the temperature dependence of the Knight shift. After long annealing times, when the liquid has had sufficient time to reach equilibrium at high temperature, tunneling [138, 140] of the liquid from a local minimum of higher potential energy in megabasin 1 to a local minimum of lower energy in megabasin 2 can occur. This leads to enhancement of peak 2 as observed in Fig. 5.8 and change of the relative populations of the two liquid states.

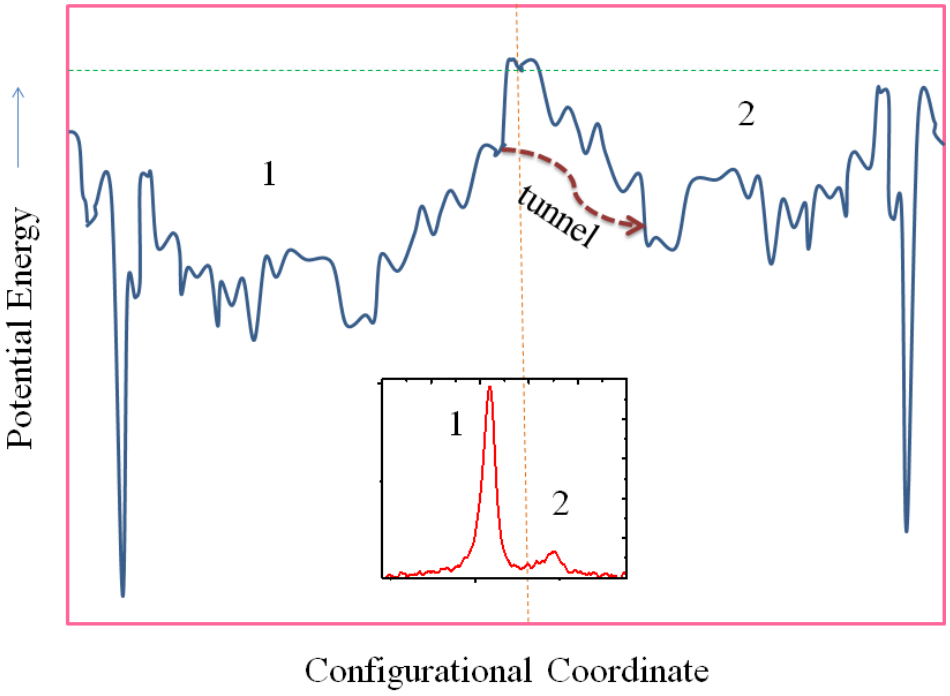

Figure 5.17 Schematic illustration of the potential energy landscape that accounts for two coexisting liquids states, adapted from [138]. Megabasin 1 corresponds to the larger liquid population and resides at a lower average potential energy than megabasin 2. The horizontal green line (- - - -) corresponds to the crossover between the free diffusion and landscape-influenced regimes. During large annealing times tunneling occurs in the landscape-influenced regime and results in an enhancement of peak 2.

5.12 Quadrupole Relaxation

In addition to fast atomic vibration and rattling, another important dynamic feature of a metallic liquid is cage collapse and diffusion [13, 114, 118, 141]. This provides a mechanism for nuclear spins to reach thermal relaxation efficiently and is caused by a

fluctuating electric-field gradient (EFG). This causes quadrupolar relaxation of the nuclear spins. In the fast-motion limit, the quadupole relaxation rate is given by [141]

$$R_Q(T) = \frac{3}{4}\frac{2I+3}{I^2(2I-1)}\left[\frac{eQ}{\hbar}\right]^2 \left\langle |V_m|^2 \right\rangle \int_0^\infty dt \frac{\left\langle V_m^*(t)V_{-m}(0)\right\rangle}{\left\langle |V_m|^2 \right\rangle} \tag{5.7}$$

where I is the nuclear spin, $V_m(t)$ is a component of the EFG, Q is the nuclear quadrupole moment, and $\langle\ \rangle$ denotes the ensemble average. The integral above gives the correlation time τ_c of the EFG, which describes the length of time that the cage of atoms around Al remains rigid. Therefore, upon cooling, it is expected that $R_Q(T)$ increases reflecting the slowing down of molecular motions.

To determine the quadrupolar relaxation rate, the magnetic contribution to the nuclear spin relaxation from the Knight shift must first be determined. Relaxation arising from the Knight shift is given by the Korringa relation [30, 32, 142]

$$R_K = \frac{4\pi k_B \gamma_{Al}^2}{\hbar \gamma_e^2} T K_s^2 / f \tag{5.8}$$

where γ_{Al} and γ_e are the gyromagnetic ratios of the aluminum nucleus and the electron, K_s is the Knight shift, T is the temperature, and f is the enhancement factor that accounts for electron-electron interactions. The factor f was calculated to be ~ 2.3 by experimentally determining $R_K(T)$ at 50, 100, 150, and 200 C.

Spin-spin and spin-lattice relaxation rates are equal in the fast-motion limit [30]. Therefore, the total relaxation rate is given by

$$R(T) = R_Q(T) + R_K(T) \tag{5.9}$$

where $R(T)$ can be obtained from the full width at half maximum (FWHM) of the NMR spectrum, and $R_Q(T)$ can be determined from (5.7) and (5.8). The factor $R_Q(T)$ was found by extracting the linewidth of peak 1 by fitting the spectrum to a double Lorenztian function. Figure 5.18 shows results of $R_Q(T)$ obtained as a function of T during heating, cooling and rapid cooling. Because of poor signal-to-noise and large errors associated with the fit parameters, the linewidths obtained for peak 2 are not included in Fig. 5.18. The results show that the correlation time of the EFG around aluminum atoms increases gradually upon cooling from 960 to just above 800 C as expected, but exhibits a large discontinuity and hysteresis at ~800C. This further verifies hysteresis and temperature dependence of the Knight shift in Fig. 5.11.

The dramatic increase in the temperature dependence of the quadrupole relaxation rate at ~800C is caused not only to the slowing down of atomic motions, but can be viewed from the effects of Ostwald ripening on atomic motions that allows phase-separated droplets to grow [26] and the non-exponential relaxation caused by landscape-influenced dynamics [2, 133]. Quadrupule relaxation is directly related to the viscosity of the droplets through cage collapse and reorientation that is necessary for viscous flow. Viscosity and surface tension studies indicate that these droplets might range in size from ~1 to 10 nm [25], which would effectively permit slowing down of atomic motions according to the Stokes-Einstein relation [143, 144]. Interestingly, this is an order of magnitude smaller than the estimated correlation length of the liquid phase-separated regions based on the NMR timescale. In Fig. 5.18 it is observed that spectral linewidth or $R_Q(T)$ is larger below the kink during slow and rapid

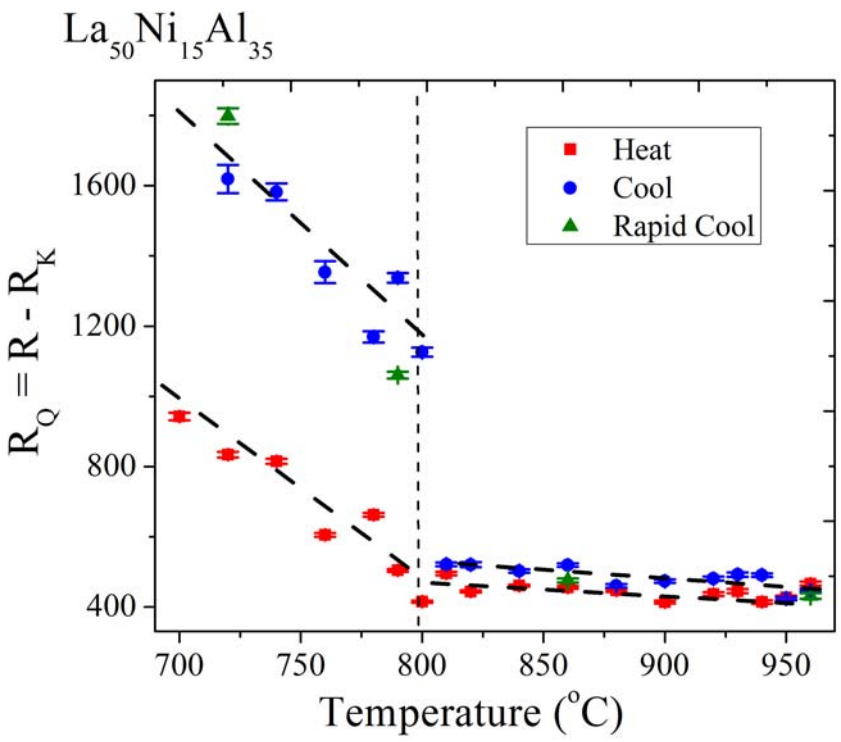

Figure 5.18 The quadrupole relaxation rate $R_Q(T)$ is plotted for peak 1 during heating, cooling, and rapid cooling that shows hysteretic behavior. The correlation time is observed to be much larger during heating than during cooling.

cooling compared to heating even though the temperature dependence is approximately the same. From the viewpoint of Ostwald ripening this may be attributed to instantaneous growth of the droplet size of the phase separated liquid, which is larger during cooling than heating. From the perspective of the landscape-influenced dynamics, which signifies the onset of solid-like behavior of the liquid, the dramatic increase of the NMR linewidth is caused by the increase of the configurational heat capacity. In the landscape-influenced regime, where the thermal energy is comparable to the potential energy, the liquid can sample all the possible liquid configurations available at a particular temperature. This highlights the importance of interatomic interactions that cause additional confinement,

sampling of different liquid configurations, and slowing down of the liquid. The hysteresis of the linewidth implies the significance of the thermal history in the liquid. This demonstrates that liquid samples the landscape much differently during heating (endothermic) than during cooling (exothermic) through 800C.

5.13 Conclusions

Temperature dependent ^{27}Al NMR experiments were carried out above the liquidus temperature in $La_{50}Ni_{15}Al_{35}$ metallic glasses. The coexistence of two liquid states was observed in addition to nonlinear liquid behavior. The two liquid states are believed to be very similar in terms of composition or density because of the small Knight shift difference between the two liquid peaks and similar slopes of the Knight shift with change of temperature. Data collection upon heating and cooling cycles confirms that the nonlinear behavior has a hysteresis, which implies energy dissipation. Annealing studies demonstrate that the liquid is not at equilibrium and that the relative population of the two liquid states can be controlled to some degree based on the annealing time. The complex liquid behavior observed in $La_{50}Ni_{15}Al_{35}$ was considered from two perspectives: 1) liquid decomposition by Ostwald ripening that is driven by differences of chemical potential and 2) energy landscape-influenced phase separation driven by density or entropy differences.

From the viewpoint of liquid decomposition, the hysteretic behavior observed in $La_{50}Ni_{15}Al_{35}$ can be attributed to energy dissipation caused by Ostwald ripening and slow Brownian flocculation processes. These kinds of behaviors are typically observed in metallic melts that have a miscibility gap, which is associated with positive heats of mixing. Study of the liquid behavior of $La_{50}Ni_{15}Al_{35}$ is especially interesting since it lacks a strong driving force for phase separation and also because of the associated nonlinear behavior, which may

provide insight for understanding other mechanisms that cause liquid decomposition. Within the framework of the potential energy landscape, the liquid behavior of $La_{50}Ni_{15}Al_{35}$ may also arise from the increased influence of the configurational entropy as the temperature is lowered. Annealing time tests show that the memory of a liquid influences the manner in which the energy landscape is explored. This was observed to have important implications for how the populations of the phase-separated liquids could change.

CHAPTER 6

Conclusions and Future Work

The work in this dissertation focused on upon three different aspects of ZrCu- and La-based metallic glasses. First, ^{27}Al NMR spectroscopy was used to study the local magnetism, anelastic deformation mechanism, and liquid state behavior. Other measurement techniques such as DSC, instron mechanical tester, magnetization measurements, SEM, X-ray diffraction, and EDS also provided tremendous support in these studies.

Chapter 3 described temperature-dependent ^{27}Al NMR spectroscopy and magnetization measurements to characterize the magnetic behavior of $(CuZr)_{46.5-x}Al_7Gd_x$ (x = 1, 2) BMGs at low temperatures. Spectroscopy results show strong spectral linewidth enhancement emerges at high temperatures. Magnetization experiments confirm that AF short-range order gives rise to local inhomogenous behavior while the system on average remains paramagnetic (i. e. no long-range magnetic order). Although the work presented in this section was significant in demonstrating how local inhomogenous magnetic behavior in dilute magnetic systems could induce frustration in the isothermal magnetization at 2K, the behavior reported here is not atypical of what is seen in dilute magnetic metallic glass systems. For example, magnetic behaviors in dilute Gd-bearing ZrCu-based metallic glasses [16, 44] also show deviations from conventional Curie-Weiss behavior and frustration of saturation magnetization. On the other hand, NMR provides an opportunity to look at the

local behavior specific to a nucleus chosen, which might otherwise be overwhelmed in macroscopic magnetization measurements.

Anelastic deformation studies of $La_{50}Ni_{15}Al_{35}$ at room temperature were summarized in Chapter 4. This work provided tremendous insight into the relevant order parameter to characterize this type of deformation (free volume vs. local structure). Nutation experiments were carried out to examine systematically changes of the EFG caused by anelastic deformation in the local environment surrounding the aluminum atoms. Much new insight into the anelastic deformation mechanism was gained from this study. For example, this study revealed that despite the small viscoplastic strains, anelastic strain is essentially what affects the local structure rather than the local density, as is expected from the various theories of deformation and free volume in metallic glasses [18, 19]. Furthermore, changes in the local density achieved by annealing are manifested by changes in the electronic structure. Another important feature of this study is the new insight gained from observing that the anelastic relaxation time at the atomic level is much longer (> 1 month) than anelastic macroscopic recovery (~few days). This aspect of relaxation has not previously been emphasized in earlier anelastic studies of metallic glasses.

Chapter 5 presented a temperature-dependent study of the liquid state of $La_{50}Ni_{15}Al_{35}$. The data show that phase separation is an important and subtle metastable feature, as evidenced by the nonlinear liquid behavior that emerges ~100 degrees above the liquidus temperature. Heating and cooling cycles confirm this by revealing the existence of a hysteresis and verify that the nonlinear behavior is a first-order phase transition. Because of the complexity of the liquid behavior observed, two different interpretations have been considered: 1) liquid decomposition by Ostwald ripening of liquid phase separation that is

driven by differences of chemical potential and 2) energy landscape-influenced phase separation driven by density or entropy differences.

Liquid decomposition processes that are typically observed in metallic melts that have a miscibility gap seem to be relevant in $La_{50}Ni_{15}Al_{35}$ even though there is no significant driving force for phase separation. This indicates that competing interactions and the resulting frustrated structures might play a significant role for phase separation. Here it is observed that simply considering the heats of mixing between elements severely underestimates the complex nature of these liquids. Therefore, if compositional phase separation and further decomposition is important, this study provides considerable new insight for new mechanisms that give rise to this liquid behavior.

In terms of the energy landscape perspective, this study provides the first clear evidence of the liquid crossing from the landscape-influenced regime to the free diffusion regime (and vice-versa) [133]. The difficultly of observing this experimentally comes from the atomic vibrations that are also sensitive to temperature. Liquid-liquid phase transitions arising from differences of density or structure are not a newly observed phenomenon in glass-forming liquids [22], but are rarely observed [106] at temperatures well above the liquidus temperature. In addition, annealing studies have demonstrated that non-equilibrium behavior affects the memory of a liquid and can ultimately change relative populations of separated phases. This truly bizarre and interesting characteristic of the liquid has not been reported previously and merits much further investigation by experiment or simulation.

This research is likely to inspire many more future studies of liquid phase behavior in La-based metallic glasses. For example, going to higher temperatures, just above the critical

temperature to achieve a homogenous liquid would be important for $La_{50}Ni_{15}Al_{35}$ since it is not clear at the moment whether phase separation is driven by nucleation and growth by spinodal decomposition [26, 145]. This can be accomplished by heating just below the critical temperature and examining the Knight shift as a function of time. Spinodal decomposition would be a likely candidate for the mechanism of phase separation if the liquid peak position changes with time. If nucleation and growth is important, then the relative intensity (indicative of the population) of the peaks corresponding to the different phases would change with time. Carrying out high temperature DSC would be beneficial in verifying that the liquid-liquid phase transition at ~800 C is in fact a first-order phase transition, by observing a change of enthalpy.

It would be beneficial to continue this study as a function of composition (i.e. $La_{50}Ni_{20}Al_{30}$, $La_{50}Ni_{25}Al_{25}$, etc.) to determine whether the liquid behavior has any implications for GFA. This might answer the question of whether immiscibility (at least locally) of structure or composition is important for enhancing GFA. A basic question that still remains is what is actually causing phase separation in $La_{50}Ni_{15}Al_{35}$. Considering the different atomic radii and heats of mixing, one can only speculate at a superficial level about the different competing structures of the liquid that might drive phase separation.

From an applications perspective, these results have important implications for the processing of metallic glass. Because of the non-equilibrium nature of the liquid the length of annealing time at high temperature was observed to either promote or suppress the growth of peak 2. It is not clear at this point whether the population of peak 2 would degrade or enhance the overall properties of the metallic glass when it is quenched. Therefore, different annealing times at high temperature followed by quenching and mechanical testing of

metallic glasses would be a good complementary study in addition to NMR to allow one to understand how to further optimize their properties for engineering applications.

References

1. van den Beukel, A. and J. Sietsma, *The glass transition as a free volume related kinetic phenomenon.* Acta Metallurgica et Materialia, 1990. 38(3): p. 383-389.

2. Debenedetti, P.G., *Metastable liquids : concepts and principles*. Physical chemistry. 1996, Princeton, N.J.: Princeton University Press.

3. Debenedetti, P.G. and F.H. Stillinger, *Supercooled liquids and the glass transition.* Nature, 2001. 410(6825): p. 259-267.

4. Turnbull, D., *Under what conditions can a glass be formed?* Contemporary Physics, 1969. 10(5): p. 473 - 488.

5. Suryanarayana, C. and A. Inoue, *Bulk metallic glasses*. 2010, Boca Raton, FL: CRC Press.

6. Anderson, P.W., *Through the Glass Lightly.* Science, 1995. 267(5204): p. 1617-1617.

7. Klement, W., R.H. Willens, and P.O.L. Duwez, *Non-crystalline Structure in Solidified Gold-Silicon Alloys.* Nature, 1960. 187(4740): p. 869-870.

8. Inoue, A., *Stabilization of metallic supercooled liquid and bulk amorphous alloys.* Acta Materialia, 2000. 48(1): p. 279-306.

9. Johnson, W.L., *Bulk glass-forming metallic alloys: Science and technology.* MRS bulletin, 1999. 24(10): p. 42.

10. H.S, C., *Thermodynamic considerations on the formation and stability of metallic glasses.* Acta Metallurgica, 1974. 22(12): p. 1505-1511.

11. and A. Inoue, *AL-LA-NI Amorphous-Alloys with a Wide Supercooled Liquid Region.* Materials transactions. JIM, 1989. 30(12).

12. Kelton, K.F., et al., *First X-Ray Scattering Studies on Electrostatically Levitated Metallic Liquids: Demonstrated Influence of Local Icosahedral Order on the Nucleation Barrier.* Physical Review Letters, 2003. 90(19): p. 195504.

13. Li, L., J. Schroers, and Y. Wu, *Crossover of Microscopic Dynamics in Metallic Supercooled Liquid Observed by NMR.* Physical Review Letters, 2003. 91(26): p. 265502.

14. Poon, S.J. and J. Durand, *Magnetic-cluster description of spin glasses in amorphous La-Gd-Au alloys.* Physical Review B, 1978. 18(11): p. 6253.

15. Durand, J., *Glassy Metal II*. Magnetic properties of metallic glasses. Vol. 53. 1983: Springer Berling.

16. Dunn, P.L. and S.J. Poon, *Magnetic interactions in d band amorphous metallic alloys.* Journal of Physics F: Metal Physics, 1982. 12(12): p. L273-L278.

17. Turnbull, D. and M.H. Cohen, *On the Free-Volume Model of the Liquid-Glass Transition.* The Journal of Chemical Physics, 1970. 52(6): p. 3038-3041.

18. Spaepen, F., *A Microscopic Mechanism for Steady State Inhomogenous Flow in Metallic Glasses.* Acta Metallurgica, 1977. 25: p. 407-415.

19. Argon, A.S., *Plastic Deformation in Metallic Glasses.* Acta Metallurgica, 1979. 27: p. 47-58.

20. Suzuki, Y., J. Haimovich, and T. Egami, *Bond-orientational anisotropy in metallic glasses observed by x-ray diffraction.* Physical Review B, 1987. 35(5): p. 2162.

21. de Hey, P., J. Sietsma, and A. van den Beukel, *Structural disordering in amorphous Pd40Ni40P20 induced by high temperature deformation.* Acta Materialia, 1998. 46(16): p. 5873-5882.

22. Paul, F.M., et al., *Polyamorphism and liquid–liquid phase transitions: challenges for experiment and theory.* Jounal of Physics: Condensed Matter, 2007. 19(41): p. 415101.

23. Kündig, A.A., et al., *In situ formed two-phase metallic glass with surface fractal microstructure.* Acta Materialia, 2004. 52(8): p. 2441-2448.

24. Popel, P.S., O.A. Chikova, and V.M. Matveev, *Metastable Colloidal States of Liquid Metallic Solutions.* High Temperature Materials and Processes, 1995. 14(4): p. 219-234.

25. I. G. Brodova, P.S.P., G. I. Ėskin, *Liquid metal processing: applications to aluminium alloy production*. 2001: CRC Press.

26. Ratke, L. and S. Diefenbach, *Liquid immiscible alloys.* Materials Science and Engineering: R: Reports, 1995. 15(7–8): p. 263-347.

27. Sastry, S., et al., *Potential energy landscape signatures of slow dynamics in glass forming liquids.* Physica A: Statistical Mechanics and its Applications, 1999. 270(1-2): p. 301-308.

28. Abragam, A., *Principles of Nuclear Magnetism*. The International series of monographs on physics. 1961: Clarendon Press, Oxford.

29. Fukushima, E. and S.B.w. Roeder, *Experimental Pulse NMR: A Nuts and Bolts Approach*, ed. I. Addison-Wesley Publishing Company. 1981.

30. Slichter, C.P., *Principles of magnetic resonance*. Springer series in solid-state science ; 1. 1990, Berlin ;New York: Springer-Verlag.

31. Knight, W.D., *Nuclear Magnetic Resonance Shift in Metals.* Physical Review, 1949. 76(8): p. 1259-1260.

32. Carter, G.C., L.H. Bennett, and D.J. Kahan, eds. *Metallic Shifts*. Progressive Material Science. Vol. 1. 1977.

33. Xi, X.K., et al., *Bonding characters of Al-containing bulk metallic glasses studied by ^{27}Al NMR.* Journal of Physics: Condensed Matter, 2011. 23(11): p. 115501.

34. J, K., *Nuclear magnetic relaxation and resonnance line shift in metals.* Physica, 1950. 16(7–8): p. 601-610.

35. Man, P.P., *Determination of spin-5/2 quadrupolar coupling with two-pulse sequences.* Solid State Nuclear Magnetic Resonance, 1993. 2(4): p. 165-180.

36. Hahn, E.L., *Spin Echoes.* Physical Review, 1950. 80(4): p. 580-594.

37. Xi, X.K., et al., *Correlation of Atomic Cluster Symmetry and Glass-Forming Ability of Metallic Glass.* Physical Review Letters, 2007. 99(9): p. 095501-4.

38. Xi, X.-K., et al., *Structural changes induced by microalloying in Cu46Zr47-xAl7Gdx metallic glasses.* Scripta Materialia, 2009. 61(10): p. 967-969.

39. Man, P.P., et al., *Spin-5/2 Hahn echoes in solids.* Solid State Nuclear Magnetic Resonance, 1995. 5: p. 181-188.

40. Bak, M., J.T. Rasmussen, and N.C. Nielsen, *SIMPSON: A General Simulation Program for Solid-State NMR Spectroscopy.* Journal of Magnetic Resonance, 2000. 147(2): p. 296-330.

41. Beck, H. and H.J. Guntherodt, *Glassy metals*. Topics in applied physics ; v. 46, 53, 72, etc. 1981, Berlin ;New York: Springer-Verlag.

42. Johnson, W.L. and T. M., eds. *Glassy metals : magnetic, chemical, and structural properties*. ed. R. Hasegawa. 1983, CRC Press: Boca Raton, Fla.

43. Dublon, G. and Y. Yeshurun, *Spin-glass - ferromagnetic transitions and critical lines in FexPd82-xSi18 metallic glasses.* Physical Review B, 1982. 25(7): p. 4899.

44. Gruzalski, G.R. and D.J. Sellmyer, *Magnetically dilute metallic glasses. II. 4f moments.* Physical Review B, 1979. 20(1): p. 194.

45. Levy, R.A. and R. Hasegawa, *Amorphous Magnetism II*. 1977, New York: Plenum Press.

46. Burgy, J., et al., *Colossal Effects in Transition Metal Oxides Caused by Intrinsic Inhomogeneities.* Physical Review Letters, 2001. 87(27): p. 277202.

47. Dagotto, E., J. Burgy, and A. Moreo, *Nanoscale phase separation in colossal magnetoresistance materials: lessons for the cuprates?* Solid State Communications, 2003. 126(1-2): p. 9-22.

48. Castro Neto, A.H., G. Castilla, and B.A. Jones, *Non-Fermi Liquid Behavior and Griffiths Phase in f-Electron Compounds.* Physical Review Letters, 1998. 81(16): p. 3531.

49. Bernal, O.O., *Nuclear Magnetic Resonance Study of the Unconventional Kondo Alloy System UCu5-xPdx*, in *Physics*. 1994, University of California Riverside.

50. Poon, S.J. and J. Durand, *The Ruderman-Kittel-Kasuya-Yosida interaction in amorphous La80Au20 alloys with dilute Gd impurities.* Solid State Communications, 1977. 21(8): p. 793-795.

51. de Châtel, P.F., *The RKKY interaction in disordered systems.* Journal of Magnetism and Magnetic Materials, 1981. 23(1): p. 28-34.

52. McCausland, M.A.H. and I.S. Mackenzie, *Nuclear magnetic resonance in rare earth metals*. Advances in Physics. Vol. 28. 1979: London: Taylor & Francis. 305.

53. Trémolet de Lacheisserie, É., *Magnetism. [Vol. 2], Materials and applications [electronic resource]*. Magnétisme. English., ed. D. Gignoux and M. Schlenker. 2005, New York: Springer.

54. Campbell, I.A., *Indirect exchange for rare earths in metals.* Journal of Physics F: Metal Physics, 1972. 2(3): p. L47.

55. Park, E.S., J.S. Kyeong, and D.H. Kim, *Phase separation and improved plasticity by modulated heterogeneity in Cu-(Zr, Hf)-(Gd, Y)-Al metallic glasses.* Scripta Materialia, 2007. 57(1): p. 49-52.

56. http://www.oxford-instruments.com/products/low-temperature/opticaland-spectroscopy/variox/Documents/Variox%20Product%20Guide%20LR.pdf. *Oxford Variox Products*.

57. Bryant, P.L., et al., *27Al field-swept and frequency-stepped NMR for sites with large quadrupole coupling constants.* Solid State Nuclear Magnetic Resonance, 2000. 16: p. 63-67.

58. Walstedt, R.E. and L.R. Walker, *Nuclear-resonance line shapes due to magnetic impurities in metals.* Physical Review B, 1974. 9(11): p. 4857.

59. Wang, J.Q., W.H. Wang, and H.Y. Bai, unpublished results.

60. Bernal, O.O., et al., *Copper NMR and Thermodynamics of UCu5-xPdx: Evidence for Kondo Disorder.* Physical Review Letters, 1995. 75(2023).

61. MacLaughlin, D.E., O.O. Bernal, and H.G. Lukefahr, *NMR and uSR studies of non-Fermi-liquid behaviour in disordered heavy-fermion systems.* Journal of Physics: Condensed Matter, 1996. 8(48): p. 9855-9870.

62. Kurland, R.J. and B.R. McGarvey, *Isotropic NMR shifts in transition metal complexes: The calculation of the fermi contact and pseudocontact terms.* Journal of Magnetic Resonance (1969), 1970. 2(3): p. 286-301.

63. Yang, L. and G.-Q. Guo, *Structural origin of the high glass-forming ability in Gd doped bulk metallic glasses.* Applied Physics Letters, 2010. 97(9): p. 091901.

64. Moon, R.M., et al., *Distribution of Magnetic Moment in Metallic Gadolinium.* Physical Review B, 1972. 5(3): p. 997.

65. Griffiths, R.B., *Nonanalytic Behavior Above the Critical Point in a Random Ising Ferromagnet.* Physical Review Letters, 1969. 23(1): p. 17.

66. Liu, C.-Y., et al., *Disorder-driven non-Fermi-liquid behavior in CeRhRuSi2.* Physical Review B, 2000. 61(1): p. 432.

67. Oddou, C.J.a.J.L., *Bulk Magnet Properties of Anorphous Gd20Y30Agso Alloy.* Sohd State Communications, 1984. 50(2): p. 155-159.

68. Larkin, A.I. and D.E. Khmel'nitskit, *Virial Expansion for Magnetic Impurities in Metals.* Soviet Physics JETP, 1970. 31(1).

69. v., L.H., T.J. L., and S. F., *Magnetic properties of (La, Gd)Al2 alloys.* Zeitschrift für Physik B Condensed Matter, 1978. 29(4): p. 319-326.

70. Poon, S.J. and J. Durand, *Critical phenomena and magnetic properties of an amorphous ferromagnet: Gadolinium-gold.* Physical Review B, 1977. 16(1): p. 316.

71. Schuh, C.A., T.C. Hufnagel, and U. Ramamurty, *Mechanical behavior of amorphous alloys.* Acta Materialia, 2007. 55(12): p. 4067-4109.

72. Taub, A.I. and F. Spaepen, *Ideal elastic, anelastic and viscoelastic deformation of a metallic glass.* Journal of Materials Science, 1981. 16(11): p. 3087-3092.

73. Argon, A.S. and H.Y. Kuo, *Free energy spectra for inelastic deformation of five metallic glass alloys.* Journal of Non-Crystalline Solids, 1980. 37(2): p. 241-266.

74. Argon, A.S., *Delayed Elasticity in Inorganic Glasses.* Journal of Applied Physics, 1968. 39(9): p. 4080-4086.

75. Courtney, T.H., *Mechanical behavior of materials*. McGraw-Hill series in materials science. 2000, Boston: McGraw Hill.

76. Cohen, M.H. and D. Turnbull, *Molecular Transport in Liquids and Glasses.* The Journal of Chemical Physics, 1959. 31(5): p. 1164-1169.

77. Park, K.-W., et al., *Paradoxical phenomena between the homogeneous and inhomogeneous deformations of metallic glasses.* Applied Physics Letters, 2009. 94(2): p. 021907-3.

78. Kawamura, Y., et al., *Newtonian and non-Newtonian viscosity of supercooled liquid in metallic glasses.* Materials Science and Engineering A, 2001. 304-306: p. 674-678.

79. Srolovitz, D., et al., *Structural defects in amorphous solids Statistical analysis of a computer model.* Philosophical Magazine A, 1981. 44(4): p. 847 - 866.

80. Argon, A.S., *Investigations of the Strength and Anelasticity of Glass*, in *Mechanical Engineering*. 1956, Massachusetts Institute of Technology.

81. Argon, A.S. and L.T. Shi, *Development of Visco-Plastic Deformation in Metallic Glasses.* Acta Metallurgica, 1983. 31(4): p. 499.

82. Chen, H., et al., *Deformation-induced nanocrystal formation in shear bands of amorphous alloys.* Nature, 1994. 367(6463): p. 541-543.

83. Sun, B.A., et al., *Aluminum-rich bulk metallic glasses.* Scripta Materialia, 2008. 59(10): p. 1159-1162.

84. Slipenyuk, A. and J. Eckert, *Correlation between enthalpy change and free volume reduction during structural relaxation of Zr55Cu30Al10Ni5 metallic glass.* Scripta Materialia, 2004. 50(1): p. 39-44.

85. Argon, A.S., *Mechanisms of inelastic deformation in metallic glasses.* Journal of Physics and Chemistry of Solids, 1982. 43(10): p. 945-961.

86. Johnson, W.L. and K. Samwer, *A Universal Criterion for Plastic Yielding of Metallic Glasses with a (T/Tg)2/3 Temperature Dependence.* Physical Review Letters, 2005. 95(19): p. 195501.

87. Ju, J.D., et al., *An atomically quantized hierarchy of shear transformation zones in a metallic glass.* J. Appl. Phys., 2011. 109(5): p. 053522.

88. Nowick, A.S. and B.S. Berry, *Anelastic relaxation in crystalline solids*. Materials science series [v. 1]. 1972: New York, Academic Press.

89. Berry, B.S., W.C. Pritchet, and C.C. Tsuei, *Discovery of an Internal-Friction Peak in the Metallic Glass Nb_{3}Ge.* Physical Review Letters, 1978. 41(6): p. 410-413.

90. Sinning, H.R., M.M. Nicolaus, and F. Haessner, *Crystallization of hydrogen-containing Co33Zr67: an internal friction study.* Materials Science and Engineering: A, 1991. 133(0): p. 371-374.

91. Matsumoto, M., H. Mizubayashi, and S. Okuda, *Hydrogen internal friction peak and hydrogen induced structural relaxation in amorphous Cu60Zr40.* Acta Metallurgica et Materialia, 1995. 43(3): p. 1109-1117.

92. Hennig, J., D. Mari, and R. Schaller, *Order-disorder phase transition and stress-induced diffusion in Au-Cu.* Physical Review B, 2009. 79(14): p. 144116.

93. Reading, M., A. Luget, and R. Wilson, *Modulated differential scanning calorimetry.* Thermochimica Acta, 1994. 238: p. 295-307.

94. Yamamoto, I., J. Van Zytveld, and H. Endo, *Electronic and atomic structure of AlxLa70-xNi30 amorphous alloys.* Journal of Non-Crystalline Solids, 1993. 156-158(Part 1): p. 302-306.

95. Yang, D.P., et al., *Magnetization and NMR study of the La-Al metallic glass system.* Journal of Applied Physics, 1991. 69(8): p. 6225-6227.

96. Yang, D.-P., *Nuclear Magnetic Resonance and Magnetization Studies of Rapidly Quenched Aluminum Based alloys*. 1988, The University of Connecticut.

97. Egami, T., *Structural Relaxation in Metallic Glasses.* Annals of the New York Academy of Sciences, 1981. 371(Structure and Mobility in Molecular and Atomic Glasses): p. 238-251.

98. Egami, T., K. Maeda, and V. Vitek, *Structural defects in amorphous solids A computer simulation study.* Philosophical Magazine A, 1980. 41(6): p. 883 - 901.

99. Iida, T., *The physical properties of liquid metals*, ed. R.I.L. Guthrie. 1988, Oxford; New York: Clarendon Press; Oxford University Press.

100. Mauro, N.A., et al., *High energy x-ray scattering studies of the local order in liquid Al.* The Journal of Chemical Physics, 2011. 135(4): p. 044502-6.

101. Busch, R., *The thermophysical properties of bulk metallic glass-forming liquids.* JOM Journal of the Minerals, Metals and Materials Society, 2000. 52(7): p. 39-42.

102. Alonso, J.A., *Electrons in metals and alloys*, ed. N.H. March. 1989, London ; San Diego: Academic Press.

103. Schenk, T., et al., *Icosahedral Short-Range Order in Deeply Undercooled Metallic Melts.* Physical Review Letters, 2002. 89(7): p. 075507.

104. Lee, G.W., et al., *Difference in Icosahedral Short-Range Order in Early and Late Transition Metal Liquids.* Physical Review Letters, 2004. 93(3): p. 037802.

105. Aasland, S. and P.F. McMillan, *Density-driven liquid-liquid phase separation in the system AI2O3-Y2O3.* Nature, 1994. 369(6482): p. 633-636.

106. Katayama, Y., et al., *A first-order liquid-liquid phase transition in phosphorus.* Nature, 2000. 403(6766): p. 170-173.

107. Sastry, S. and C. Austen Angell, *Liquid-liquid phase transition in supercooled silicon.* Nat Mater, 2003. 2(11): p. 739-743.

108. Rapoport, E., *Model for Melting?Curve Maxima at High Pressure.* J. Chem. Phys., 1967. 46(8): p. 2891.

109. CT, M., *Two species/nonideal solution model for amorphous/amorphous phase transitions.* Mater Res Soc Symp Proc, 1997. 455: p. 411-425.

110. Tanaka, H., *General view of a liquid-liquid phase transition.* Physical Review E, 2000. 62(5): p. 6968-6976.

111. Popel, P.S., M. Calvo-Dahlborg, and U. Dahlborg, *Metastable microheterogeneity of melts in eutectic and monotectic systems and its influence on the properties of the solidified alloy.* Journal of Non-Crystalline Solids, 2007. 353(32-40): p. 3243-3253.

112. Dahlborg, U., et al., *Structure and properties of some glass-forming liquid alloys.* The European Physical Journal B - Condensed Matter and Complex Systems, 2000. 14(4): p. 639-648.

113. Li, L., *Dynamics and Structure in Metallic Supercooled Liquids and Glasses Studied by NMR*, in *Physics and Astronomy*. 2005, University of North Carolina at Chapel Hill: Chapel Hill p. 119.

114. Titman, J.M., *Nuclear magnetic resonance in liquid metals and alloys.* Physics Reports, 1977. 33(1): p. 1-50.

115. Demmel, F., et al., *Diffusion in liquid aluminium probed by quasielastic neutron scattering.* Physical Review B, 2011. 84(1): p. 014307.

116. Li, J.J.Z., et al., *Evidence for a liquid–liquid phase transition in metallic fluids observed by electrostatic levitation.* Acta Materialia, 2011. 59(5): p. 2166-2171.

117. El-Hanany, U. and D. Zamir, *Temperature Dependence of the Electronic Structure of Solid and Liquid Copper-An NMR Study.* Physical Review B, 1972. 5(1): p. 30.

118. Li, L. and Y. Wu, *NMR study of liquid to solid transition in a glass forming metallic system.* The Journal of Chemical Physics, 2008. 128(5): p. 052307-4.

119. Faupel, F., et al., *Diffusion in metallic glasses and supercooled melts.* Reviews of Modern Physics, 2003. 75(1): p. 237.

120. Mallamace, F., et al., *Thermodynamical properties of glass forming systems: A Nuclear Magnetic Resonance analysis.* Journal of Non-Crystalline Solids, 2011. 357(2): p. 286-292.

121. Ritter, A.L. and J.A. Gardner, *Pseudopotential Calculation of Knight-Shift Temperature and Volume Dependence in Liquid and Solid Sodium.* Physical Review B, 1971. 3(1): p. 46-49.

122. Watabe, M., et al., *Calculations on the temperature dependence of the knight shift in liquid metals at constant volume and its measurement in sodium.* Philosophical Magazine, 1965. 12(116): p. 347-354.

123. Tanaka, H., *Relationship among glass-forming ability, fragility, and short-range bond ordering of liquids.* Journal of Non-Crystalline Solids, 2005. 351(8-9): p. 678-690.

124. D.F.R. Boer, R.B., W.C.M. Matterns, A.R. Miedema, A.K. Niessen, *Cohesion in metals*. Vol. 1. 1998, North-Holland Physics Publishing.

125. Schmidt, U., et al., *Decomposition of La- and Dy-rich amorphous alloys.* Journal of Non-Crystalline Solids, 2002. 297(1): p. 1-12.

126. Matsubara, E., et al., *An anomalous X-ray structural study of an amorphous La55Al25Ni20 alloy with a wide supercooled liquid region.* Journal of Non-Crystalline Solids, 1992. 150(1-3): p. 380-385.

127. Seyhan, I., et al., *Ostwald ripening of solid-liquid Pb-Sn dispersions.* Metallurgical and Materials Transactions A, 1996. 27(9): p. 2470-2478.

128. Lorenz, R., *Simultaneous coarsening of dispersions by growth and coagulation.* Journal of Colloid and Interface Science, 1987. 119(2): p. 391-397.

129. Lifshitz, I.M. and V.V. Slyozov, *The kinetics of precipitation from supersaturated solid solutions.* Journal of Physics and Chemistry of Solids, 1961. 19(1–2): p. 35-50.

130. Hunter, R.J., *Foundations of colloid science*. 2001, Oxford ;New York: Oxford University Press.

131. Bartsch, A., et al., *Dynamic Arrest in Multicomponent Glass-Forming Alloys.* Physical Review Letters, 2010. 104(19): p. 195901.

132. Ediger, M.D., C.A. Angell, and S.R. Nagel, *Supercooled Liquids and Glasses.* The Journal of Physical Chemistry, 1996. 100(31): p. 13200-13212.

133. Sastry, S., P.G. Debenedetti, and F.H. Stillinger, *Signatures of distinct dynamical regimes in the energy landscape of a glass-forming liquid.* Nature, 1998. 393(6685): p. 554-557.

134. Sastry, S., *Onset temperature of slow dynamics in glass forming liquids.* PhysChemComm, 2000. 3(14): p. 79-83.

135. Schroder, T.B., et al., *Crossover to potential energy landscape dominated dynamics in a model glass-forming liquid.* The Journal of Chemical Physics, 2000. 112(22): p. 9834-9840.

136. Doliwa, B. and A. Heuer, *What Does the Potential Energy Landscape Tell Us about the Dynamics of Supercooled Liquids and Glasses?* Physical Review Letters, 2003. 91(23): p. 235501.

137. Debenedetti, P.G., et al., *Theory of supercooled liquids and glasses: Energy landscape and statistical geometry perspectives*, in *Advances in Chemical Engineering*. 2001, Academic Press. p. 21-79.

138. Angell, C.A., *Formation of Glasses from Liquids and Biopolymers.* Science, 1995. 267(5206): p. 1924-1935.

139. Angell, C.A., *Landscapes with megabasins: Polyamorphism in liquids and biopolymers and the role of nucleation in folding and folding diseases.* Physica D: Nonlinear Phenomena, 1997. 107(2-4): p. 122-142.

140. Angell, C., P. Poole, and J. Shao, *Glass-forming liquids, anomalous liquids, and polyamorphism in liquids and biopolymers.* Il Nuovo Cimento D, 1994. 16(8): p. 993-1025.

141. Sholl, C.A., *Nuclear quadrupolar relaxation in liquid metals.* Journal of Physics F: Metal Physics, 1974. 4(9): p. 1556.

142. Rowland, T., *Nuclear Magnetic Resonance in Metals.* Progress in materials science, 1951. 9(1): p. 3-91.

143. Wang, Y.-Q., Y.-Q. Wu, and X.-F. Bian, *Liquid–Liquid Structure Transition in Metallic Melts: Experimental Evidence by Viscosity Measurement.* Chinese Physics Letters, 2007. 24(7): p. 2028.

144. Heitjans, P., et al., *Diffusion in Metallic Glasses and Supercooled Melts*, in *Diffusion in Condensed Matter*. 2005, Springer Berlin Heidelberg. p. 249-282.

145. Cahn, J.W., *Spinodal Decomposition.* Transactions of the Metallurgical Society of AIME, 1968. 242(2): p. 166.